Development of a time gated, compressive detection Raman instrument for effective fluorescence rejection and multilayer analysis

By Christopher J Corden (MSci)

Supervised by Prof I. Notingher

Thesis submitted to the University of Nottingham.

for the degree of Doctor of Philosophy

March 2021

The School of Physics and Astronomy

Abstract

In this thesis we have developed and implemented a Raman instrument of a novel design that uses a combination of state-of-the-art technologies to provide a temporal dimension in the measured spectrum with the goal of effective fluorescence suppression. Combining high repetition rate, picosecond laser pulses and high temporal resolution detection systems with MEMs devices we developed a time gated Raman instrument that is capable of effective fluorescence suppression and producing time-gated Raman maps thanks to the improved signal achievable through compressive detection.

Time gated Raman spectroscopy was then investigated for pigmented samples of relevance to cultural heritage and to biology. The instrument was able to recover Raman spectral information of highly fluorescent samples where a typical CCD based Raman instrument with CW laser typically fails. Multilayer samples were measured, and 3D mapping performed. By utilizing multiplexing, depth analysis was measured and calculated via photon time of flight.

The design of the instrument was optimized to overcome some of the issues that plague current time gated Raman techniques (portability, low fill factors, temporal resolution). The system uses a single element single photon avalanche diode as the detector to provide the best possible temporal resolution and a digital micromirror device (DMD) as the wavelength selective component to provide a high fill factor for maximum throughput. The DMD allows multiple spectral features to be directed to the detector at any one time (multiplexed compressive detection). The increase in signal from multiplexing allows time gated Raman maps to be performed on a time scale comparable to conventional Raman instruments (seconds per pixel). This study demonstrates the feasibility of time gated Raman mapping for a range of applications.

List of Publications

- **Christopher Corden**, Christopher J. Corden, Dustin W. Shipp, Pavel Matousek, and Ioan Notingher, "Fast Raman spectral mapping of highly fluorescing samples by time-gated spectral multiplexed detection," Opt. Lett. 43, 5733-5736 (2018)
- **Corden, C**., Matousek, P., Conti, C., & Notingher, I. (2021). Sub-Surface Molecular Analysis and Imaging in Turbid Media Using Time-Gated Raman Spectral Multiplexing. Applied Spectroscopy, 75(2), 156–167. https://doi.org/10.1177/0003702820946054
- Liao, Z., Lizio, M. G., **Corden, C**., Khout, H., Rakha, E., & Notingher, I. (2020). Feasibility of integrated high-wavenumber Raman imaging and fingerprint Raman spectroscopy for fast margin assessment in breast cancer surgery. *Journal of Raman Spectroscopy*, *51*(10), 1986-1995.
- RAMAN SPECTROSCOPY METHOD AND APPARATUS, PCT/GB2019/052618 filed on September 17, 2019., Inventors Ioan Notingher, Chris Corden, Dustin Shipp.

Acknowledgements

I would like to thank my supervisor, Professor Ioan Notingher for giving me the opportunity to pursue a PhD and pushing me to become a better scientist.

Table of contents

1 Introduction

Photons incident upon a material can interact through a variety of mechanisms; they can be reflected, absorbed, transmitted, or scattered. While the reflected and transmitted light yields little information, analysis of the absorbed and scattered light offers deep insight into the molecular composition of the sample. Rotational and vibrational modes have energies equivalent to infra-red (IR) radiation, therefore when irradiated with IR radiation, these modes absorb photons of corresponding energies. The resultant IR absorption spectrum can therefore be used to infer the presence of specific molecules.

Higher energy radiation from the ultra-violet (UV) to visible (VIS) regimes are absorbed through a change in electronic state of the molecule, which can lead to re-emission of light, in the phenomenon known as fluorescence. The mechanism behind light scattering can be classically explained as the influence of an electromagnetic wave on a polarisable medium, resulting in a dipole moment. The oscillation of this induced dipole gives rise to a secondary radiation that is emitted into a solid angle of 4π.

In elastic (Rayleigh) scattering, the induced dipole oscillates with a frequency equal to that of the incident excitation wave, thus the radiated light is of the same wavelength. Alternatively, in inelastic scattering, the induced dipole may lose or gain a certain amount of energy though interactions with vibrational or rotational modes. The radiated light will therefore have a different energy, corresponding to a different wavelength. This method of scattering is named Raman scattering after its discoverer, Chandrasekhara Venkata Raman [1].

By exploiting this mechanism, Raman spectroscopy has developed into a powerful technique for obtaining information regarding the molecular vibrations of a sample. Its non-destructive nature makes it particularly well-suited for monitoring biological or delicate samples. A wide range of techniques have been developed to excite and detect Raman scattering with the most common laboratory instrument based upon

dispersive spectrometers using diffraction gratings and charge-coupled devices (CCD).

Within such a modern Raman spectroscopy instrument, a laser is used to illuminate the sample and the Raman scattered light is then collected and filtered using highly optimized optics. The signal enters the spectrometer where it is collimated and split into its component wavelengths via a wavelength dispersive element (WDE), most commonly a diffraction grating. The resultant components are then focused onto a CCD where each spectral feature falls on a separate column of pixels, allowing the full spectrum to be analysed. As each group of pixels corresponds to a different wavelength (and therefore a different energy) the intensity profile measured by the CCD provides information about the vibrational modes of the molecules in the sample.

The field of Raman spectroscopy has applications throughout many areas of research and industry such as solid-state physics, biophysics, art and cultural heritage, medical diagnosis, mining, and forensics, to name just a few. There are, however, difficulties inherent with Raman spectroscopy. In particular, the extremely low Raman scattering cross section; for approximately 10^{10} excitation photons incident on the sample, only one Raman scattered photon will be produced. To therefore generate and detect a sufficient amount of Raman scattered photons with an acceptable signal to noise ratio, highly optimized lasers, optics, and detectors are necessary. Consequently, any source of noise, background or stray light can easily be detected and overwhelm the weak Raman signal.

The absorption of incident laser photons can also excite electronic states within the sample resulting in fluorescence emission, which typically occurs on a nanosecond timescale [2]. Fluorescence imaging utilizes this effect to characterise materials based upon the fluorophore's emission. As was first observed by Stokes, most fluorophores emit at a lower energy than they absorb because of various internal conversion mechanisms [2]. These mechanisms result in broadening of the fluorescence emission that results in low chemical specificity as many fluorophores emit in the same wavelength range. Raman scattered light on the other hand, consists of narrow bands with energy shifts equal to the sample's vibrational modes. The resultant Raman spectrum provides a chemically specific fingerprint and allows for accurate chemical classification and quantitation. Unfortunately for Raman spectroscopy, the intense,

broad fluorescence bands frequently overlap with the Raman spectrum resulting in a large fluorescence background. By shifting the excitation wavelength away from the absorption peaks of most fluorophores to the near infra-red, much of this background can be avoided. There are, however, many samples that still exhibit high fluorescence even at 785 nm excitation.

The quantized nature of light gives rise to a probability distribution that can be described by Poisson statistics, where the standard deviation is proportional to the square root of the intensity, that is for N photons the shot noise is $\sqrt{N}$. The total number of photons that affect the signal to noise ratio (SNR) are not only Raman scattered photons, but also photons introduced by fluorescence and ambient lighting. Although the average background and fluorescence can be computationally removed from the spectrum, their noise contributions remain after correction.

To therefore maximise the SNR, it is desirable to suppress all photons other than Raman photons. Modern research grade spectroscopy CCD detectors have extremely low read and thermal noise levels thanks to highly optimized electronics and cooled detector arrays. The dominant source of noise in the measured spectra is often the photon shot noise. For many samples, a significant portion of this noise arises from the fluorescence emission, as such, many samples are difficult to study by Raman spectroscopy. Various methods of reducing the fluorescence background in Raman spectroscopy have been developed and are discussed in more detail in the background chapter. An effective method however has been to take advantage of the relatively long timescales of fluorescence when compared to the almost instantaneous effect of Raman scattering. It has been previously shown that by operating in the time domain, it is possible to temporally separate the Raman and fluorescence components to successfully reduce the amount of fluorescence photons detected. [3–6].

Although there have been prior, successful time-gated Raman spectroscopy studies, due to a wide range of technical limitations, the instrument designs have been significantly less efficient than an optimized steady-state CCD based Raman system resulting. These systems have typically long acquisition times and require complex equipment. The aim of the work conducted during my years as a PhD student and outlined in this thesis is to design and build an instrument to improve on some of these technical limitations.

The main aim of the thesis was to design and build a practical time-gated Raman instrument, coupled to a microscope, that can offer effective fluorescence suppression while maintaining acceptable acquisition times to enable Raman mapping.

Furthermore, through the addition of the time dimension, depth information can be retrieved to allow sub-millimetre depth mapping based on Raman spectra, with integration times on the orders of seconds per pixel (similar to typical continuous wave Raman microscopes).

I will outline the various experimental setups, their limitations and our solution providing a novel design of a robust, compact, time resolved spectrometer.

1.1 Outline

Chapter 2 covers the background literature and the various methods of fluorescence suppression in Raman spectroscopy, with emphasis on techniques operating in the time domain. Included also are sections on compressive spectral detection and depth measurement techniques.

Chapter 3 describes the instrument design and the theoretical aspects for selecting the components used. Considerations on signal intensity and sources of noise are included for both steady state and time gated instruments under a range of measurement conditions to emphasize the potential benefits of time gating before leading on to compressive sensing and the benefits of multiplexing concluding with an overview of the electronics and software developments.

Chapter 4 presents the first results demonstrating the time-gated Raman mapping of samples in the presence of a highly fluorescing background.

Chapter 5 demonstrates the effective suppression of highly fluorescing samples of relevance to cultural heritage. The combination of time-gated and spatially-offset Raman spectroscopy allows the measurement of Raman spectra from highly fluorescent materials not only in the focal plane, but from behind a highly fluorescing surface material. Furthermore, the high temporal resolution combined with spectral multiplexing allows for rapid detection of molecular information from millimetres within an optically turbid material.

Chapter 6 presents preliminary experimental results using time-gated Raman spectroscopy for eliminating ambient lighting, the response of NIR autofluorescence to laser power, the correlation between two photon excitation and NIR autofluorescence and fluorescent lifetime measurements of biological samples.

Chapter 7 – Conclusions and future prospects

2. Background

Early in the discovery of the Raman effect it was recognized that the intensity of the "new type of secondary radiation" was orders of magnitude weaker than the Rayleigh scattering and fluorescence [7]; in fact while first reporting their discovery, C.V. Raman and K.S. Krishnan wrote "That the effect is a true scattering and not a fluorescence is indicated in the first place by its feebleness in comparison with ordinary scattering…" [8].

Still today, it can be extremely difficult to detect Raman scattering through the various sources of background noise such as fluorescence emission or stray light. Even with the most sensitive, cooled detectors with nil dark count, optimized optics and filters and ideal, monochromatic laser excitation sources, the low Raman scattering cross-section is still the major limiting factor.

The Jablonski energy diagram (Figure 2.1) diagrammatically represents some of the relevant interactions of a photon with a molecule. In fluorescence, incident photons of sufficient energy can excite an electron from the singlet ground state S_0 to an excited electronic state (S_1). For each of the electronic states there exists a number of vibrational energy levels (v = 0, 1, 2, …) and upon absorption of a photon the molecule will usually be excited to a higher vibrational level. Most molecules will rapidly relax to the lowest vibrational state via internal conversion (less than 10^{-12} s) and settle in this lowest vibrational state of S_1 prior to decaying back to the S_0 ground state with the emission of a photon. The S_1 to S_0 transition typically occurs on time scales of 10^{-8} s.

The absorption and emission wavelengths are determined by the difference in energy between the ground and excited singlet states (S_0, S_1, S_2) of the fluorophore. The closely spaced vibrational levels of the ground state coupled with normal thermal motion results in a broad range of excitation and emission energies.

Considering the energy levels of scattering interactions requires the concept of a "virtual state", where a virtual state is the result of absorption without energy conservation. [9]

In this representation, an incident photon can excite a molecule from the ground state S_0 to a virtual state. Decay back to the ground state then occurs with the emission of a photon. In most interactions, the molecule will begin and end in the lowest vibrational state of S_0, resulting in the emission of a photon with the same energy as the excitation (elastic/Rayleigh scattering).

When relaxing back to a higher vibrational ground state, the emitted photon has less energy than the excitation photon by an amount equal to the difference in the vibrational energy levels - giving rise to Stokes Raman scattering. Conversely, if the molecule begins in an excited vibrational state, then it is possible to emit a photon of greater energy than the excitation photon in anti-Stokes Raman scattering. As the probability of the molecule being in a relaxed or excited vibrational ground state depends on the molecule's temperature, the relative probability of Stokes – anti Stokes scattering is temperature dependent.

Although the probability of elastic scattering is significantly greater than inelastic scattering the intense Rayleigh scattered light can easily be filtered out with a long pass optical filter. Laser induced fluorescence on the other hand presents as a major obstacle for many samples in Raman spectroscopy as the broad emission spectra of many fluorophores overlaps with the Stokes Raman spectrum. This broad background is often orders of magnitude greater than the Raman signal, resulting in detector saturation and significant reduction in the signal to noise of the Raman spectrum, sometimes to a point where the signal is completely irretrievable. To maximise the signal to noise ratio it is therefore desirable to reject the fluorescence components. There have many been efforts to negate the effects of the strong fluorescence background in Raman spectroscopy over the years through a variety of techniques, with some more successful than others

.

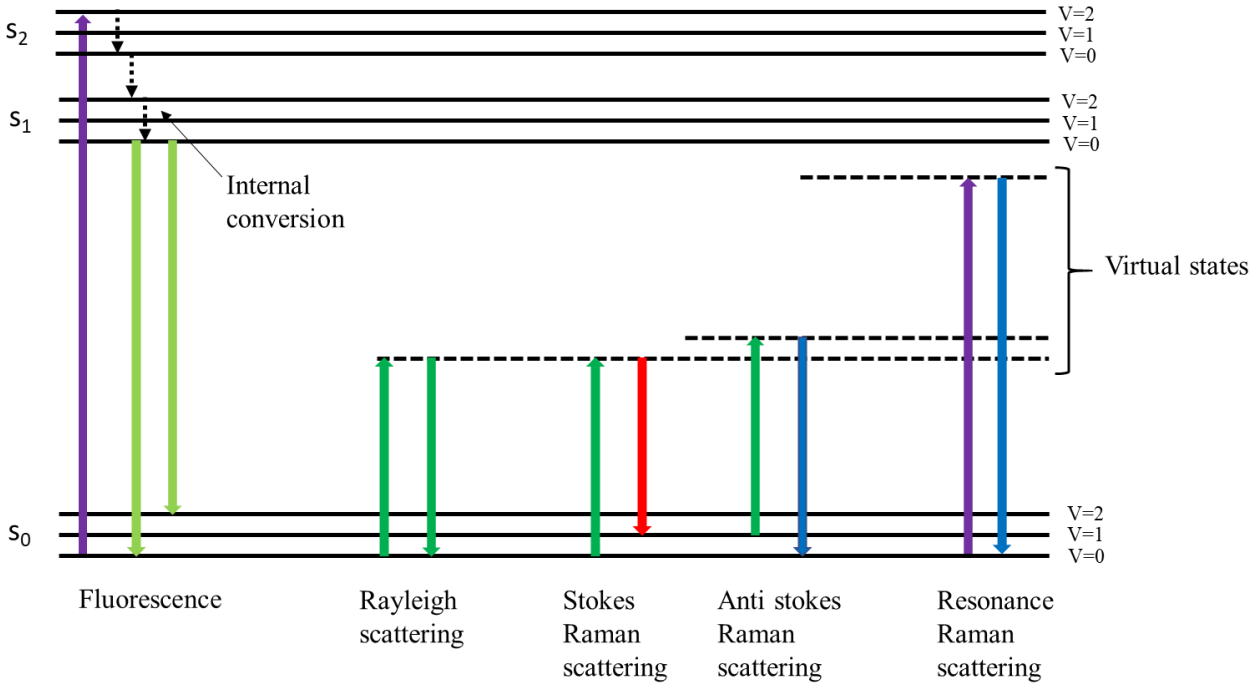

Figure 2.1 Jablonski energy diagram representing the energy transitions involved in fluorescence, Rayleigh, and Raman scattering.

2.1 Fluorophores

Within the field of fluorescence spectroscopy there are two main classes of fluorophores, intrinsic and extrinsic. Extrinsic fluorophores are artificially added to a sample to provide fluorescence to a molecule that has none. These fluorophores are often engineered to attach only to specific molecules and provide spectral and temporal contrast to the neighbouring medium. Various types of organic pigments are widely used throughout art and industry in applications such as printing, colouring of plastics and the dying of synthetic fibres. If analysis of the underlying substrate is required for scientific or forensic purposes the additional pigments can often render Raman spectroscopy ineffective.

Biological fluorophores

Intrinsic fluorophores are molecules that fluoresce in their natural form. Autofluorescence (AF) is the name given to the natural fluorescence that originates from endogenous or intrinsic fluorophores. As these fluorophores have specific absorption and emission spectra, they provide a valuable method of noninvasively probing biological samples without the need for external contrast agents. For the most part, the natural fluorophores absorb and emit in the 200-700 nm range with broad spectral features spanning roughly 50 nm (Figure 2.2). Table 2.1 lists some common endogenous fluorophores, and their properties.

Table 2.1. Fluorescence lifetimes of endogenous fluorophores from various sources.

Fluorophore	Excitation max	Emission max	Lifetime ns	reference
Tryptophan	280	350	3.03ns	[10]
Phenylalanine	260	300	7.5ns	[11]
NADPH free	300-380	450-500	0.3	[12]
Riboflavin	420-500	520-570	4.12	[13]
Fluorescein	496	500	4.0	[14]
Collagen	280-350	440	5.3	[15]
Elastin	300-370	420-460	0.3/2	[15]
Protoporphyrin IX	400-450	710	15.9	[16]
Haemoglobin	400-600	None	-	[17]
Chlorophyl a	430,662	650-700,710-740	0.17-3ns	[13]
Chlorophyl b	453,642	None	-	
Melanin	473	570-720	0.83	[18]

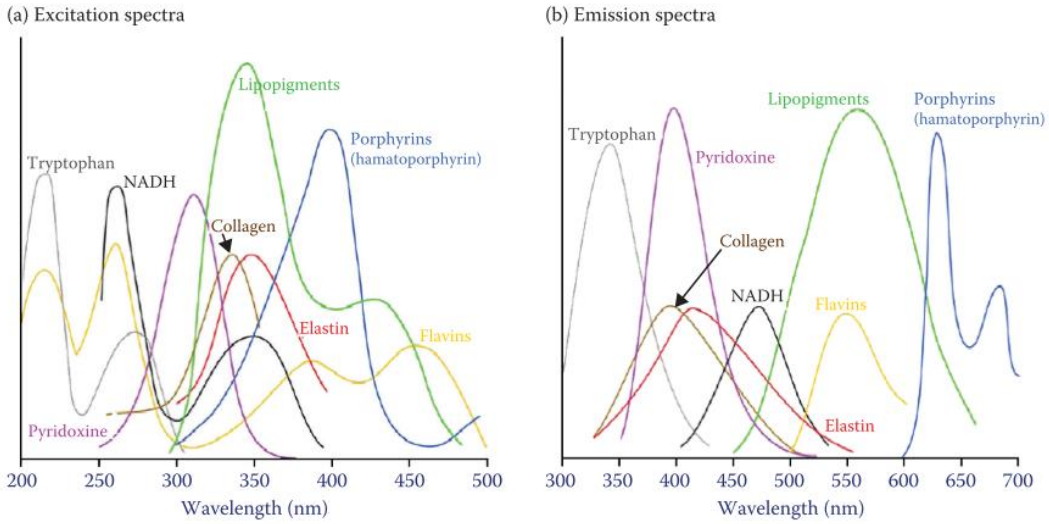

Figure 2.2. Excitation and emission spectra of biological fluorophores. [19]

To reduce the impact of the intrinsic fluorescence on Raman spectroscopy, many systems employ a NIR excitation of 785 nm. The resultant fingerprint region of the Raman spectrum is measured between 800 and 900 nm and can be efficiently detected using a silicon-based detector while avoiding much of the autofluorescence.

There are, however, many biological samples that still generate large fluorescence backgrounds even at 785 nm excitation. Lung, [20] liver [21], kidney and blood [22] all exhibit significant background with 785 nm excitation. Even though NIR excited fluorescence is significantly less intense than that produced by visible excitation, it can still overwhelm the NIR Raman spectrum. A potential source of this background has been suggested in the literature to be due to the fluorescence of porphyrin structures.

A 2017 study by Htun et al suggested that heme degradation products bilirubin and protoporphyrin IX are the likely source of near infrared autofluorescence in intraplaque haemorrhage. [23] The porphyrin band III observed in myoglobin and haemoglobin [24,25] has been suggested to be responsible for the resonant enhancement of blood using 785 nm excitation. Wood et al measured resonant Raman spectra of blood using 785 nm excitation to provide enhancements of bands at 567 cm^{-1} associated with Fe-O2 stretching mode and 419 cm^{-1} assigned to the Fe-O-O bending mode in oxygenated cells. The enhancement of B1g modes at 785 nm was

suggested to be consistent with the vibronic coupling between band III and the Soret band. [26]

Porphyrins

Metalloporphyrin's exhibit similar optical absorption spectra (Figure 2.3). Most studies on porphyrins and their optical properties are concentrated on the 300-700 nm range of the EM spectrum as this is where the strongest absorption and emission bands are found. A study by M.Uttamlal on a series of porphyrin structures showed little change in the emission spectra with varying excitation wavelengths between 400-650 nm. [27]

The most intense band lies in the 400-450 nm region and is known as the Soret band and arises from the S0 – S2 transition. The bands in the absorption spectra in the 500-700 nm range arise from $S0_n$- $S1_n$ transitions, with the lowest labelled Q(0,0)(Figure 2.3a). A charge transfer band with a maximum absorption wavelength of 762 nm (band III) is 1000 times less intense than the Soret band [26] (Figure 2.3b). This band is Vibronically coupled to the Soret band. (Vibronic coupling is the name given for the correction of some sort of inexact wavefunctions .e.g. Herzberg -Teller coupling, Born-Oppenheimer coupling or Born -Huang coupling). [28]

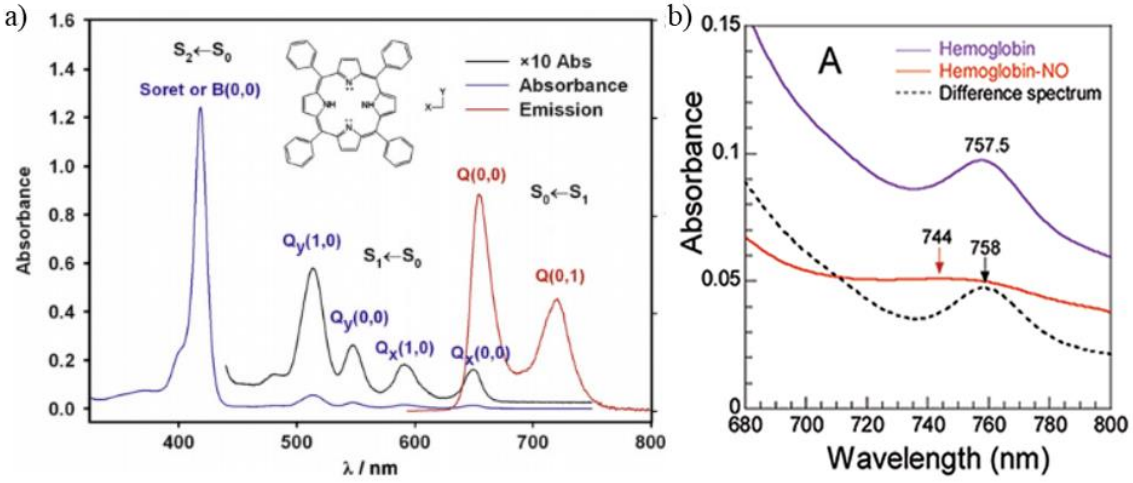

Figure 2.3 a) Absorption and emission spectra of meso-tetraphenylporphyrin at 515 nm excitation displaying the general form of many porphyrin structures. [27] 2.2b) Optical absorption of hemoglobin showing the charge transfer band III absoroption at 758 nm. [29]

2.2 Fluorescence rejection techniques in Raman spectroscopy

2.2.1 Choice of excitation wavelength

The choice of excitation wavelength is the most crucial factor to consider when considering Raman spectroscopy. Major factors to be considered are:

- Wavelength dependence of Raman scattering
- Laser induced photo damage.
- Laser induced fluorescence excitation.
- Quantum efficiency of detectors
- Resonance Raman scattering effects

Figures 2.4 and 2.5 illustrate some of the key considerations when choosing the excitation wavelength. As Raman scattering varies inversely proportional with the fourth power of the wavelength, the efficiency of the Raman scattering is increased significantly as the excitation wavelength is reduced (Figure 2.4a). For example, excitation at 780 nm results in 4.6x reduction in Raman scattering when compared with 532 nm excitation.

However, as we approach the more energetic UV regime, significant sample damage can be induced, negating a major benefit of Raman spectroscopy that is non-invasiveness. Exciting in the visible range of 400-700 nm we find ourselves with photon energies where most fluorophores absorb. Consequently, when using visible excitation, the fluorescence background is frequently a major obstacle for many samples (particularly biological). Moving further into the NIR region 700-900 nm, the excitation photons have less energy than the absorption energies of many fluorophores and although Raman scattering is significantly reduced, the reduction in levels of fluorescence justify its implementation. For many samples, 785 nm excitation has been found to be an acceptable trade-off between scattering efficiency and fluorescence.

For the samples that display intense fluorescence even at NIR excitation, the obvious choice it would seem would be to go even further into the IR to further reduce photon excitation energies.

Figure 2.5 illustrates the emission spectra of endogenous fluorophores, Raman scattering and detector operating ranges for commonly used experimental configurations and samples. For 785 nm excitation, it can be seen that the fingerprint region of the Raman spectrum spans a range of 810-914 nm, allowing for efficient detection using a silicon-based detector while avoiding much of the fluorescence. For example, the Andor iDUS series of CCD detectors have a QE of 87-60% at 800-900 nm (Figure 2.4b) while offering dark counts as low as 0.03 and read noise as low as 5 electrons per second per pixel. If, however, we are interested in the long wavenumber region of 2700-3100 cm^{-1} (996-1037 nm) the efficiency of silicon detector drops off significantly.

As the bandgap of silicon is 1.1 eV the theoretical detection limit is 1127 nm ($h \cdot c/1.1 \cdot e = 1127\ nm$). At this point the photons have insufficient energy to excite an electron to the conduction band and they are not absorbed. To detect the fingerprint region of the Raman spectrum using 1064 nm excitation (1111-1316 nm) a material with a lower energy band gap must be used.

InGaAs array-based CCDs have in recent years became available commercially with quantum efficiencies comparable to silicon detectors (Figure 2.4c). The lower energy band gap of InGaAs (0.75eV) allows for the detection of lower energy photons. However, the lower band gap results in an increased noise due to thermal excitations. Furthermore, the read noise of each pixel is approximately 1000 times greater than silicon-based CCDs (when comparing the specifications of the Andor 401 series CCD to the latest Andor iDus InGaAs 491 array series). Coupled with the low scattering efficiency at longer wavelengths this can lead to low SNR in samples that are weak Raman scatterers.

Despite the excess noise generated by InGaAs arrays, 1064 nm dispersive Raman has been shown to outperform 785 nm excitation using a CCD detector for samples that exhibit extremely high fluorescence backgrounds. Work by C.Schmidt et al used 1064 nm excitation with a Princeton Instruments OMA-V InGaAs linear array detector to successfully record the Raman spectra of various organic red colourants with significantly reduced level of background when compared to 785 nm excitation. [30]

C.Patil et al compared 785 nm to 1064 nm dispersive Raman for tissue samples of breast, kidney and liver. [31] A significant reduction in the signal to noise was

observed using the 1064 nm system for the breast tissue as the fluorescent background is relatively weak and detector noise dominates. However, the 1064 nm system outperformed 785 nm for kidney and liver as the fluorescence background of these samples is extremely intense with 785 nm excitation. They also note that even when the 1064 nm excitation is increased to account for the decreased scattering, the SNR is still ~ 8x lower due to the high read and thermal noise of InGaAs arrays.

Although 1064 nm dispersive arrays have been shown outperform 785 nm excited Raman for samples with extreme fluorescence backgrounds, the low Raman scattering at 1064 nm excitation and high detector noise require long integration times to acquire spectra with adequate signal to noise ratio.

One final factor to consider when selecting the excitation wavelength is resonance effects. When the energy of the excitation laser corresponds to the energy of an electronic state within the sample, a resonance effect is observed leading to an increase in the signal of the Raman band associated with the excited molecule. If the resonances of the sample to be measured are known beforehand the instrument can be designed around this. Although certain Raman bands are enhanced, a significant increase in fluorescence background is also to be expected from the matching of the energies of the excitation photons to the electronic states. In such cases it is required to suppress the fluorescence via methods such as time gating. [4]

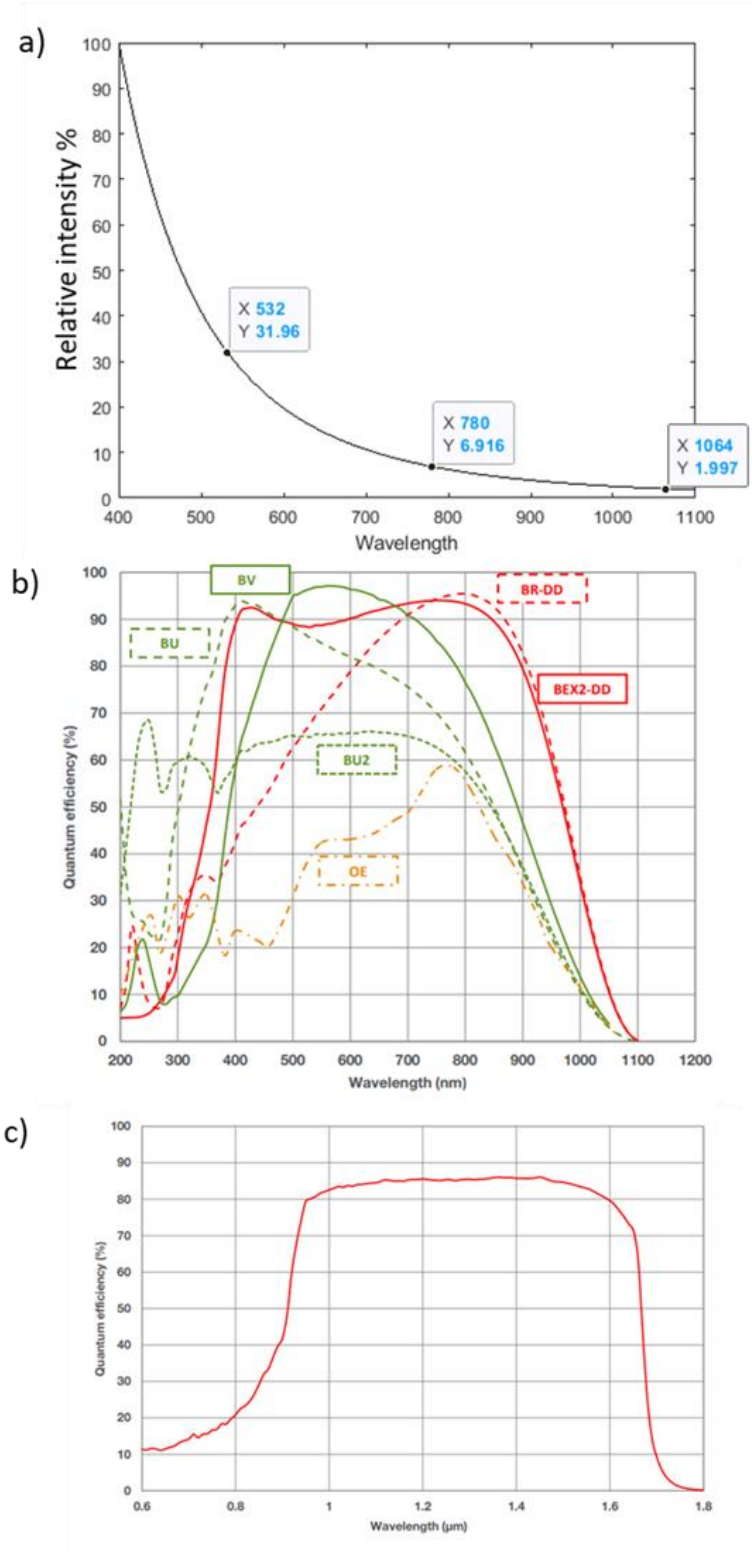

Figure 2.4a) Relative $1/\lambda^4$ dependence scattering with common excitation wavelengths highlighted. b) QE of a silicon-based CCD detector (Andor iDus 401 series CCD). c) QE of InGaAs-based CCD detector (iDus 1.7 μm InGaAs @20degree C).

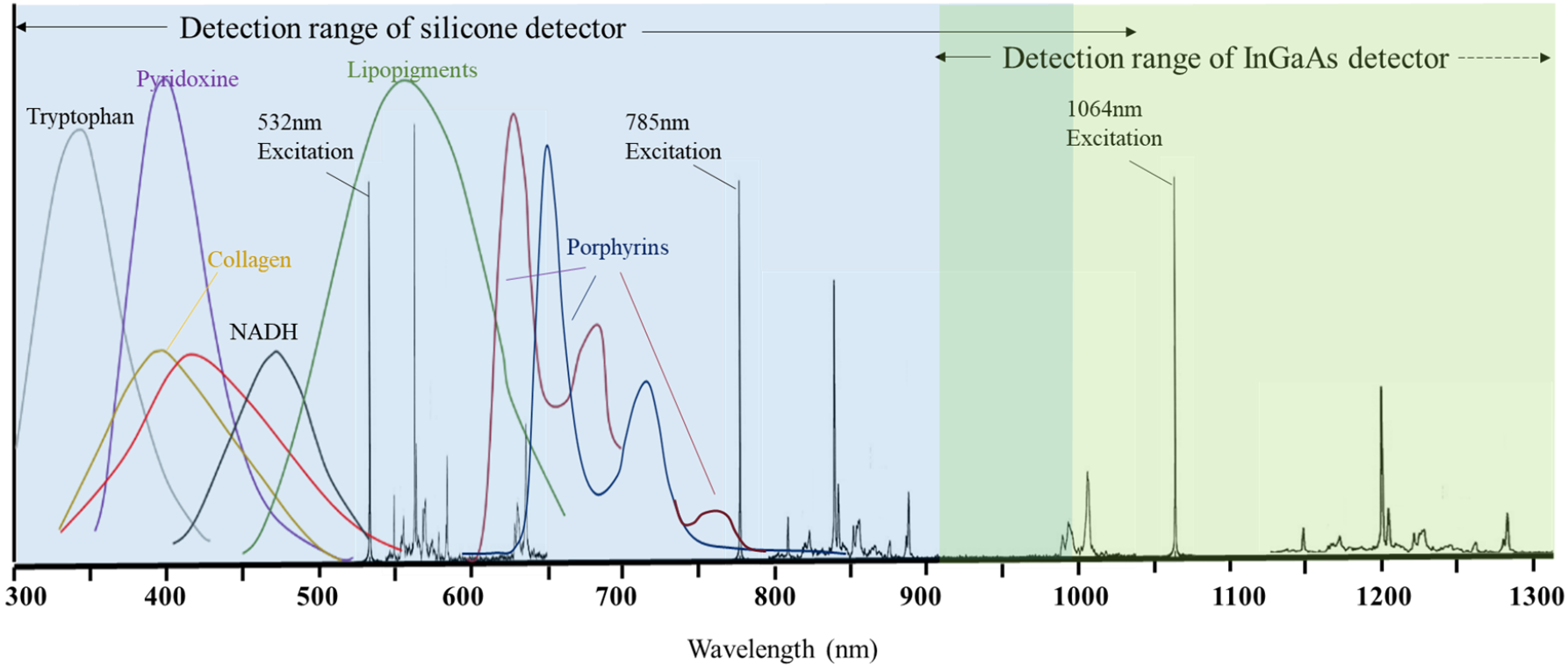

Figure 2.5) Emission spectra of biological fluorophores [19] with Raman spectra of polystyrene at 532nm, 785nm and 1064nm excitation. Blue background represents region where silicone-based detectors efficiently operate. Green background represents the shortest wavelength detection range of InGaAs based detectors.

2.2.2 Fluorescence bleaching

Theoretically, the electronic transitions that give rise to fluorescence can repeat indefinitely. In practice however, most fluorophores experience photobleaching under high intensity, continuous illumination, [2]. The highly reactive excited states give rise to structural instabilities of the molecules, leading to a structure that can no longer fluoresce.

This mechanism is undesirable for fluorescence imaging, however it has been used to the advantage of Raman spectroscopy to provide a reduction in background. [32,33] Samples are exposed to high intensity illumination for minutes to hours prior to the Raman spectroscopy measurement to chemically alter the fluorophores so they no longer fluoresce. Of course, this technique can only be applied to samples where photodamage is of no concern and the Raman bands of interest are not affected by the bleaching.

2.2.4 Wavelength domain

For small changes in excitation wavelength the response of the Raman scattering will closely follow that of the excitation wavelength while the fluorescence emission spectrum will remain relatively unchanged. Shifted excitation Raman difference spectroscopy (SERDS) is a technique first described in 1991 by A.P.Shreve et al [34], where a sample is excited with an excitation wavelength λ_1 and the resultant spectrum $S_1(\lambda)$ is then measured, consisting of both fluorescence and Raman photons. The sample is then excited with an excitation wavelength λ_2, and a second spectrum $S_2(\lambda)$ is then acquired. The difference in the spectra $S(\lambda) = S_1(\lambda)$ -$S_2(\lambda)$ is then calculated. As the fluorescence background is unchanged by the shift, the resultant spectrum is background free. The remaining spectrum presents as derivative shaped and needs to be modelled to generate a conventional Raman spectrum.

The technique has been shown to be effective in removing the average background fluorescence. However, the photon shot noise cannot be simply subtracted and will remain after subtraction.

2.2.5 Computational techniques

Computational processing of the data is a critical step in analysis of hyperspectral data. If the background consists of a broad continuum, devoid of sharp features, various computational techniques are available to subtract the contributions resulting in a baseline corrected Raman spectrum. The goal of any background removal technique is to remove the background without affecting the overlaying spectrum. Methods include Fourier transformations, wavelet transforms, [35,36] first and second order differentiation [37,38] and polynomial fitting. Polynomial curve fitting techniques are favoured due to their simplicity and effectiveness. Many mathematical tools such as MATLAB incorporate built in fitting tools that allow the user to fit a polynomial to a spectrum using a least squares-based curve fitting function. One common method proposed by C.A.lieber, known as the modified polyfit method, modifies the fitted curve by iteratively removing the spectral features that lie above the fit. [39] The resulting modified curve provides a corrected background. This method can be automatically implemented to large datasets with minimal user input.

While effective and essential, computational techniques can only operate on the data provided. Photons incident on a CCD are converted to electrons and stored in a bin during the measurement window. Mixed up in these bins are electrons from Raman scattering, fluorescence emission, thermal and electronic noise, and ambient light. The resulting noise is therefore the sum of all sources. What is needed is another dimension of measurement to separate the sources of signal.

2.2.6 Time-domain Raman spectroscopy

Operating in the time domain requires the use of a pulsed laser and a detection system with a fast temporal response. As Raman scattering can be considered instantaneous the duration of the Raman signal will closely follow that of the excitation laser pulse. If the duration of the laser pulses are significantly less than the emission lifetime of a typical fluorophore ($\sim 1\ ns$) and the detection has an appropriate time response, it is possible to discriminate between the different mechanisms (Figure 2.6), and thus separate the Raman photons from the fluorescence. To achieve this temporal discrimination, various detection methods have been employed, each with their own advantages and disadvantages.

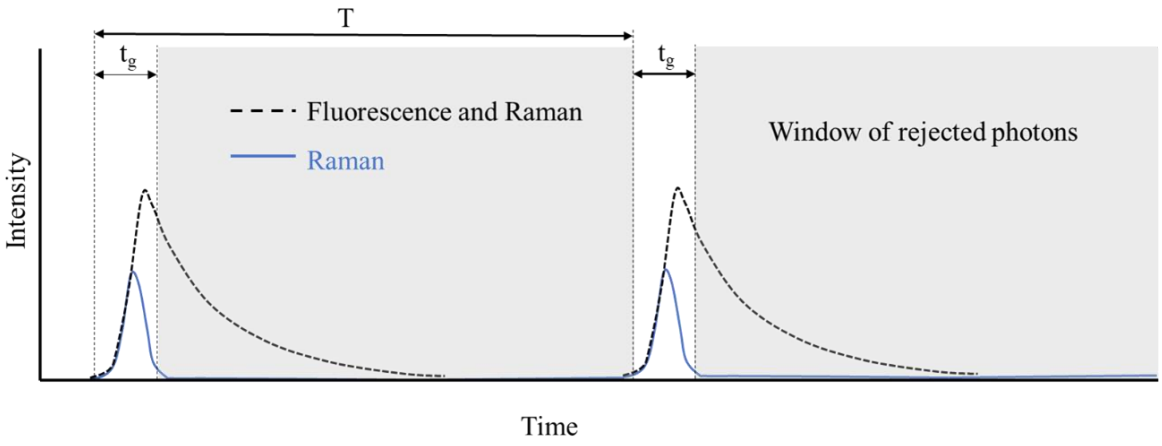

Figure 2.6. Graphical representation of the time gating principle in Raman Spectroscopy. The period T = 1/repetition rate and t_g is the width of the measurement window. The blue curve represents the Raman signal while the black curve represents the total signal consisting of both Raman and fluorescence.

For every period *T*, the detection method will be configured to only acquire photons from a small window known as the 'gate' window of width t_g. Photons incident on the detector that lie outside of the gate window will not be detected and thus would not contribute to the total signal. This of course can lead to a significant reduction in background from all sources, such as ambient light and thermal detector noise. Provided the laser excitation pulse and the temporal resolution of the instrument is less than the gate window, the total possible background suppression is given by the ratio of the time gate to the period of the laser pulse T/tg.

For background contributions solely from fluorescence emission, the amount of effective fluorescence suppression can be approximated from the ratios of the fluorescence decay and the temporal profile of the Raman signal (instrument response function (IRF)).

2.3 Time-gated Raman spectroscopy

The idea of fluorescence suppression through the use of time gating has been around for a long time. S Burgess and I.W Shepherd from the University of Manchester used the technique in 1976 to reduce the fluorescence of Rhodamine G in a sample of benzene by a factor of 6 [40] (IRF of 1.5 ns FWHM). In 1986 J Howard et al used the technique to provide enhancements by a factor of 14.6 for Raman/fluorescence background and 2.8 (Raman signal/florescence noise) for a benzene sample doped with a fluorophore of lifetime 11.8ns while corresponding improvements of 5.5 and 2.0 were observed with a dopant of 3.9 ns lifetime [6] (IRF of 1.75 ns IRF).

The techniques used by Burgess and Howard used a single detector (PMT). Using a single element detector makes the acquisition of the full spectrum a timely process as the sensor or diffraction grating would need to be scanned for every spectral point of interest. Advances in detector technology have provided new solutions such intensified CCD (iCCD) cameras or single photon avalanche diode (SPAD) arrays. A novel solution was proposed by Matousek et al in 1999 based on the optical Kerr effect [41]. Polarised signal consisting of Raman and background light passes through a Kerr medium which is then activated via a high powered, picosecond laser pulse. By adjusting the physical path length of this so-called gating pulse, it is possible to change the polarisation of the Kerr medium at the precise time, allowing only Raman scattered photons to reach the detector. Although the result is picosecond resolution time-gated Raman (4 ps temporal resolution), the system requires a high-energy picosecond pulsed laser to activate the Kerr medium, resulting in a complex, expensive solution with a repetition rate of only 10kHz. Since the repetition rate is low, high pulse energies must be used for exciting the Raman photons in order to achieve sufficient signal, which can result in photodamage to the sample. The short gate widths and low rep rate require long acquisition times to generate spectra with adequate signal to noise ratios.

Single photon avalanche diode (SPAD) array-based spectrometers offer great potential. Detector arrays with single photon sensitivity and exceptional time resolution could potentially offer a direct replacement for modern CCD detectors. Such arrays are still in development stages with various issues to be overcome such as

low fill factors, high dark counts, low sensitivity, and array inhomogeneity across temporal, noise and sensitivity dimensions.

Many array detectors use a common gate by pulsing the bias voltage across all pixels, however some recent developments incorporate time to digital convertors on each pixel, offering a significant improvement as each pixel can be operated in TCSPC mode [42]. This comes at cost of fill factor as more of the array area is taken by electronics. The reader is directed to a thorough review on developments in SPAD array technology over the last decade by Claudio et al [43].

Recent years have seen the improvement of SPAD arrays to the point where a commercially available time resolved spectrometer has been developed based around 128 x 8 active sensor elements [44]. The commercial instrument uses an 8x768 pixel array with 100 ps temporal resolution in conjunction with a 532 nm, 150 ps pulsed laser.

It is an active field of research, and it is feasible to assume that over the next decade, the technical limitations will eventually be overcome through advances in semiconductor fabrication. As the fundamental semiconductor material is silicon, the resulting devices can be expected to have detection sensitivities equal to or exceeding the best silicon-based CCDs while offering temporal resolution of less than 10 ps.

Intensified Charge Couples Device (ICCD)

Image intensified CCD (ICCD) use an image intensifier coupled to a CCD array to achieve ultrafast gating (Figure 2.7). In what can best be described as a combination of a microchannel plate PMT and a CCD, incident photons strike a photocathode and produce photoelectrons. The photoelectrons are then accelerated by a high voltage via a microchannel plate which provides a collimation effect, preserving the spatial properties of the incident photons. The electrons then strike a phosphor plate which is coupled to a CCD detector. The detector can be gated by pulsing the accelerating voltage resulting in some models achieving sub nanosecond timing resolution. There will be a loss of efficiency and additional noise considerations because of the photon-electron-photon-electron conversion process.

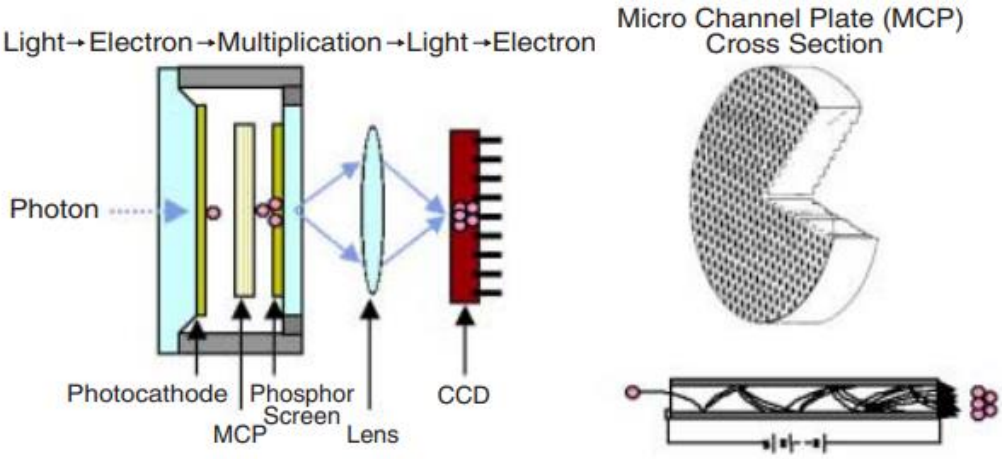

Figure 2.7. Schematic of general principles of an ICCD. [45]. The narrow channels of the microchannel plate preserve spatial information while reducing the transit time spread (TTS) of multiplied electrons.

Commercially available, multichannel detection with sub ns temporal resolution the ICCD offers the best option of available current technology for measuring low light with a high degree of temporal resolution.

The ICCD has been successfully applied to measurement of depth through photon time of flight in applications such as brain imaging [46], Raman depth analysis of mineral samples [47] and Raman analysis of depth through diffusely scattering media [48].

The ICCD has been used for effective fluorescence suppression where E.Efremov et al used this model to successfully reduce fluorescence in resonance Raman spectroscopy using a gate width of as low as 80 ps to achieve a reduction in the fluorescence background of a factor of 79 for a 5 ns fluorophore with a spectral resolution of ~15 cm^{-1}. [49]

The PicoStar HR (LaVision) is a state-of-the-art intensified gated/modulated CCD camera system which offers a temporal resolution of 250 ps. In a study by J.Selb et al, the detector is used for depth resolved brain imaging using 750 – 850 nm where the sources of noise are analysed for NIR wavelengths [46].

The quantum efficiency of the photocathode material (S20) is 0.46 % at 850 nm. Of the photoelectrons generated ~60 % of theses enter the microchannel plate active area. The accelerated electrons then excite green photons through the interaction with a phosphor layer. The green photons are then detected by the CCD with a quantum efficiency of 70 %. At 850 nm (the midpoint of the Raman fingerprint region with 785

nm excitation), approximately 0.0046 x 0.6 x 0.7 = 0.19 % quantum efficiency can be estimated by these results.

There are multiple sources of noise to be considered that vary depending upon the instrument parameters used such as binning and intensifier gain. These include intensifier shot noise, thermal noise, amplification noise from the MCP gain process, photon shot noise from the phosphor screen, CCD dark noise and CCD read noise. The group calculated the signal to noise ratio vs incident photons at the ICCD at 800 nm, for a range of intensifier gain voltages (Figure 2.8). It is seen that to achieve SNR of just 10:1, a minimum of approximately 10^4 incident photons are required.

Although this method provides an acceptable and flexible solution for time gated Raman spectroscopy, noise generated by at the various stages is significant and photocathodes have extremely low efficiency in the NIR. This detection method is therefore better suited to resonance Raman experiments using UV-VIS excitation.

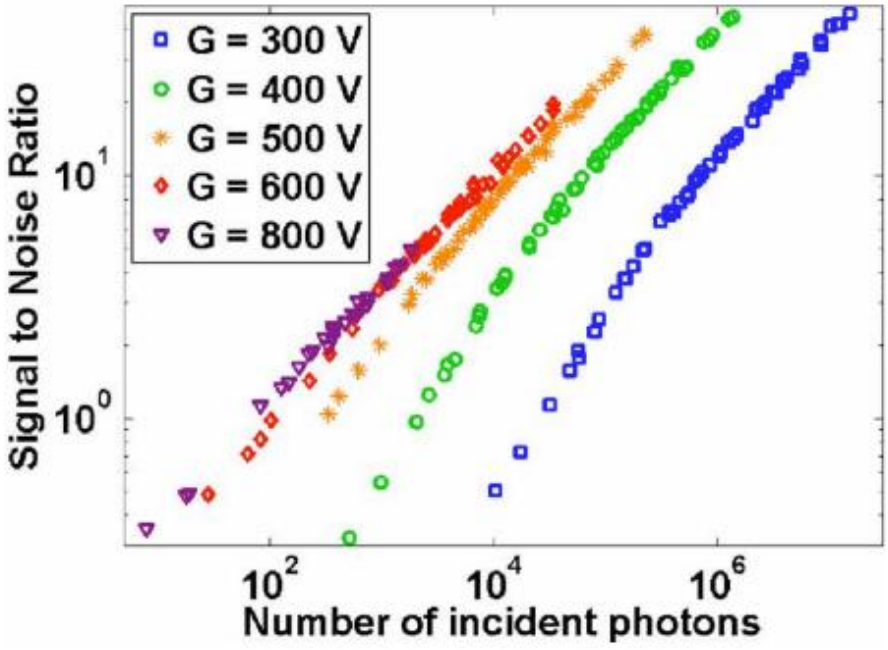

Figure 2.8. Signal to noise vs incident photons for the PicoStar HR (LaVision) for a range of intensifier gate voltages (G) at 800 nm. [46]

TCSPC

Most of the time gating techniques mentioned thus far use a fixed time gating window of a specific width determined by either software or by fixed experimental parameters. To recreate a time profile of the sample this gate window must be moved incrementally in time and repeat measurements must be made.

Operating in time correlated single photon counting mode (TCSPC), every photon is measured, and time tagged before being saved for later analysis all in one measurement. This provides an advantage over the fixed gate window as the time profile of the photon distribution can be determined with just one measurement. From this time histogram, the lifetime of the sample, photon diffusion times and the optimum time gate can be determined later in data analysis stages. This offers a significant advantage if one wants to produce time-gated Raman maps of heterogeneous samples of varying background levels and optical properties as different time-gates can be applied at various measured spectra.

2.4 Compressive detection

In the examples mentioned so far, both single channel and multichannel detectors have been used to provide the additional temporal dimension required for time-gated Raman spectroscopy. To generate a full spectrum using a single channel detector, each wavelength must be measured sequentially resulting in long acquisition times. Furthermore, any variation in signal during the measurement due to photobleaching or other experimental factors will result in spurious spectral features. The speed advantages of detecting the whole spectrum simultaneously are obvious. Apart for increasing data acquisition speed, any variation in background during the measurement window is measured equally over all channels, providing a true representation of the information.

There are, however, situations where the use of a single channel detector offers advantages over a multichannel detector, such as operating effectively in the infra-red range or when superior temporal resolution is required. To take full advantage of the single channel detector in such situations, it is desirable to simultaneously detect photons from all the relevant vibrational modes. By doing so, there are certain regimes where it actually becomes advantageous to use a single detector.

There is a signal to noise penalty accrued for dispersing the spectrum over many pixels as the measurement of each individual pixel of a CCD is accompanied by its own read and thermal noise. In low signal regimes, where the CCD read-out and thermal noise become dominant, there is a potential signal to noise advantage to be gained by multiplexing the spectral features of interest to a single channel detector.

In hyperspectral Raman imaging a sample is typically raster scanned in the x-y plane while a multichannel detector acquires data at each point. The information recorded is stored as a data cube with dimensions x,y & λ (with typical sizes in Raman mapping of 100 x 100 x 1024). The hyperspectral data acquired by a multichannel detector is complex and must be converted to lower dimensional space to clearly represent the desired information.

Univariate techniques consider only one variable at a time and use simple methods such as integrating the area under a curve to reduce the entire spectrum to a single value. As the spectroscopic data acquired contains multiple variables, multivariate analysis is required to take full advantage of the available information. The outcome is the same however - the compression of the data so the relevant information can be clearly represented and visualised.

Spatial light Modulators

Digital micromirror devices (DMD) are micro-electrical-mechanical (MEMS) devices developed by Texas Instruments that consist of arrays of microscale mirrors (Figure 2.9). Each pixel is a bistable optomechanical element whose state can be rapidly controlled by software. Initially developed for light projection systems and finding applications in industries such as 3D printing and digital lithography they have, in recent years reached an efficiency level that meets the stringent requirements required for Raman spectroscopy.

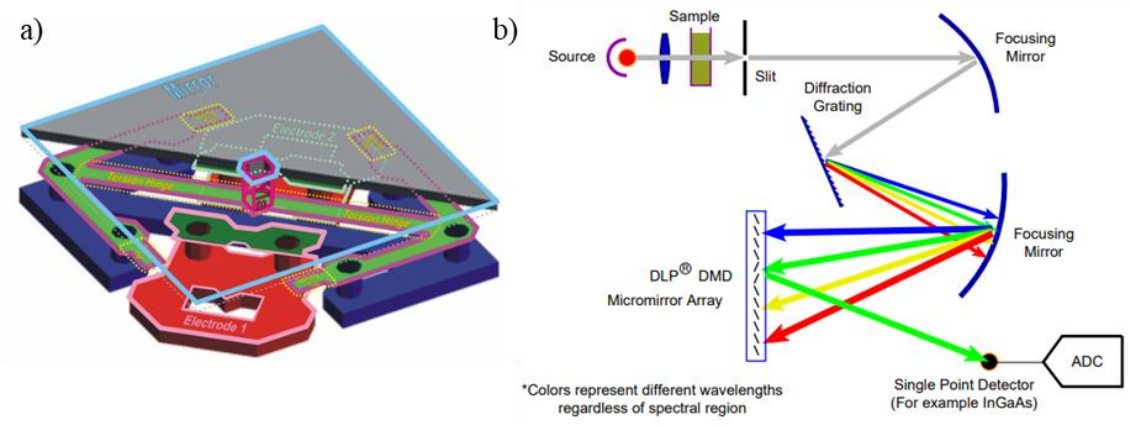

Figure 2.9a Diagram of a single pixel from a digital micro mirror device. [50] 2.9b. Application of a DMD as a programmable optical filter for use in spectroscopy. [51]

The integration of DMDs allows for real time manipulation of optical systems, paving the way for a range of techniques that could not be alternatively achieved. [52] For example, dispersing a spectrum across a DMD allows multiple wavelengths to be simultaneously focused onto a single detector (i.e. spectral multiplexing), essentially compressing the data at the measurement stage, hence these techniques have become known as compressive sensing (Figure 2.9b). [53–56]

There is currently active research into the optimization of the optical filters projected by the DMD based upon supervised and unsupervised approaches. [57–59] Recent results have shown that compressive Raman detection using an optimized filter algorithm outperformed both CCD and EMCCD detectors in the high and low signal regimes in terms of both speed and limit of detection. The study compared the signals from phantom samples mimicking microcalcifications relevant to breast cancer diagnosis. [54]

3 Instrument Design

3.1.1 Introduction

In order to determine the required specifications of any instrument the goals must be first defined.

Goals

1. Effective fluorescence suppression of samples that exhibit intense levels of fluorescence, rendering conventional Raman spectroscopy ineffective.
2. Non-Invasive - Maintain the ability to analyse delicate samples such as biological samples or those of historical and cultural significance.
3. Effective suppression of ambient lighting leading to an instrument that can potentially be used in optically noisy conditions.
4. Acquisition times comparable to current steady state Raman instruments.
5. Depth analysis via photon time of flight measurements
6. Measurement of the fluorescence lifetimes

The ultimate goal is a time gated Raman instrument that can effectively supress fluorescence background of biological samples to provide real time diagnosis of disease and produce scans on a time comparable to that of a continuous wave CCD based spectrograph. That is, to produce Raman maps on the order of seconds per pixel. The additional modality of fluorescence lifetime imaging to provide rapid discrimination of regions of interest is a secondary function that arises from the use of a high temporal resolution detector operating in TCSPC mode. Furthermore, by operating in TCSPC mode, the photon time of flight can be determined providing depth information of optically turbid samples.

The first goal is the main motivation for this project, and it has been shown in the literature that by operating in the time domain, is possible to temporally separate Raman scattering from fluorescence. As defined in the Background chapter, by operating in the time domain, the effective amount of fluorescence suppression achievable depends on the fluorescence lifetime of the fluorophores in the samples and the temporal resolution of the instrument.

Intended applications - as our group, the Bio-photonics group is primarily interested in acquiring Raman spectra from biological and organic samples, the instrument specifications are selected with these samples in mind.

For background contributions solely from fluorescence, the amount of effective fluorescence suppression can be approximated from the ratios of the fluorescence decay and the Raman signal temporal profile (instrument response function (IRF). Modelling the IRF as an infinitely sharp rising, single exponential decay has been shown to provide results consistent with experiment for Kerr gated and iCCD based time gated Raman systems [49,60] and can be therefore used to predict and compare the effectiveness of various detection methodologies.

$$fl_{bg}/_{Raman} = \frac{\int_0^{\infty} e^{-t/t_f} dt}{\int_0^{tg} e^{-t/t_f} dt} = \frac{1}{1-e^{-tg/t_f}} \approx \frac{t_f}{t_g} \qquad [3.1]$$

where t = time, t_f = fluorescence lifetime and t_g is gate width.

To estimate the effectiveness of potential solutions we must consider the properties of the fluorophores, lasers, and detection methods at all wavelength ranges. We can then make a comparison to the alternative techniques such as Kerr gating, SPAD arrays, iCCDs and 1064 nm Raman with InGaAs detectors. For a sample with a fluorescence lifetime of just 1ns we would require a temporal resolution of 100 ps to achieve a 10x improvement in the Raman to fluorescence background ratio. Figure 2.2 shows the excitation and emission spectra of common endogenous fluorophores and Table 3.1 lists the lifetimes of fluorophores taken from various sources in the literature.

Table 3.1 Properties of endogenous fluorophores with predicted amount of fluorescence suppression for a time gated Raman system with a 100 ps gate width.

Fluorophore	Excitation	Emission	Lifetime, (ns)	Ref	Predicted suppression factor (100 ps gate)
Lung tissue	680	780	5-6ns	[61]	60
Protoporphyrin IX	400-450	710	15.9	[16]	150
Protoporphyrin IX	400-500	633	8.4-13	[62]	84
Elastin	337	>345	2.3	[15]	23
Collagen	337	>345	5.3ns	[15]	53
Melanin	473	570-720	0.83	[18]	8.8
lipofuscin	470	>510	2.4	[63]	24
NAD(P)H (hepatocytes)	362	450	2.8ns	[64]	28
Chlorophyl a	430,662	650-700,710-740	0.17-3ns	[13]	2.2-30

3.1.2 Justification for using NIR.

From the absorption and emission characteristics of biological fluorophores alone it is clearly seen that if fluorescence suppression of biological samples is the ultimate goal, then UV-visible excitation should be avoided unless resonance Raman is desirable.

It is well known that the autofluorescence generated by endogenous fluorophores can generally be avoided through near infra-red excitation, there are however many samples that exhibit intense backgrounds even at these wavelengths. As described previously in the Background chapter, the source of much of this is thought to be due to porphyrin-based molecules however, NIR autofluorescence literature is scarce and the sources of the fluorescence background in this region are still not clear.

The main absorption band of the porphyrin is known as the Soret band and strongly absorbs around 400 nm while emitting in the 600-800 nm range. Porphyrins however have multiple absorption mechanisms; the Q bands span from 500-650 nm while the

charge transfer band III lies around 740-800 nm and although the absorption due to the charge transfer band III is approximately 1000 time weaker than the Soret band, it still results in an intense background at 785 nm excitation.

To meet the goals, a wavelength that minimizes the fluorescence while maximizing the signal to noise was selected. By choosing a NIR laser excitation of 750-800 nm we minimize laser induced fluorescence and photodamage while still allowing for detection of the Raman fingerprint region using silicon-based detectors. Selecting a longer excitation wavelength of 1064 nm we are required to use InGaAs detectors which have much higher thermal and electronic noise than silicon-based detectors and for low signal regimes this thermal and read noise dominates.

3.1.3 Current state of the art

There are two main methods of detecting signals with a degree of temporal resolution: time gating and time correlated single photon counting (TCSPC). Time gating refers to the acquisition of data over a fixed measurement window. This can be realized in a variety of ways but in general, a gating pulse (either optical or electrical) is applied to the incoming signal to either allow or block the photons incident on the detector. To therefore measure the signal intensity as a function of time, multiple measurements must be made while incrementally varying the timing of the gating pulse with respect to the laser pulse. In TCSPC, a fast detector is used to measure the occurrence of single photons with respect to the excitation laser pulse via a time to digital convertor (TDC). The resultant signal is a stream of numbers, each representing the photon arrival time. In this way the complete signal is acquired in one measurement. The appropriate analysis can then be performed at a later stage to provide, fluorescence rejection, photon diffusion times and fluorescence lifetime analysis. The main drawback to this method is the size of the datasets that are generated.

Designs based on optical Kerr gating proposed by Matousek et al [41] offer the best temporal resolution (4 ps) achieved thus far but at a cost of complexity and reduced throughput. The actuation of the Kerr medium requires a powerful pulsed laser, and their current system can only achieve repetition rates of 10kHz. To therefore irradiate the sample with enough average power, the pulse energy must be high, risking damage to the sample. The short gate window and the low repetition rates result in very little signal reaching the detector and therefore long acquisition times. Currently such a

design is restricted to only one laboratory in the world (Rutherford Appleton Laboratory).

La Vision's PicoStar HR Intensified CCDs (iCCDs) offer an ideal solution to the shortcomings of the Kerr gated system. Relatively easy to implement, high repetition rates of up to 100MHz with a sub 300 ps intensifier gate width FWHM. It has been shown by F.Ariese at al, that effective fluorescence suppression and depth profiling is attainable using this iCCD camera-based system [48,49]. Operating at high repetition rates minimises the probability of laser induced damage for a given average power, furthermore, by carefully adjusting the position of the gate window with respect to the incoming laser pulse the group showed the effective gate width could be as low as 80 ps. The S25 photocathodes for NIR detection offer 0.1-0.2% quantum efficiency for 800-900 nm detection.

SPAD array-based spectrometers are still in the development stages however there is one currently available commercial system from Timegate instruments, Finland. According to the brochure, the instrument uses a 8x768 pixel array with 100 ps temporal resolution in conjunction with a 532 nm pulsed laser at 250kHz repetition rate with 150 ps pulses.

The SPAD array comes from the university of Oulu's department of electrical engineering and is based upon a 2x4x128 pixel array that has a temporal resolution and ungated dark counts of 50k cps [65]. At 250 kHz repetition rate with 150 ps laser pulses, a total background reduction of 4 us/150 ps = 2600 X making the gated dark count as low as 20 cps. The high pulse energy of the low repetition rate 532 nm laser coupled with the 150 ps resolution makes it unsuitable for delicate samples with short lifetimes.

Single pixel detection systems such as single photon avalanche diodes and photo multiplier tubes offer low noise, good temporal resolution and high detection probabilities. They can be operated in TCSPC mode, easy to implement and commercially available. However, single element detectors require that the whole spectrum be scanned sequentially to obtain a full spectrum resulting in long measurement times for full spectra.

3.1.4 Potential solution using DMD

When the spectral features of interest are known, a single pixel detector with a suitable optical filter would provide a simple solution. A single pixel detector, operating in TCSPC mode could provide the best temporal resolution current technology allows and the issues not yet resolved in SPAD arrays are no longer relevant.

DMD and SLM based Compressive Raman detection combines single pixel detectors with a software configurable optical filter to provide signal enhancement by multiplexing multiple spectral features onto a single detector. The resulting signal consists of more relevant photons, while providing only one pixel worth of read and thermal noise. In fact, the binary operation of a SPAD requires no ADC and therefore generates no read noise. Compressive detection methods have demonstrated improvements in both the limit of detection and acquisition times when compared with CCD and EMCCD. [54]

A DMD coupled with a single pixel detector allows for >92 % fill factor, best possible temporal resolution, lowest thermal noise, and zero read noise. Although the initial sequential scanning of a full spectrum would take much longer than for an array-based detector, once the spectral features of interest are identified they can be simultaneously directed towards the single pixel detector the resultant increased signal can be acquired in less time.

In summary, the combination of a spatial light modulator with a single pixel detector operating in TCSPC has the potential to provide high throughput, high temporal resolution and compact design potentially fulfilling the criteria set in the goals.

3.2 Component selection - Detectors

Single photon avalanche diodes and photomultiplier tubes form the basis for almost all detection methods that require high accuracy in the temporal dimension with the Kerr gate being the main exception. Their basic operation and key properties are discussed here. At 775 nm the Raman fingerprint region of 400-1800 cm^{-1} spans a wavelength range of 800-900 nm; with this in mind we compare the specifications of potential detectors.

3.2.1 SPADS

Single photon avalanche diodes (SPAD) are solid state detectors capable of detecting extremely low intensity signals of down to a single photon. A p-n junction is reverse biased to the point just below the breakdown voltage (Vb). An incident photon at the depletion region generates an electron hole pair that accelerates under the high potential and results in charge carrier multiplication through impact ionization. The subsequent avalanche of current results in a rapidly rising sub nanosecond pulse with the leading edge of the pulse marking the time of arrival of the incident photon. Additional circuitry is required to quench the current flow and to return the detector to its initial state via control of the bias voltage. The quenching circuit is an integral part of most commercially available detectors. The processes involved in a detection event are;

1. Incident photon generates electron hole pair.
2. Impact ionization result in an avalanche of current
3. Quenching circuit detects avalanche and generates synchronised TTL or other standardized output pulse.
4. Bias voltage is reduced to below Vb
5. Delay before increasing bias voltage to initial state.

Dead time

Between two consecutive output events there is a minimum delay time due to the requirements of the quenching circuit that is known as the detectors dead time (d_t). For the MPD100CTE there is approximately 80ns dead time between the detection of an event and the time at which the detector is ready to detect the next event. This of course means that there is a maximum count rate of ~12.5MHz ($1/d_t$).

Correction factor

During the dead time, the bias voltage is reduced to below the breakdown voltage, thus any photons incident on the detector during this period are not detected. Consequently, the measured value will be less than the actual value. This effect is nonlinear, and for count rates of less than 1% of the detectors maximum, the effect is negligible. The actual count can be calculated by Equation 3.2, where the correction factor is the ratio

of the actual to measured count. The correction factor as a function of measured counts is plotted for two regimes in Figure 3.2a & 3.2b to illustrate the effect.

$$R_{actual} = \frac{R_{measured}}{1 - R_{measured} \cdot T_D} \qquad [3.2]$$

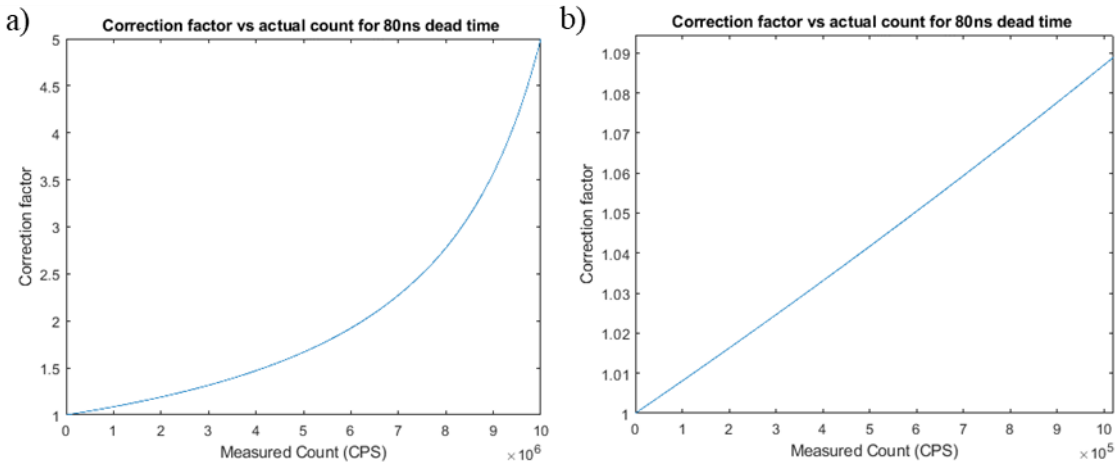

Figure 3.2. Correction factor vs measured count for a spad with 80 ns dead time. (a) The nonlinear effect on the measured count rate due to the dead time is clearly observed for count rates above 50% of the maximum count rate. (b) For count rates of less than 1% of the detector maximum it can be see the effect is approximately linear and the measured count differs from the actual count by less than 1%.

Afterpulsing

Impurities in the gain medium of the detector can lead to charge carriers becoming trapped. The release of these charge carriers can trigger an avalanche resulting in an unwanted detection event known as afterpulsing. This effect can be seen as the asymmetry in the instrument response function in Figure 3.5a. As thermal energy helps release the trapped charge carriers the effect is more pronounced in cooled detectors

3.2.2 PMT – photo multiplier tubes

A photon incident on a PMTs light window strike a phosphor cathode and will produce a photo electron with a probability equal the QE of the phosphor. This photoelectron is focused and accelerated through a series of dynodes where more electrons are generated. As there are multiple paths each electron can take, the resultant signal generated has a temporal distribution related to the transit time spread (TTS) of the

electrons. This results in a broadening of the temporal response of the detector as shown by Figure 3.3. and is affected by the emission angle distribution and the initial velocity distribution of both photoelectrons and secondary electrons.

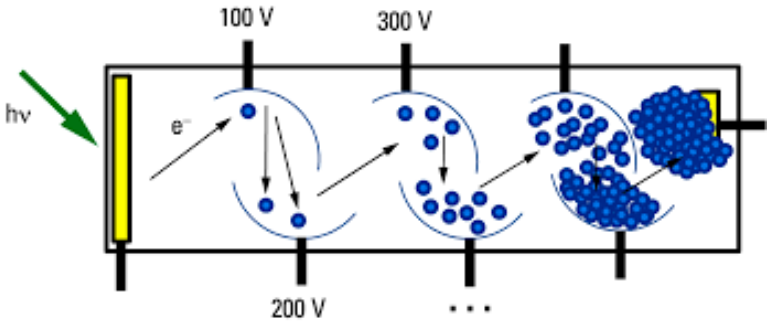

Figure 3.3 Image of PMT structure

Micro channel plate-photomultiplier tube (MCP PMT)

By utilizing a series of microchannels the electrons are multiplied and accelerated in a smaller region therefore reducing the transit time spread and improving temporal resolution (figure 2.7) . Microchannel plates form integral components of other high-speed detectors such as the image intensifiers used in iCCD detectors and ultra-low level light imaging. Advantages of MCPs are fast time response, large detector area, stability in high magnetic fields and high spatial resolution in two dimensions. Disadvantages include, the requirement of a large cooler, poor collection efficiency, low QE at NIR and cost.

Advantages of SPADs are fast time response, high detection efficiency (Figure 3.5b), low noise, simplicity, and cost. The main disadvantage of a SPAD is the small detection area of 25-100 μm^2.

A comparison of the temporal response of both a MCP PMT (R3809U-50) and a SPAD (PDM 50CT) has been performed by PicoQuant [66] and the results show the SPAD to be approximately equivalent in temporal resolution at 670 nm (Figure 3.5 a).

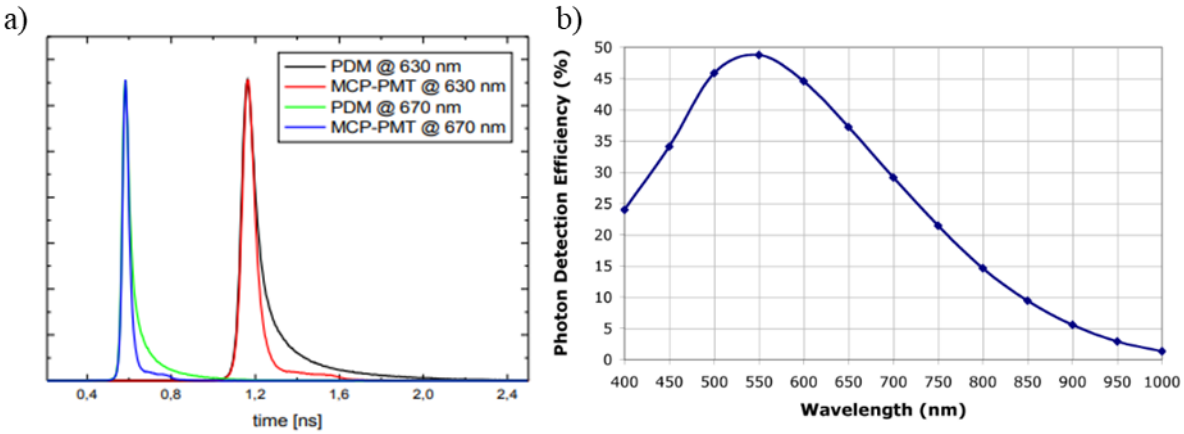

Figure 3.5. a) Comparison of the temporal response of a MCP PMT and the PDM50ct SPAD. Taken from a technical note produced by PicoQuant. [66] b) Photon detection efficiency of the PDM series of SPADS by MPD, taken from data sheet. [67]

The key considerations and specifications from three potential detectors are shown in Table 3.2. The MPD 100CTE SPAD from micro photon devices (MPD), the COUNT T-series SPAD from Laser Components and the R3809U-61 microchannel PMT from Hamamatsu. When compared to the best MCP PMT available, the single photon avalanche diode (SPAD) offers equivalent temporal resolution, superior detection efficiency at NIR wavelengths, a more compact physical form and lower cost.

When selecting a pulsed laser, the specifications were chosen with the detector in mind. The Katana laser produced by OneFive has 35 ps pulses with a selection of wavelengths and repetition rates and an average output power of 65 mW. The full specifications of the delivered laser are shown in Table 3.3.

Table 3.2 Key considerations and specifications of potential detectors.

	PDM 100CTE	MCP PMT	COUNT T
Detector Area	100 µm x 100 µm	10 mm	100 µm x 100 µm
Temporal resolution	<50 ps	<150 ps	350 ps
QE @ 800-900 nm	15-10%	0.1 -0.2%	70%
Dark count rate	15 cps	20 cps	20 cps
Deadtime	77 ns	1 ms	43 ns
Pulse width	20 ns	20 ns	17 ns
Cost	Low (£5000)	High >£30000	Low (£5000)

Table 3.3. Katana 775 pulsed laser delivered specifications.

Parameter	Unit	Specification	Test Data
Pulse duration	ps	35±15	30.7
Average power	mW	>40	65
Wavelength	nm	775±2	774.056
Spectral bandwidth	nm	<0.2	0.081
Pulse Repetition rate	MHz	1-10	0.9-11
M2		<1.3	1.06,1.04
Pulse to timing jitter	ps	<5	6.8

3.3 Theoretical estimations of performance

Using a NIR laser with a 30 ps pulse width in conjunction with a SPAD of temporal resolution of 50 ps we can expect an IRF of $(30^2+50^2)^{1/2}$ =60 ps FWHM. Based upon the lifetimes in the literature and the expected IRF we can make some estimations of the amount of fluorescence suppression possible.

Below, we compare the potential Raman signal to noise of time gating using a SPAD to a CCD at 785 nm excitation and 1064 nm excitation using an InGaAs detector array. This is done for a range of Raman and fluorescence intensities to determine the signal regimes at which the best advantages may be gained.

Detector quantum efficiency, read noise, thermal noise, Raman photon shot noise and fluorescence shot noise are considered for each regime. The specifications used were taken from the data sheets and are shown in Table 3.4.

It is assumed that the fluorescence intensity at 1064 nm is 500x less than that at 785 nm and the Raman photons detected at 1064 have been corrected to account for the λ^{-4} scattering reduction.

The amount of fluorescence suppression provided by time gating the SPAD is calculated based upon the FWHM of the detectors and a 1ns fluorophore.

To get a realistic idea of the number of photons we can expect to be dealing with, a reference spectrum of polystyrene is measured. Considering the number of photons falling on a single column of pixels associated with the 1454 cm^{-1} wavenumber and after compensating for quantum efficiency and the sensitivity of the CCD at 40 mW, around 15000 incident photons per second are measured. Polystyrene is of course, a strong Raman scatterer so this amount of signal is on the upper side of what is to be expected. In fact, for biological samples 1-2 orders of magnitude less signal is to be expected.

If P Raman photons per second are incident on one pixel of CCD detector with quantum efficiency Q, a signal consisting of N_e electrons is generated and stored in a well.

$$N_e(t) = Q \cdot P \cdot t \quad [3.3]$$

The photon shot noise on the signal is given by;

$$\delta_{signal} = \sqrt{Q \cdot P \cdot t} \quad [3.4]$$

For a sample with fluorescence background consisting of $P_{fluorescence}$ photons there is an additional photon shot noise of,

$$\delta_{fluorescnce} = \sqrt{Q \cdot P_{fluorescence} \cdot t} \quad [3.5]$$

The total noise is sum of the read noise, thermal noise and photon shot noise from all sources.

$$\delta_{total}\sqrt{{\delta_{dark}}^2 + {\delta_{read}}^2 + {\delta_{signal}}^2 + {\delta_{fluorescence}}^2} \quad [3.6]$$

The signal to noise is, therefore.

$$\frac{S}{N} = \frac{Q \cdot P \cdot t}{\sqrt{{\delta_{dark}}^2 + {\delta_{read}}^2 + {\delta_{signal}}^2 + {\delta_{fluorescence}}^2}} \quad [3.7]$$

Table [3.4] Specifications of CCD, InGaAs, and SPAD detectors

	DU401 785	Du491A(1064)	SPAD PDM100CTE	SPAD COUNT -T
Read Noise	5-10	580/8150	0	0
Dark count	0.013	12k	10	13
QE (800-900 nm)	95-85	85	15-10	70
Pixel size	26x26µm	25x500	100 x 100µm	100 x 100µm
Sensitivity (e^- per count)	2.5-18.2	2800/90	1	1
Temporal resolution	0	0	50 ps	400 ps

The count value read from the CCD varies depending on the settings used. Photoelectrons generated are stored in wells. The sensitivity setting defines the A/D convertor resolution and therefore the amount electrons required per count. For the SPAD, no AD convertor exists. As one photoelectron can trigger an avalanche event the sensitivity is classed as one count equals one incident photon detected.

The signal to noise ratio is calculated for 785 nm excited Raman with CCD detection, 785 nm excited Raman with SPAD detection and for 1064 nm excited Raman with InGaAs detection based upon the signal falling across a region of just one pixel (*P*).

1)No fluorescence

For signal consisting solely of Raman photons, Figure 3.6) shows that the SNR of the InGaAs detector is significantly less than both the SPAD and CCD due to the large amounts of read and thermal noise. In the high signal regime (>10^4 photons per second per pixel) where the photon shot noise becomes comparable to the read and thermal noise the performance of the InGaAs becomes comparable to the SPAD with the lowest detection efficiency of ~10%.

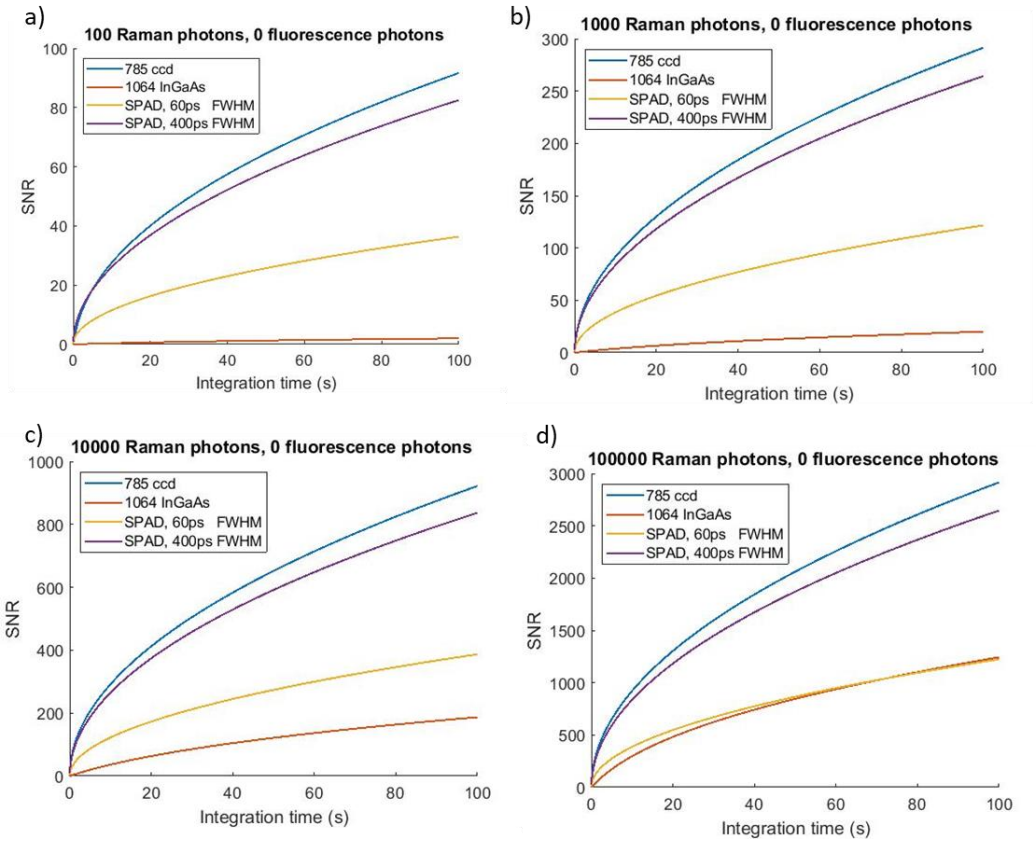

Figure 3.6. SNR comparison of one pixel of the SPADs and CCD at 785 nm and 1064 nm InGaAs detectors for varying levels of Raman intensity with no background from fluorescence. a) 100 incident Raman photons per pixel per second. b) 1000 incident Raman photons per second per pixel. c) 10000 incident Raman photons per second per pixel. d) 100000 incident Raman photons per second per pixel.

2) Low levels of fluorescence

For low levels of fluorescence of 1000 photons per pixel per second, the photon shot noise contribution from fluorescence has little effect and the results are the same as for no fluorescence with a highly efficient CCD outperforming other detection methods.

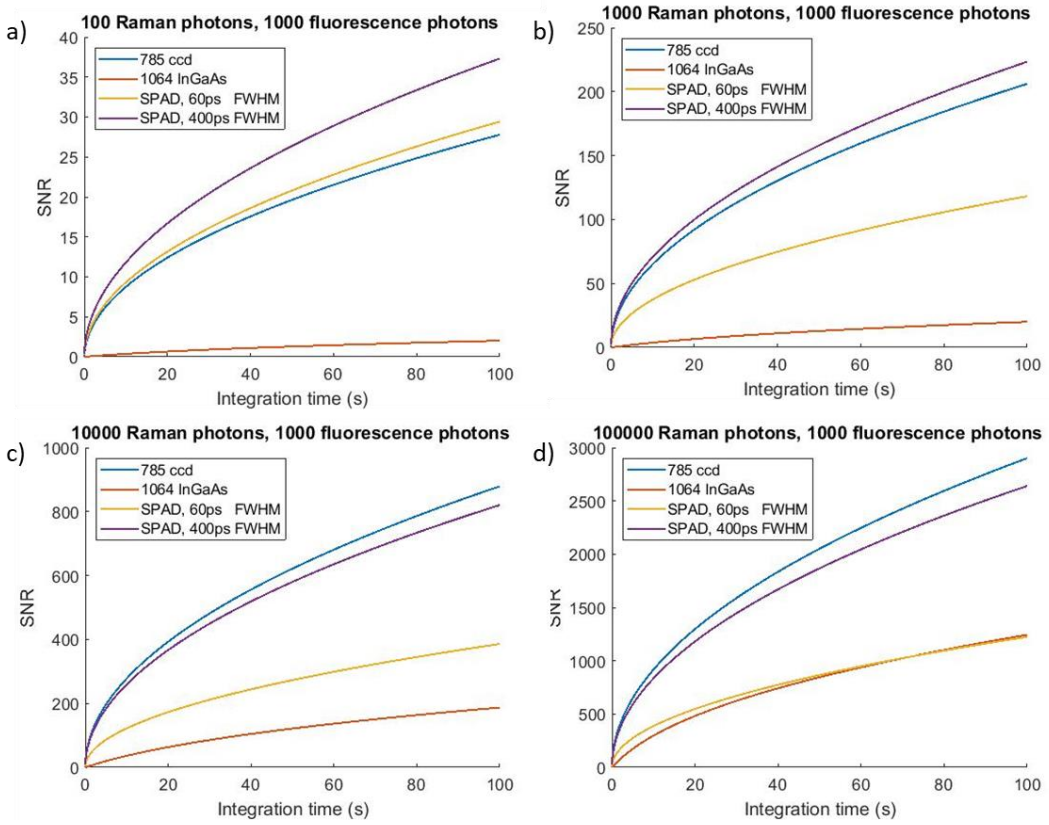

Figure 3.7 SNR comparison of one pixel of the SPAD, CCD at 785 nm and 1064 nm InGaAs for varying levels of Raman intensity with low levels (1000 fluorescence photons per pixel per second) of fluorescence background from a fluorophore with a 1ns lifetime and time gating equal to the FWHM of the detectors. a) 100 incident Raman photons. b) 1000 incident Raman photons. c) 10000 incident Raman photons. d) 100000 Raman photons per second, per pixel.

3) Moderate levels of fluorescence

For moderate levels of background fluorescence of 10,000 photons (P^{-1} s^{-1}), the shot noise from the fluorescence becomes relevant in the low signal regime of 100 to 1000 Raman photons. At these levels both SPADs offer an advantage in signal to noise over the CCD. For higher signal levels of 100000 Raman photons per second the CCD outperforms the SPADs with time gating.

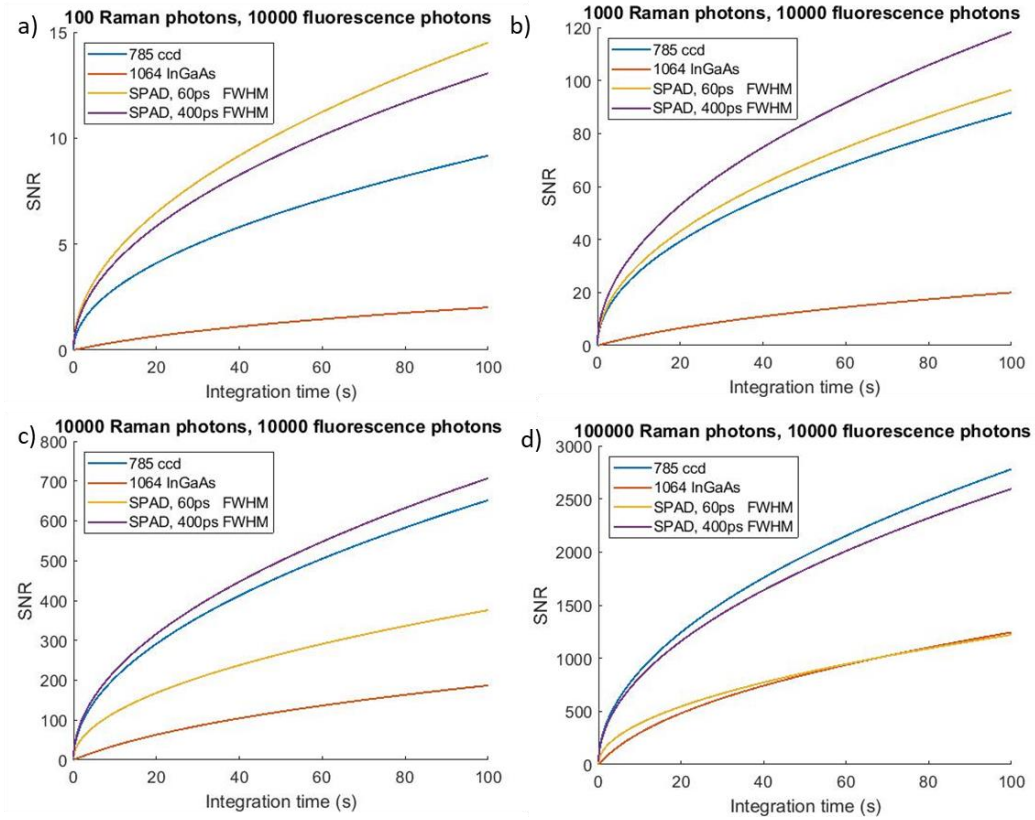

Figure 3.8 SNR comparison of one pixel of the SPAD, CCD at 785 nm and 1064 InGaAs for varying levels of Raman intensity with moderate levels of fluorescence background (10000 fluorescence photons per pixel per second) from a fluorophore with a 1ns lifetime and time gating equal to the FWHM of the detectors. a) 100 incident Raman photons b) 1000 incident Raman photons. c) 10000 Raman photons. d) 100 000 Raman photons, per pixel per second.

4) High levels of fluorescence

For high levels of fluorescence of 100000 photons (P^{-1} s^{-1}) there is a signal to noise advantage to be gained by using the SPAD with time gating over both the CCD and the 1064 InGaAs in the low Raman signal regimes. For high levels of Raman signal, the more sensitive SPAD and the CCD are similar in signal to noise while the SPAD with lower detection efficiency is approximately equivalent to the 1064 nm InGaAs

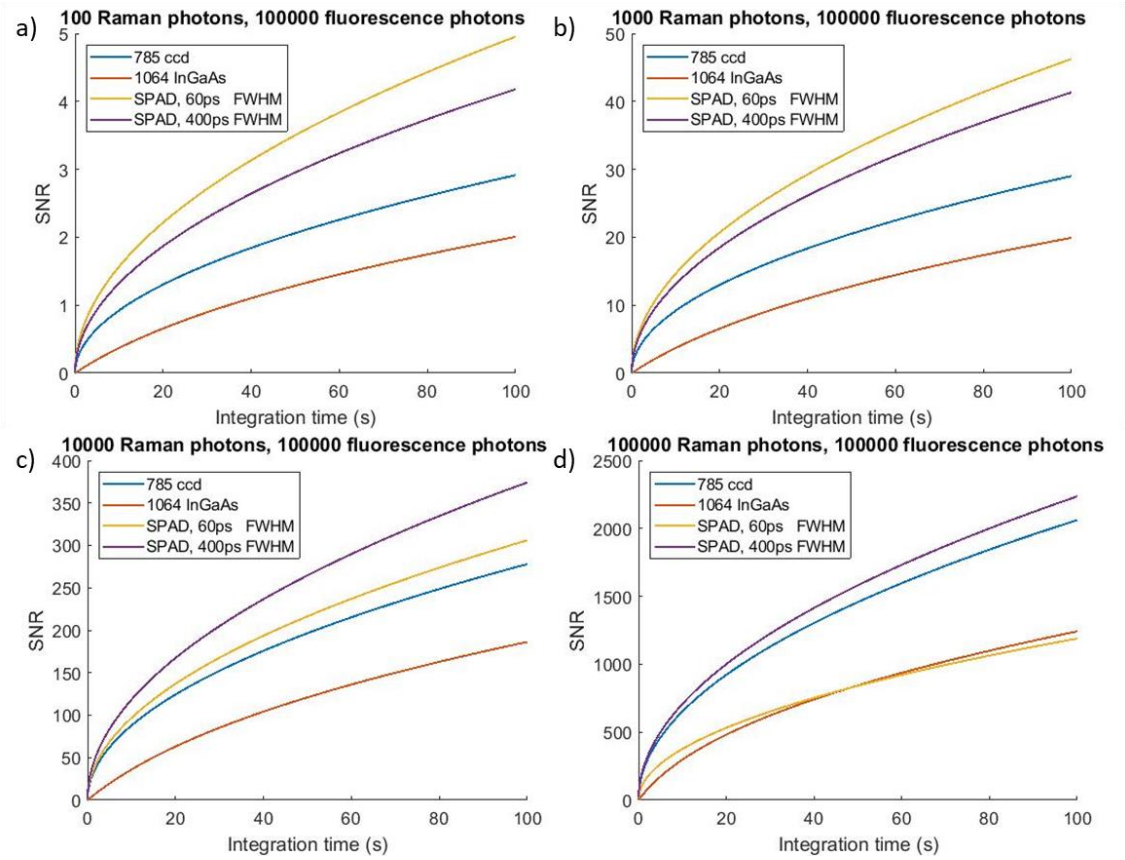

Figure 3.9 SNR comparison of one pixel of the SPAD, CCD at 785 nm and 1064 InGaAs for varying levels of Raman intensity with high levels of fluorescence background (100,000 fluorescence photons per pixel per second) from a fluorophore with a 1ns lifetime and time gating equal to the FWHM of the detectors. a) 100 incident Raman photons. b) 1000 incident Raman photons. c) 10000 Raman photons. d) 100000 Raman photons per pixel per second.

5)Extreme levels of background

Considering the extreme case, where the fluorescence intensity is of the order of the square of the Raman intensity at 1s for all Raman signal levels (Figure 3.10). In this case, at 1 second integration, the shot noise from the fluorescence is equivalent to the Raman signal. As time increases, the photon shot noise increases as the square root of the intensity and the signal to noise increases. In the low signal regimes of 500 Raman photons (P^{-1} s^{-1}) there is a signal to noise advantage to be gained by time gating using a spad over both the CCD and the 1064 InGaAs detector. For moderate to high levels of Raman scattering the 1064 nm InGaAs detector offers an advantage over both CCD and time gated SPADs in this situation.

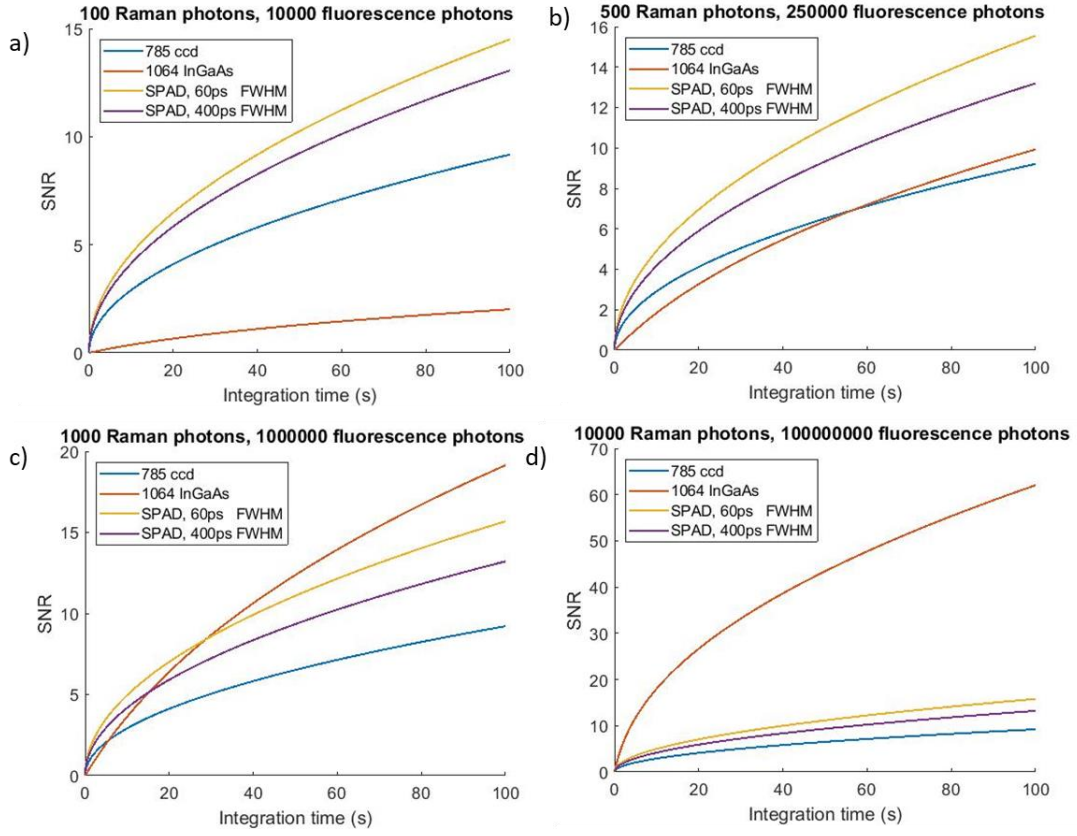

Figure 3.10 SNR comparison of one pixel of the SPAD, CCD at 785 nm and 1064 InGaAs for varying levels of Raman intensity with extreme levels of fluorescence background from a fluorophore with a 1ns lifetime and time gating equal to the FWHM of the detectors. a) 100 Raman photons with 100^2 fluorescence photons per second per pixel. b) 500 Raman photons with 500^2 fluorescence photons per second per pixel. c) 1000 Raman photons with 1000^2 fluorescence photons per second per pixel. d) 10000 Raman photons and 10000^2 fluorescence photons per second per pixel.

Summary of SNR comparison

The calculations show that time gating with a SPAD at 785 nm offers a potential signal to noise advantage over the InGaAs array detector at 1064 nm for all levels of fluorescence in the low Raman signal regimes.

For low levels of fluorescence background levels, the CCD detector offers superior performance thanks to the high QE and low read and thermal noise. When the fluorescence shot noise becomes the dominant source of noise, time gating using a SPAD offers the signal to noise advantage.

For samples with high levels of Raman scattering and extreme levels of background fluorescence there is an advantage to 1064 nm dispersive Raman using an InGaAs detector. If IR detector arrays could be produced with low read and thermal noise, then 1064 nm Raman would offer superior performance in almost all signal and noise regimes.

Further SNR plot are attached in the appendix for fluorophores with 0.3 & 3 ns lifetimes.

3.4 Instrument Design

A Nikon Eclipse inverted microscope and motorized stage was used to excite and collect the Raman scattered light Figure (3.11). The pulsed laser is directed into the microscope via the dichroic mirror (DM) where it was focused onto the sample on the x,y translation stage via an objective. Scattered and fluorescence photons are collected by the objective, the collimated light passes through the dichroic mirror and the long pass filter (LPF) before being focused onto a fiber coupling via lens (L) (Thorlabs AC127-0-30-B).

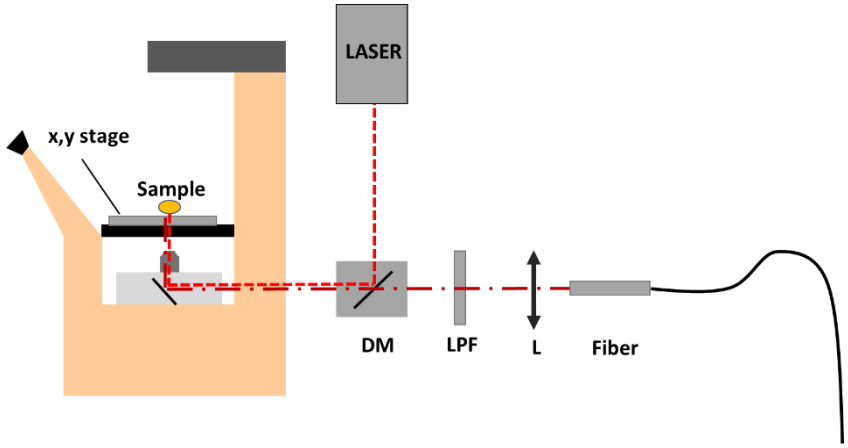

Figure 3.11. Schematic of inverted Raman microscope. DM – Dichroic mirror. LPF – long pass filter. L – focusing lens.

Figure 3.12 shows the basic layout of the compressive detection Raman system. A standard Czerny-Turner spectrometer design is used to disperse and focus the spectrum. The Raman spectrum is fiber coupled into the entrance port of the spectrometer at (1) where it is collimated by a concaved mirror (M1) and split into its component spectral features by the diffraction grating (G1). The resultant spectral features are then focused onto a CCD detector by the concaved mirror (M2). An optional extra of the spectrometer includes a software-controlled flipper mirror (FM) to direct the spectra away from the CCD and towards the side port of the spectrometer.

The spectra from the side port will then be focused onto the DMD mirrors for digital light processing via the relay lenses (L1 and L2). The most obvious optical design would be to simply take the spectra focused onto the DMD and focus it onto the detector element using two more lenses (L3 and L4) as shown in Figure 3.12.

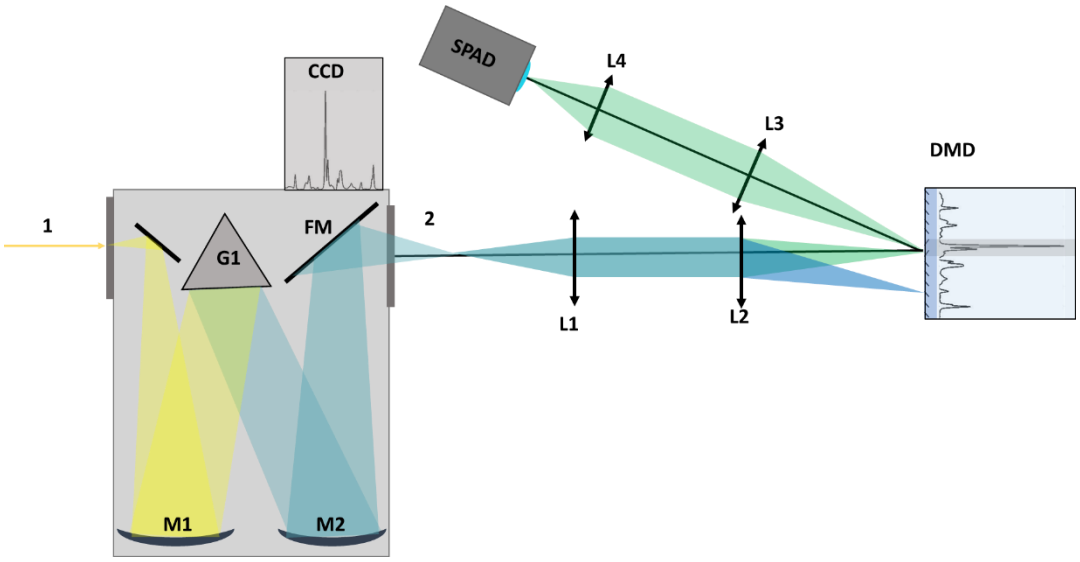

Figure 3.12. Initial design of compressive Raman addition to a standard Czerny turner spectrometer. The output from the spectrometer is projected onto the DMD (not to scale) via relay lenses L1 & L2. The filtered spectrum is then focused onto the detector.

Although this simple design seems reasonable, there is a difficulty in collecting and focusing the whole Raman spectrum down to a small detector using lenses alone without significant loss of light. To understand the limitations, we need to consider the size of the spectrum imaged onto the DMD, the detector area and the angles at which the light is emitted and can be detected.

When designing and building the prototype, the detector was the 50 µm variant PDM50CT and the DMD was the Texas Instruments DLP3000 with a width of 6.57 mm (Figure 3.13a)

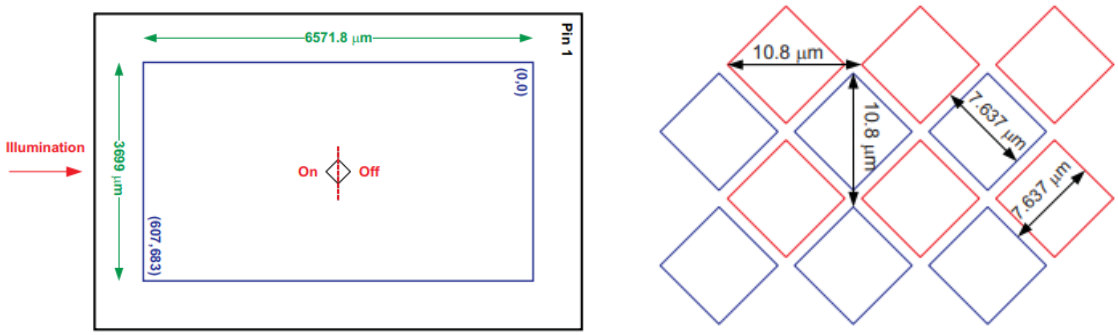

Figure 6. DLP3000 Micromirror Active Area

Figure 3.13 Dimensions of the DLP3000 DMD from Texas Instruments datasheet. [68]

In order to focus the 6.5 mm width of the Raman spectrum projected the DMD to less than 50 µm, a magnification of ~ 1/150X would be needed. For a microscope type lens system where image and object lie in the focal plane of the lens, such as the one shown in Figure 3.14, the magnification is given by the ratio of the focal length of the two lenses L3 & L4.

$$M = -\frac{s'}{s} = \frac{f_{L4}}{f_{L3}} = \frac{1}{150} \qquad [3.8]$$

To focus the image onto the SPAD, a long working distance of at least 6 mm is required. A potential microscope objective available for this application is the 100x Mitutoyo Plan Apo NIR with a focal length of 2 mm and a NA of 0.7. We would therefore require L3 to be, $150 \times L4 = 150 \times 2 = 300\ mm$. While this focal length is reasonable, a lens placed at 300 mm would have to be $300/4 = 75mm$ in diameter in order to collect all of the emitted light.

Considering the detector, a 2 mm focal length with a NA of 0.7 results in a beam radius of $2\ mm \times \tan(44.4)$=1.95 mm or a beam diameter of 3.93 mm.

Such an optical system would provide the required magnification but clearly only a small portion of the light will make it through 3.9/75 = 5.2%. This value is consistent with calculations using a demonstration version of Zemax Optics Studio. The optical

model (Figure 3.14) shows the light path for the design in Figure 3.12 using lenses of L3=300 mm and L4=2 mm

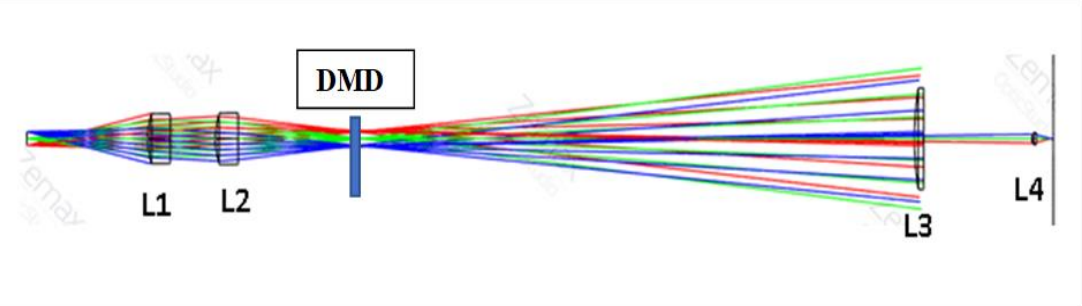

Figure 3.14. Zemax optical model of a viable, low throughput design where it can clearly be seen that only a small portion of light passes through L4 and makes it to the detector.

To overcome these limitations, several options were investigated, and two viable options were found.

1. Use a larger detector.

The micro channel plate photomultiplier tube (MCP PMT). The R3809u61 provides the best detection efficiency for our wavelength of interest but quantum efficiency drops off from 10%- 2% for 850-900 nm. In addition, it would require a cooling system to achieve a reasonable dark count. These properties result in an inefficient, expensive, bulky system.

2. Recombine the spectral components into a single collimated beam, which can then be efficiently focused on a small detector.

3.4.2 Recombination of a spectrum

With reference to Figure 3.15, light from any point of an object in the focal plane of a lens will diverge at an angle $\theta = y/f$. If we imagine the DMD as the object in the plane, each point on the DMD (Δy), corresponds to a different wavelength, we

therefore have a wavelength dependent divergence angle. By matching this divergence to the dispersion of a prism or diffraction grating it is possible to successfully compensate and, recombine the spectra to form a collimated polychromatic beam.

A perfectly collimated beam can be theoretically focused to a single diffraction limited spot. Although, all we need to achieve is enough dispersion compensation to allow the output beam to focused to the small area of the detector.

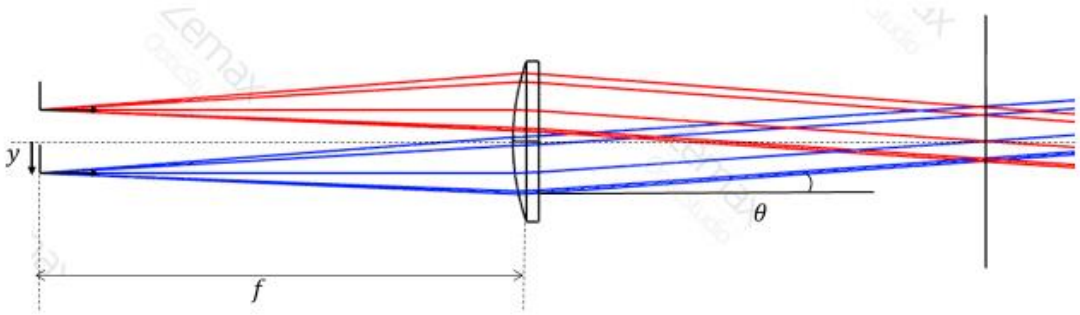

Figure 3.15. Ray diagram illustrating the divergence of light from an object in the focal plane of a lens (produced in Zemax demonstration version).

To initially test the idea, a prism-based instrument was built using a 532 nm laser for excitation. To determine the amount of dispersion compensation we need to determine the size of the spectrum projected onto the DMD array. To do this we need to know the wavelength range, diffraction grating used and the focal length of the spectrometer. The Andor Shamrock 303i has a focal length of 300 mm and the light exits at f/4. That is, the light leaving the spectrometer exits in a cone with a half angle of arctan (1/8) = 0.124 = 7.125 degrees.

The amount of angular dispersion for a given wavelength range is defined by;

$$\mathfrak{D} \equiv \frac{d\theta_m}{d\lambda} \qquad [3.9]$$

Using the grating equation; $a \cdot \sin(\theta) = m\lambda$ [3.10]

where ***a*** is the grating constant or groove separation and m is the diffraction order.

We can therefore conclude;

$$\mathfrak{D} = \frac{m}{a \cos \theta_m} \qquad [3.11]$$

For a grating with 299 lines/mm

$$a = \frac{1}{299 mm^{-1}} = 3.3 \times 10^{-3} mm = 3.3 \times 10^{-6} m$$

First to validate the approach a Hg lamp was used. Using the 579.96 nm Hg line as our central point.

$$sin\theta = \frac{m\lambda}{a} = \frac{577 \times 10^{-9}}{3.3 \times 10^{-6}} = 0.1748$$

Thus, θ_1 =10.07° and $cos\theta = 0.9846$

The angular dispersion in the wavelength region around 570 nm can now be calculated:

$$\mathfrak{D} = \frac{m}{a \cos \theta_m} = \frac{1}{3.3 \times 10^{-6} \, (0.987)} = 307769 \, rad/m$$

Or

$$\mathfrak{D} = 3.07777 \times 10^{-4} \, \frac{rad}{nm} \times \frac{180}{\pi rad} = 0.0176° nm^{-1}$$

Repeating these calculations for our wavelengths of interest we determine angular dispersion of a grating therefore, the size of the image at the exit of the spectrometer

(Table 3.5). This is done for the wavelength range corresponding to the Raman fingerprint region for both the 532 nm prototype and the 775 nm NIR version.

Table 3.5. Calculated dispersion of 299 and 599 lines /mm gratings for the wavelengths of interest. Final column (Y1x2) shows the total image size produced by our 303 mm focal length spectrograph.

Excitation wavelength	Midpoint (nm)	Range (nm)	Grating Grooves per mm	a	Sin theta	$\mathfrak{D}$ Rad/m	$\mathfrak{D}$ $°nm^{-1}$	Total (°)	Total (rads)	Y1x2 (f=303mm) (mm)
532 nm	571	32	299	$3.3 \times 10^{-6}m$	0.173	307022	0.0176	0.56	0.0098	2.97
532 nm	571	32	599	$1.67 \times 10^{-6}m$	0.342	637024	0.0365	1.168	0.020	6.06
775 nm	863	75	299	$3.3 \times 10^{-6}m$	0.261	314021	0.018	1.35	0.0236	7.1
775 nm	863	75	599	$1.67 \times 10^{-6}m$	0.517	699535	0.04	3	0.0525	15.9

Considering the width of the DMD, the grating is selected such that it gives the correct amount of dispersion. Based upon the values determined in Table 3.5 we can see that a 600 grooves per mm grating results in a Raman spectrum dispersed over 6 mm at 532 nm. For 775 nm excitation a grating of 300 grooves per mm is required to project as much of the fingerprint region as possible onto the DMD while maintaining the best spectral resolution.

Dispersion of a prism

To calculate the dispersion of a prism, the angular deviation (δ) must be calculated for each wavelength. When the light runs parallel to the base of the prism a condition arises which is known as the angle of least deviation (Figure 3.16a). Figure 3.16b shows the index of refraction v wavelength for SF11 glass, as the angular deviation is dependent on the refractive index, the resulting dispersion of a spectrum by a prism is nonlinear. Equations 3.12 & 3.13 show the relationship between refractive index, apex angle and the angular deviation(δ).

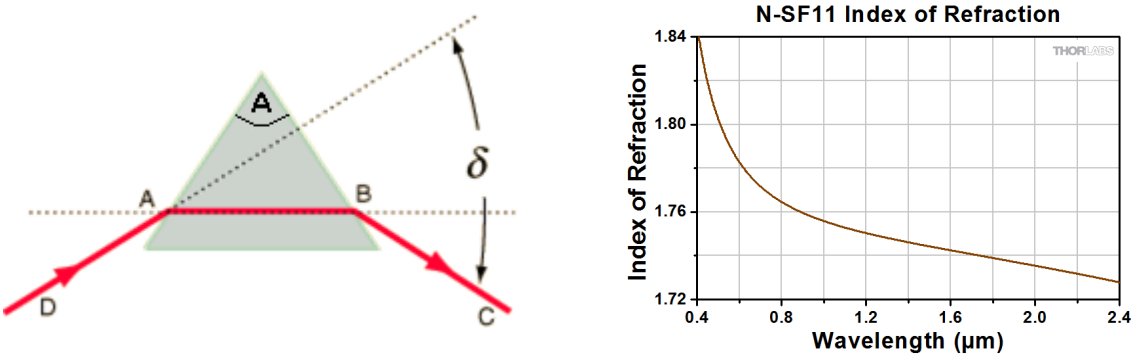

Figure 3.16a. Path of least deviation of light through a prism [69]. 3.16b. Index of refraction v wavelength for sf11 glass.

$$sin\left[\frac{A+\delta}{2}\right] = n \cdot \sin\left[\frac{A}{2}\right] \qquad [3.12]$$

$$n = \frac{\sin\left[(A+\delta)/2\right.}{\sin\left[\frac{A}{2}\right]}$$

$$\delta = 2 \cdot sin^{-1}\left[n \cdot \sin\left(\frac{A}{2}\right)\right] - A \qquad [3.13]$$

Using equation [3.13], the angle of least deviation was calculated for various prism glass types and wavelengths of interest (Table 3.6). The 546 nm & 579 nm lines from

a mercury lamp span the same wavelength region as the 532 nm excited Raman fingerprint regions, allowing the initial design to be testing using a mercury reference lamp.

Table 3.6. Refractive index of common glass and the angle of least deviation for the wavelengths of interest produced by a mercury lamp and 775 nm excited Raman fingerprint region.

		Refractive index *(n)* & angle of least deviation (δ) (A=60°)					
Source	λ(nm)	n(SF10)	$\delta(SF10)$	n(SF11)	$\delta(SF11)$	n(BK7)	$\delta(BK7)$
Hg I	546.07	1.7343	60.2582	1.7919	67.264	1.5167	38.814
Hg I	576.96	1.7298	59.7426	1.7864	66.556	1.5173	38.690
Hg I	579.06	1.7294	59.6969	1.7861	66.518	1.5172	38.682
775 nm	826			1.7632	63.672		
775 nm	901			1.7596	63.236		
Dispersion $\frac{d\theta}{d\lambda}$		0.561°/33 nm	0.017	0.435/75 nm	0.0058		

Using this information, it is possible to determine the focal length of the lens required to match the dispersion of the prism. $f_3 = y_3/\theta_4$, where θ_4 is half the dispersion of the prism for a given wavelength range and $f_3$is the focal length of lens L3 (figure 3.17).

For example, if we wanted to recombine the spectrum of the 532 nm Raman fingerprint region (or Hg lamp) using a 300 lines/mm grating. Table 3.5 shows we have an image size (y_3) of 3 mm and Table 3.6 shows the prism disperses this wavelength range by 0.75 degrees (0.013 rads). We therefore select a lens with a focal length $f = y/\theta$ =3/0.013=230 mm so the wavelength dependant divergence corresponds to the dispersion of the prism (Figure 3.17)

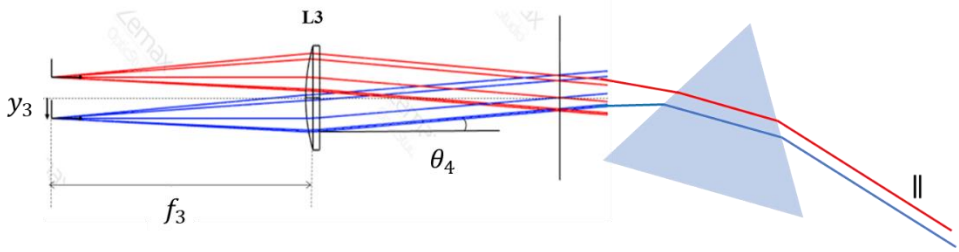

Figure 3.17 Example of matching the divergence of a spectrum of height y in the focal plane of a lens to the dispersion of prism.

To show we could successfully recombine the spectra in the manner discussed, the Andor Shamrock spectrograph was used to disperse the 546, 577 & 579 nm peaks from a mercury lamp. The spectra were then focused onto a CCD detector in three different configurations. The centre image of Figure 3.18 shows the Hg spectra with no prism in position. The top image shows how the spectral features are separated when the prism is inserted in an inverted position, finally the bottom image shows the recombination of the spectral features showing that we can successfully recombine the Hg spectra to form a single spot (in this example the optical system was adjusted so the separate features could be distinguished).

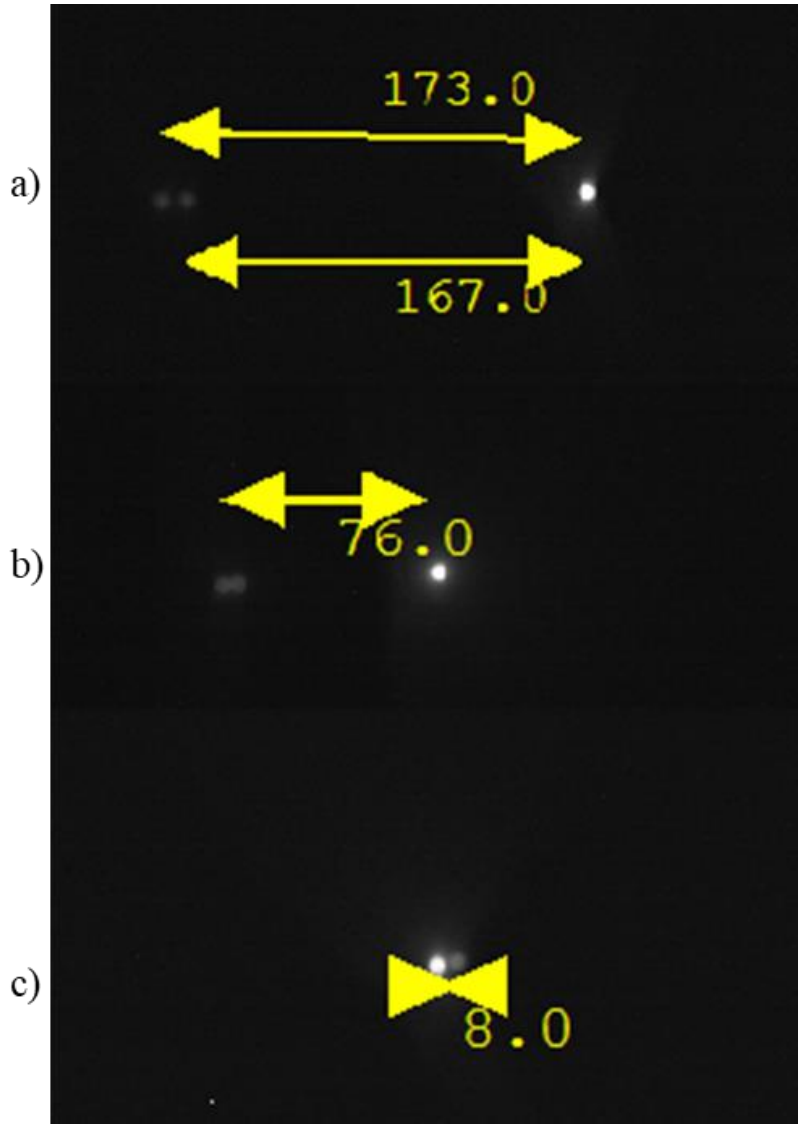

Figure 3.18. Monochrome camera image of Hg I lines (546,577 & 579 nm) at exit of spectrometer with and without recombining optics in place (300 lines per mm grating). The Hg lamp is fiber coupled to the spectrometer hence the circular image projection. a) with an SF11 prism installed in the inverted position the dispersion is increased. b) with no prism installed the amount of dispersion is determined by the spectrometer grating and focal length. c) With the prism installed to compensate for the dispersion of the grating, the spectral features overlap resulting in a single spot (in this case, the optics were slightly adjusted so the separate features could be distinguished.

With the concept shown to work as predicted using the Hg lamp, the first iteration of the DMD based Raman spectrometer was built (Figure 3.19) for use with 532 nm excitation wavelength and 599 lines per mm grating using standard components from the labs inventory L3 & L4 are 100 & 20 respectively.

As before, we need to match the divergence of the image to the dispersion of the prism. This time the image size is the full range of the DMD (6 mm) so a lens with a focal length $f = y/\theta$ = 6/0.013 = 462 mm is required. At 462 mm, the f/4 cone of light from the DMD would spread to a diameter of ~110 mm leading to a significant loss of throughput. To allow the use of a shorter focal length lens L3, two prisms were used in series to increase the amount of dispersion to be equivalent to the divergence of a lens with 100 mm focal length.

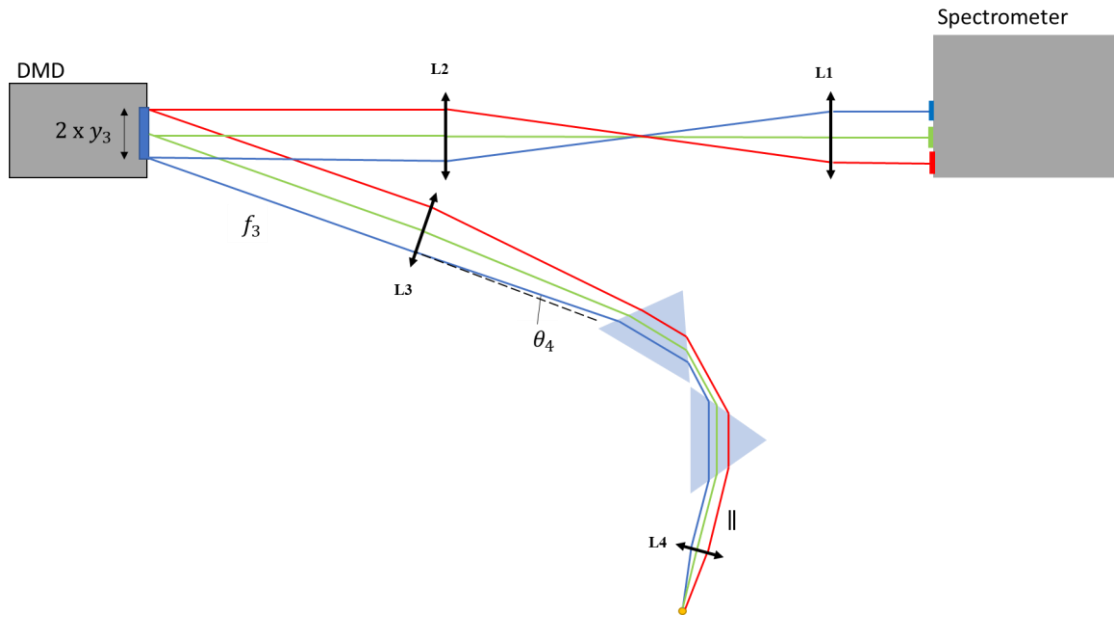

Figure 3.19 Schematic of design incorporating prisms as spectral recombination elements. Relay lenses L1 and L2 are used to extend the image of the spectrum produced by the spectrometer. The full spectral range is focused onto the DMD over a region 2 x y_3. The reflected light is collimated by lens L3 and diverges at an angle $\theta_4 = y_3/f_3$. The dispersion of the prisms compensates for the divergence and the light leaving the prisms is a collimated polychromatic beam. The beam is focused onto the detector by lens L4.

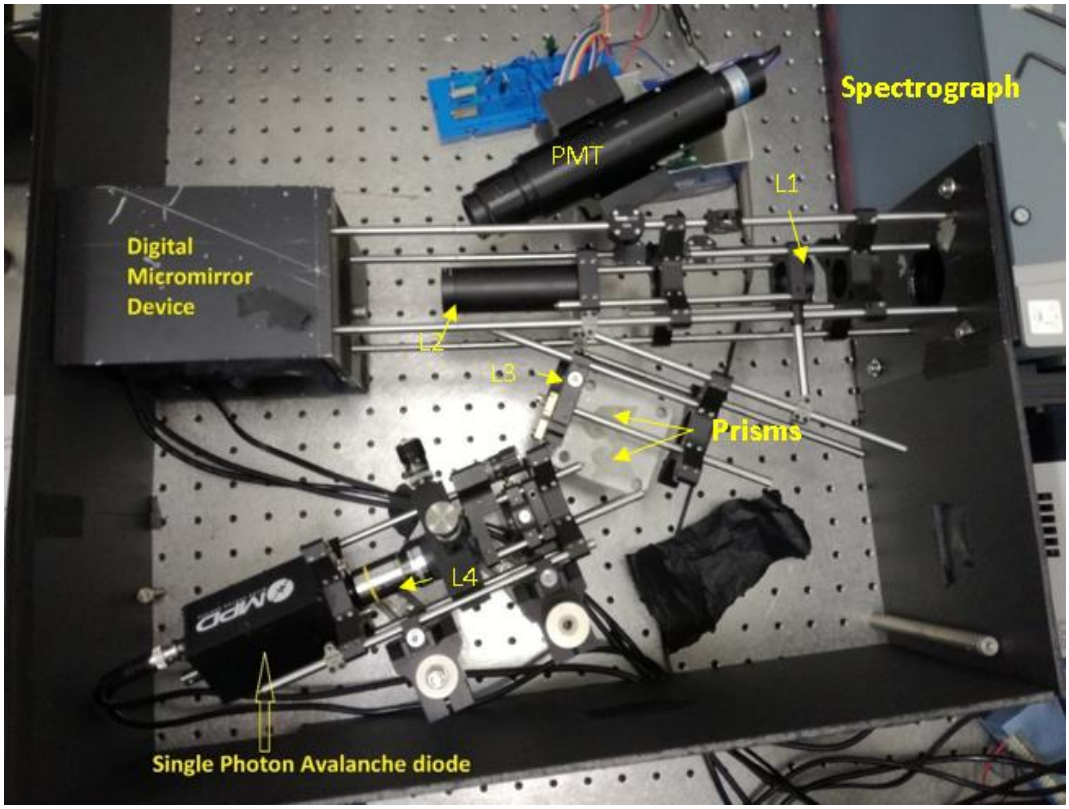

Figure 3.20. Layout of prototype CW DMD based spectrometer at 532 nm.

A LabVIEW program was written to operate the DMD mirrors via HDMI and record the number of photon events within a given time window while operating in continuous wave (CW) mode. The whole spectrum is scanned, by generating a rectangle of width W and sequentially projecting it across the DMD while recording the photon counts using a USB frequency counter (USB-CTR Series from measurement computing). The Raman spectra of polystyrene and benzene spectra were recorded using this method and compared to the Andor 401 CCD detector (Figure 3.21).

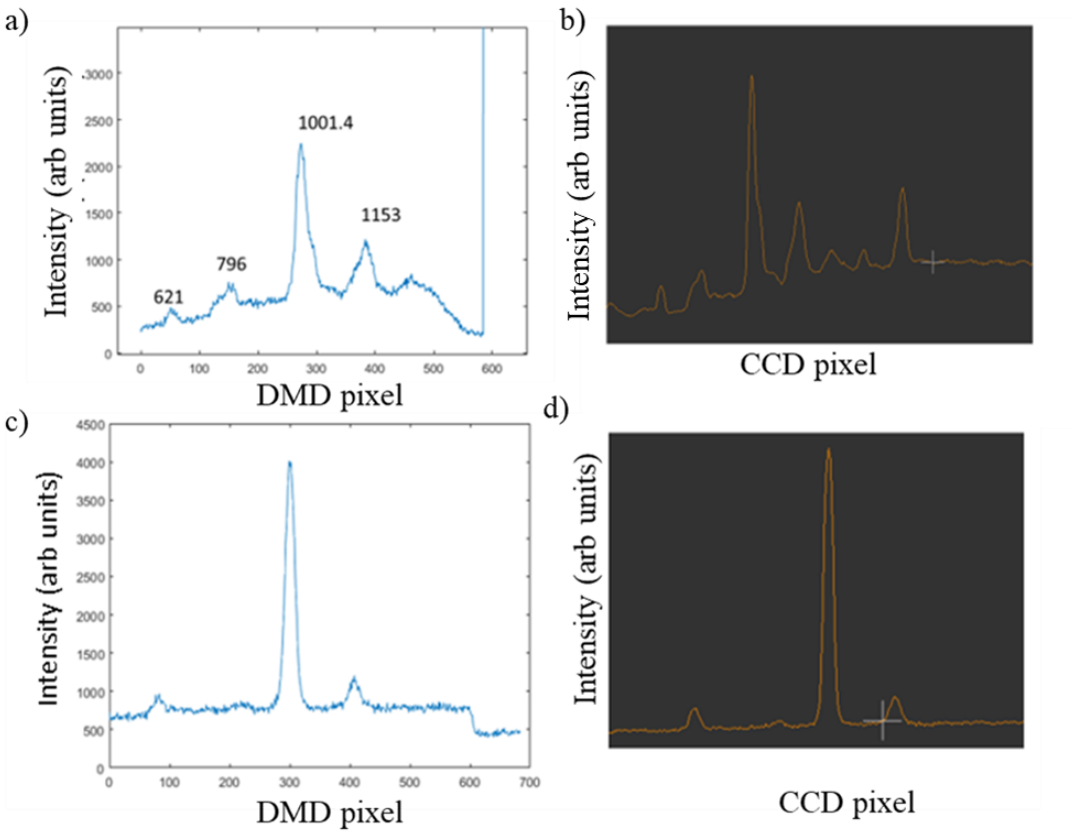

Figure 3.21. a) Raman spectra of polystyrene recorded using the DMD and single detector method in continuous mode. b) Raman spectra of polystyrene recorded using Andor CCD. c) Raman spectra of benzene recorded using DMD and single detector. d) Raman spectra of benzene recorded using Andor CCD detector.

The proof-of-concept system allowed approximately 800 cm^{-1} wavenumbers to be successfully focused onto the 50 µm SPAD with a visibly similar spectral resolution to the spectra acquired using the CCD. The optical system was then redesigned for use with the intended 775 nm pulsed laser excitation.

Zemax is a powerful tool used by professionals to design, simulate and measure the performance of optical systems. Commercially available lenses and optical elements are included in the built-in libraries along with the ability to construct custom optics elements such as prisms using a wide range of materials.

To aid in the design process, a free demonstration version of Zemax optics studio was used to model the system and measure the signal throughput. Figure 3.22 shows the non-sequential Zemax optical model of the 775 nm prism design.

All of the lenses used were implemented from the libraries based upon the manufacturers part numbers. As the prisms were not available in the libraries, they were manually designed based upon their dimensions and material type. Thorlabs AC254 075 B achromatic doublets are used as L1 and L2

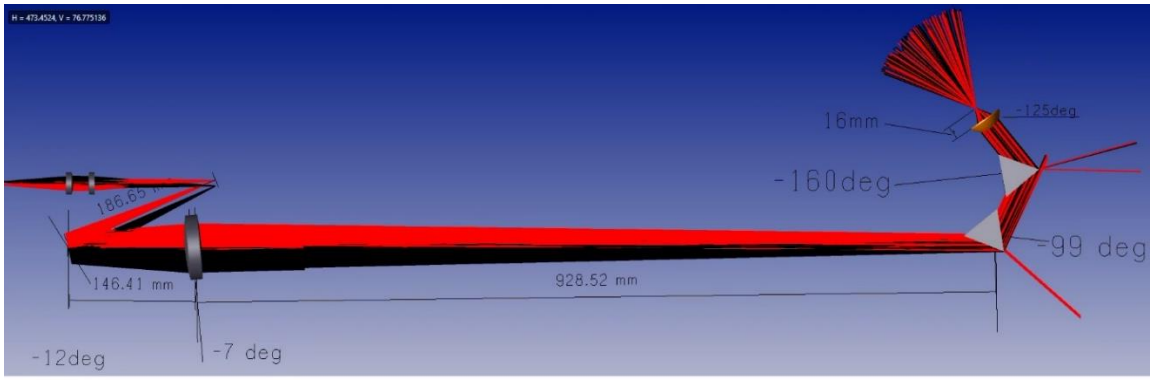

Figure 3.22. Zemax model of optical design for recombining the spectral features through the use of prisms. A specific wavelength corresponds to each spatial position of the image projected onto the DMD (determined by the optics and the spectrometer. The divergence of the reflected beam therefore has a wavelength relationship, by matching this to the dispersion of the prisms is it possible to create a polychromatic, collimated beam that can be efficiently focused to the 50 µm required by the detector area.

The prism-based design in Figure 3.22 using the PDM50CT SPAD was built and tested. The first, time gated Raman maps were generated using phantom samples of paracetamol and stilbene in the presence of a highly fluorescing dye and the results are shown in the publication ("Fast Raman spectral mapping of highly fluorescing samples by time-gated spectral multiplexed detection"), Chapter 4.

Recombination of spectra using a grating.

The throughput of the design is limited by restrictions in the physical size of available prisms (50 mm N-SF11 from Edmund Optics) and reflections at the surfaces of the prism due to high angle of incidence, although these limitations however could be overcome with custom prisms and coatings.

In the same manner as described above, the divergence angle of the collimated spectra can be matched to the dispersion of a diffraction grating. Using a blazed, reflective diffraction grating, the lower angle of incidence leads to more light collection surface area and efficiency would be improved.

One option would be to use the DMD to reflect the spectrum back into the spectrometer along an optical path parallel to the original (z axis) but offset the beam slightly in the x-y plane so that the recombined spectrum is focused to a point at the entry point of the spectrometer, adjacent to the input beam. This method was successfully applied to a Hadamard-transform spectrometer in 1971 by J.A.Decker Jr [70] (see Figure 3.23). Although this would provide the most physically compact method, there are technical and alignment difficulties when using a DMD in this manner. As the DMD mirror states are +/-12 degrees, reflection back down the incident optical axis would require additional optics to collect, reflect and refocus the signal onto the same region of the DMD before being focused back into the spectrometer. Although it is possible, it would be extremely difficult to align to the point of being unpractical.

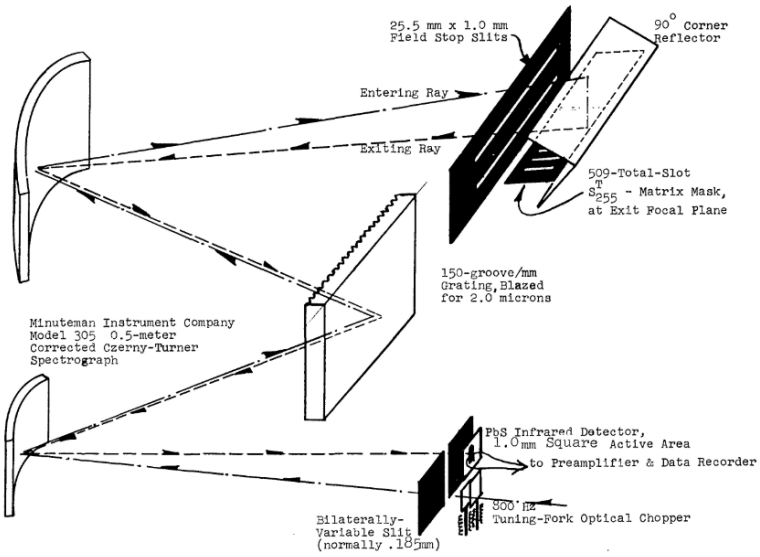

Fig. 2. Optical schematic of 255-slot HTS.

March 1971 / Vol. 10, No. 3 / APPLIED OPTICS 511

Figure 3.23. Schematic of Hadamard spectrometer by J.A.Decker .Jr [70] demonstrating successful recombination of spectra

The better solution, although more costly and a less efficient use of space would be to use a second spectrometer mounted at the exit port to recombine the spectrum. By using the same optics to both recombine and disperse the spectrum, by way of symmetry, no calculations are required. This method was implemented and found to make the alignment process significantly more straightforward. Figure 3.24 shows the configuration used for the final design.

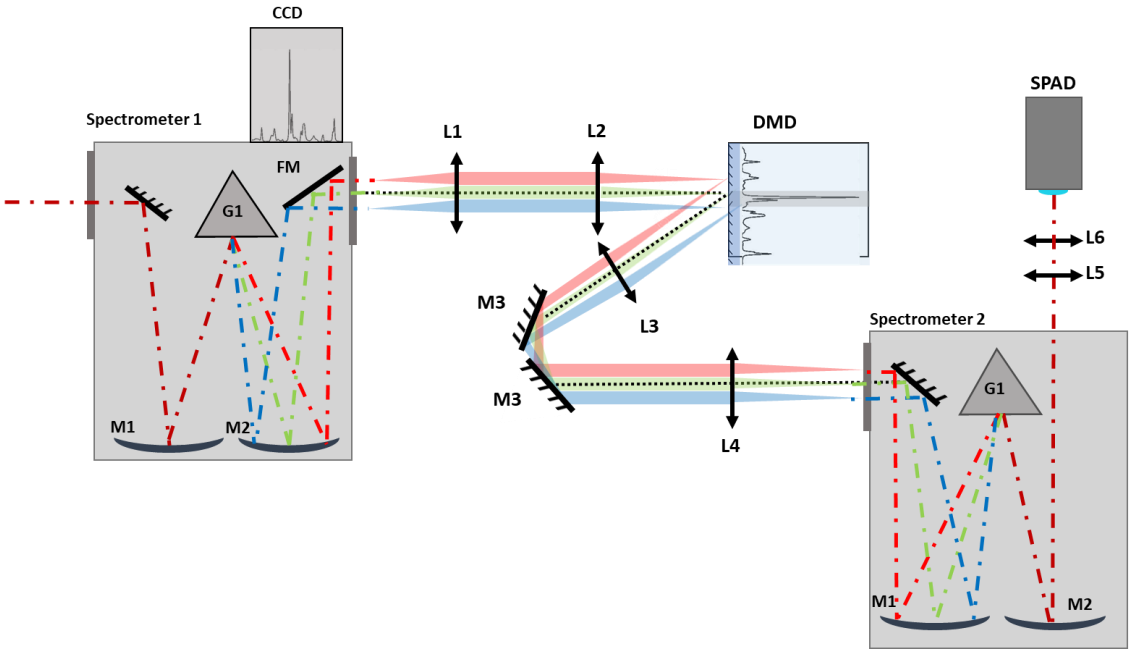

Figure 3.24. Schematic of final design using two spectrometers. Spectrometer 1 disperses the spectrum onto the CCD or to the side port via the flipper mirror (FM). L1 & L2 (AC254-75-B) relay the spectrum onto the DMD for optical filtering. L3 & L4 (AC254-75-B) relay the DMD focal plane into spectrometer 2 for recombination. L5 & L6 (AC127-040-B & AC 127-020-B) provide additional magnification (2X) and focus the recombined spectrum onto the single pixel detector.

Alignment is aided by mounting the CCD at the exit port of spectrometer 2 and adjusting for a single peak that is the combination of all the wavelengths incident at the entrance port. The throughput, size of the spot and therefore the effectiveness of the recombination can be assessed. By adjusting the angle of the grating for the zeroth order, the full wavelength range is imaged at the CCD image plane, albeit inefficiently due the low zero order efficiency of the diffraction grating.

3.5 Detection electronics

3.5.1 Time to digital convertor

The digital outputs from the SPAD and the laser controller are TTL level signals designed to be driven into 50 Ohm loads. There are a several, off the shelf options available to compare the time difference of two digital signals to a high degree of precision.

High performance time correlated single photon counting devices such as the BH SPC-130 series have been specifically developed for time correlated single photon counting (TCSPC) for fluorescence lifetime measurements and offer picosecond resolution (6.6 ps FWHM SPC 130). Although they offer superior performance, their price prohibits their implementation, furthermore they require a PC with PCI slot to operate.

Low-cost time to digital convertors have, in recent years become available due to demand for LIDAR systems. The AMS TDC-GPX2 4-channel Time-To-Digital Convertor is a low cost, high-performance device with an accuracy of 10 ps and a data throughput rate of up to 70MSPS. Using a design based upon a ring oscillator, the reference clock START input propagates though a series of invertors and increments a coarse counter before returning back to the beginning. When a STOP signal is received, the state of each invertor and the counter is latched. The course counter and the number of latched invertors allows for high precision discrimination of the START- STOP signals. The 3.3V CMOS design requires approximately 0-3.3V input range on the reference and Stop inputs, therefore, the 5V TTL output from the SPAD requires a suitable attenuator. The required voltage amplitude attenuation in dB is calculated from Eq 3.1

$$dB = 20log_{10}(V_0/V) \qquad [3.1]$$

An 8.3dB attenuation is required to bring the voltage from 5V to 3.3V peak to peak.

GPX eval board

The initial prototype was developed using the convenient evaluation board GPX2-EVA-KIT (Figure 3.24) which consists of QFN64 packaged TDC-GPX2 (2) device mounted to an optimized PCB with power supply (4) and filtering. The built in FPGA (1) allows initial set up and data acquisition from the TDC via USB connection to a PC. Configuring and reading the results from the TDC-GPX2 via a microcontroller is also fully supported through LVDS (low voltage differential signal) or SPI (serial peripheral interface).

3.5.2 Microcontroller

Key parameters considered when selecting a suitable microcontroller are:

- Processor speed
- SPI capable
- Digital inputs/outputs
- Voltage levels
- Programming language of platform
- USB interface

The Arduino Due is a high-speed microcontroller based upon a 32-bit Atmel SAM3X8E-M3 CPU running at 84MHz operating at 3.3V CMOS levels. SPI capable with a native USB port connected directly to the microcontroller pins allows for high-speed USB control of the GPX2 TDC. The Arduino integrated development environment (IDE) is based on C++ with built in libraries for SPI communication.

Connecting the SPI interface was a straightforward operation thanks to the headers on the PCB of the TDC (Figure 3.2.1 (3)). Although it should be noted that the FPGA (1) SPI connections need to be isolated by removing the series resistors or cutting the PCB tracks on the bottom layer of the board. Table 3.1.1 shows the relevant connections required to interface the GPX TDC to the microcontroller.

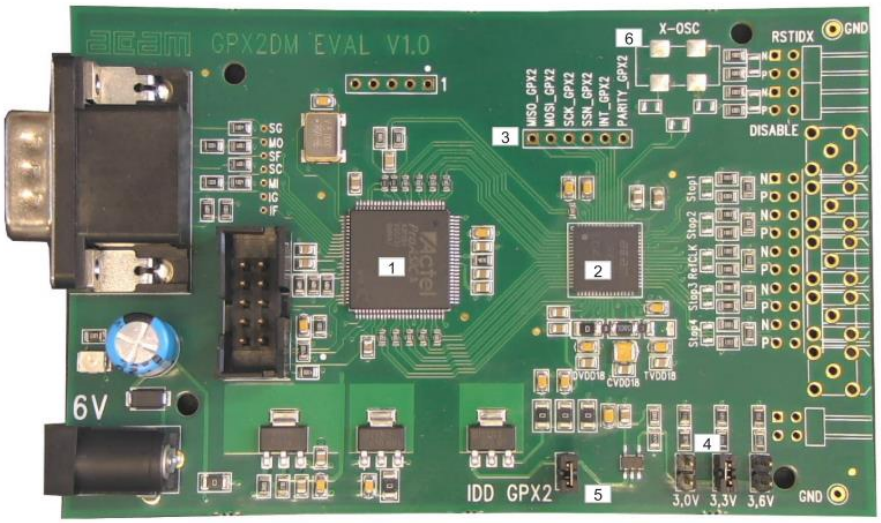

Figure 3.24 Time to digital convertor evaluation module. 2)GPX2 TDC. 1) FPGA used to read/write data to the TDC and communicate via USB interface. 3) SPI headers for connection to microcontroller.

Table 3.1.1 Required connections between microcontroller and GPX2 time to digital convertor

GPX 2 TDC pin	Microcontroller pin	Description
MISO	MISO	SPI master in slave out
MOSI	MOSI	SPI master out slave in
SCK	SCK	SPI serial clock
SSN	Digital output	SPI slave select
Interrupt	Digital input	High when data is available in fifo buffer

3.6 Software

The data sheet for the GPX time to digital convertor is comprehensive and comes with example C++ code for initial control. The configuration settings for the GPX TDC are saved to the microcontrollers flash memory and transferred to the TDC via SPI when the devices are powered up.

The software for the microcontroller is written in the Arduino IDE development environment (C++) while the main instrument control program is written in MATLAB.

Sending and receiving commands and data between MATLAB and the microcontroller simply involves setting us a serial COMM port in both programs and setting up both devices to monitor the port for data. The flow chart in Figure 3.1.2 shows the steps required to configure and control the GPX TDC from MATALB via the microcontroller.

The main control program written in MATLAB is responsible for configuration and real-time control of the laser, microscope stage, DMD and microcontroller.

For real time digital light processing the DMD receives a continuous stream of video data from the main control program via HDMI. As the DMD is a binary device, a black and white image is interpreted and output as an array of mirrors tilted at +/- 12 degrees to the normal. One of the reflected axes goes to a beam stop as it is not required and the other is focused on to the detector.

For an unknown sample it is required to scan the spectrum in a sequential mode to build up the intensity as a function of wavelength. In this mode (referred to hereafter as “DMD scanning mode”) the program produces an image of a binary black and white rectangle of a width (W) (Figure 3.25a). The width of the rectangle displayed by the DMD is analogous to the entrance slit on a spectrometer hence the value is determined experimentally to provide the best compromise of signal and resolution.

Data is acquired and the rectangle is sequentially shifted to build up a complete spectrum. Photon count data is streamed to Matlab in real time where it is stored and analysed. When the spectral features of interest have been determined the instrument can be operated in multiplexing mode (Figure 3.25b) to speed up acquisition.

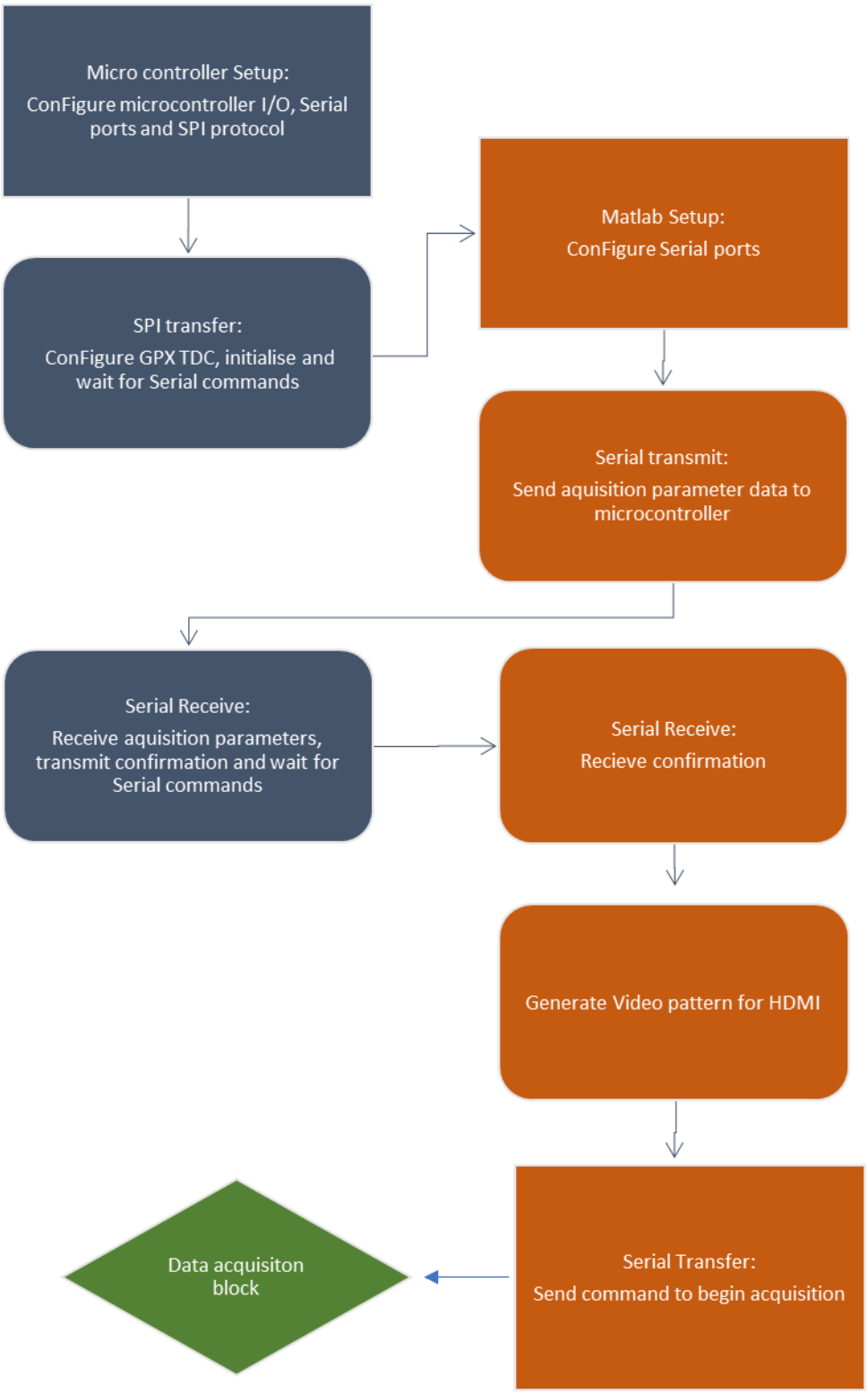

Figure 3.25. Flow chart of code blocks involved in setting up the TDC and acquiring data. Blue blocks represent microcontroller code (C++)_orange blocks represent Matlab code. The data acquisition block in green is explained in more detail below.

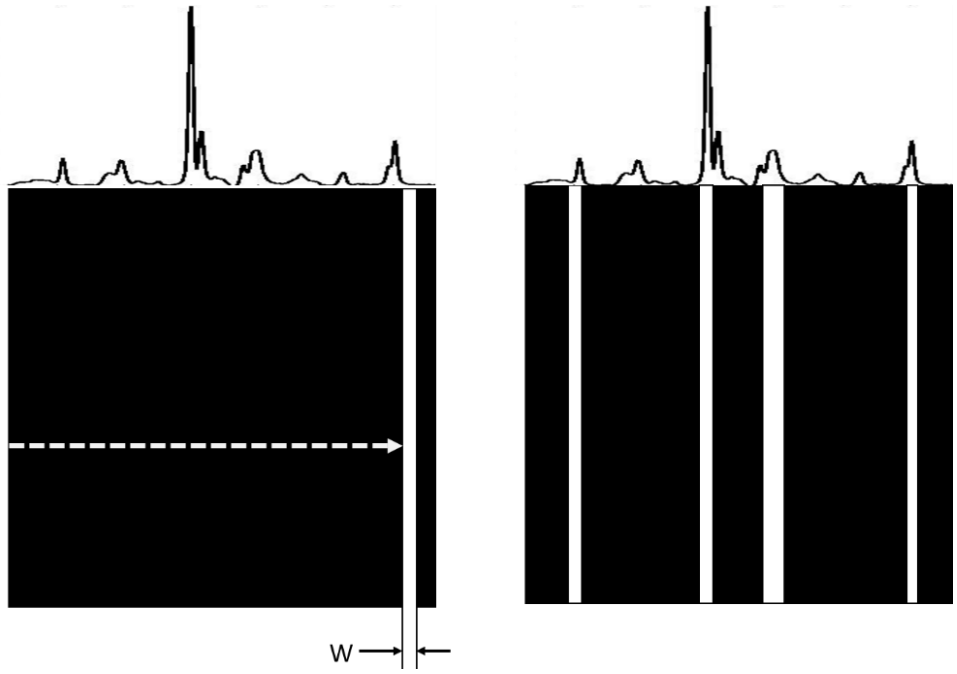

Figure 3.25. Example of the binary images projected to the DMD to generate the required optical filters. a) In DMD scanning mode a single rectangle of width W is sequentially scanned to build up a complete spectrum. b) In multiplexing mode, multiple spectral features are simultaneously directed to the detector to improve acquisition times.

Streaming the photon count data in real time, as each event is detected is effective however, it results in large data sets and is limited by the transfer and storage of the data to around 7000 counts per second.

Compression of the data at the lower levels managed by the microcontroller allows for a significant increase in the maximum data acquisition rate. Binning the data on the microcontroller during the acquisition period negates the need for a continuous data stream. Then at the end of each measurement period, a histogram can be quickly sent via serial.

By storing the values received from the TDC into a memory array with a bit depth of 3 bytes, length 2000 and bin width 5 ps we can significantly increase the data throughput while achieving an acceptable level of resolution and range. 10 ns range is more than adequate as most fluorophores we are interested in have lifetimes of < 1ns. As the maximum resolution of the time to digital convertor is 10 ps, the bin widths are set to 5 ps so as not negatively affect the resolution.

The Andor 401 DU CCD used for steady state CW Raman has a well depth of 16 bits and is found to be adequate for most applications, however, for highly fluorescing signals the detector does saturate, and data must be read multiple times (accumulation mode) during a single acquisition. The 3-byte (24 bit) bit depth of the histogram provides more than enough dynamic range and should avoid bin overflow for even the longest integration times of the most intense signals, 2^{24} =1.67x10^{7} photons per 5 ps bin.

Within the memory of the 32-bit microcontroller, integers can be saved as 32-bit (4 byte) values. The associated memory addresses consist of 4 x 1 adjacent bytes. The memory array associated with the histogram is therefore 2000 x 4 bytes. The memory is allocated in such a way one bin is 1 byte wide and 4 bytes deep. The time to digital convertor switches a logic output (int) low whenever detection event has been detected and stored in the buffer. The microcontroller detects this and begins the data acquisition as shown in the following steps and Figure 3.26.

Data acquisition block

1. Event recorded and stored in FIFO buffer of TDC.
2. Digital output (int) set to low.
3. Microcontroller selects SPI device SSN by sending a pulse.
4. Microcontroller sends Opcode read STOP 0x60 = 0b011XXXXX 1byte where XXXXX is the desired register address.
5. TDC sends the data from the addresses register on the MISO line.
6. Microcontroller converts to integer for maths operations.
7. Increment corresponding histogram address by +1
8. Send binary data from histogram memory address sequentially over serial at the end of each measurement cycle.

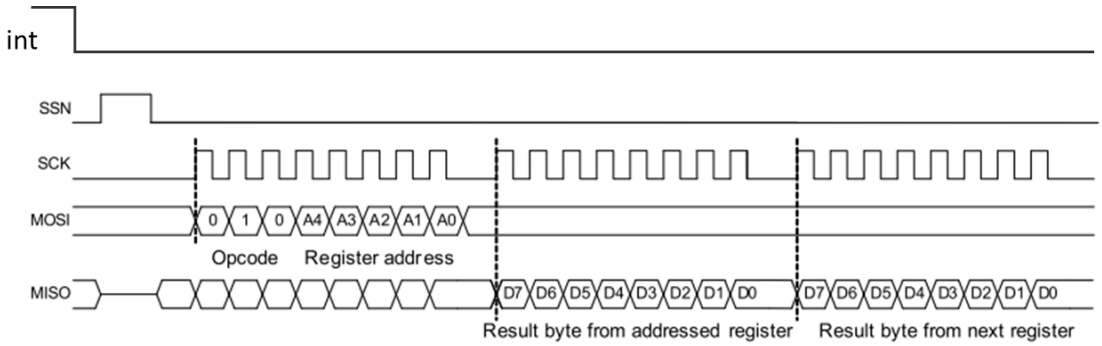

Figure 3.26 logic levels involved in the reading of SPI data from the time to digital convertor.

At the end of the acquisition cycle, the 6kb histogram is transferred by serial by sending the byte value of memory address associated with each bin. The data transfer takes ~2.5ms to add to the Serial buffer. Another 40ms is required to read and store the Serial data into Matlab structure .MAT file.

3.7 Experimental results for performance evaluation

The temporal resolution of the whole instrument is assessed by measuring the Raman intensity as a function of time I(t) for an optically clear, Raman scatterer with no fluorescence components. The resulting plot is known as the instrument response function (IRF) and is the true representation of the temporal resolution (Figure 3.27a & 3.27b). The measured FWHM of the instrument response function is 55-65 ps and 450 ps for the PDM 100CTE and the COUNT T series SPAD respectively – in close agreement with the value expected from the specifications of the detectors. The Raman spectrum of a clear polystyrene sample was measured using the PDM100CTE and the COUNT-T SPADs (Figures 3.27a & b), under identical conditions to compare the detection efficiency. As expected, the detection efficiency of the COUNT-T is approximately 6 times that of the PDM100CTE.

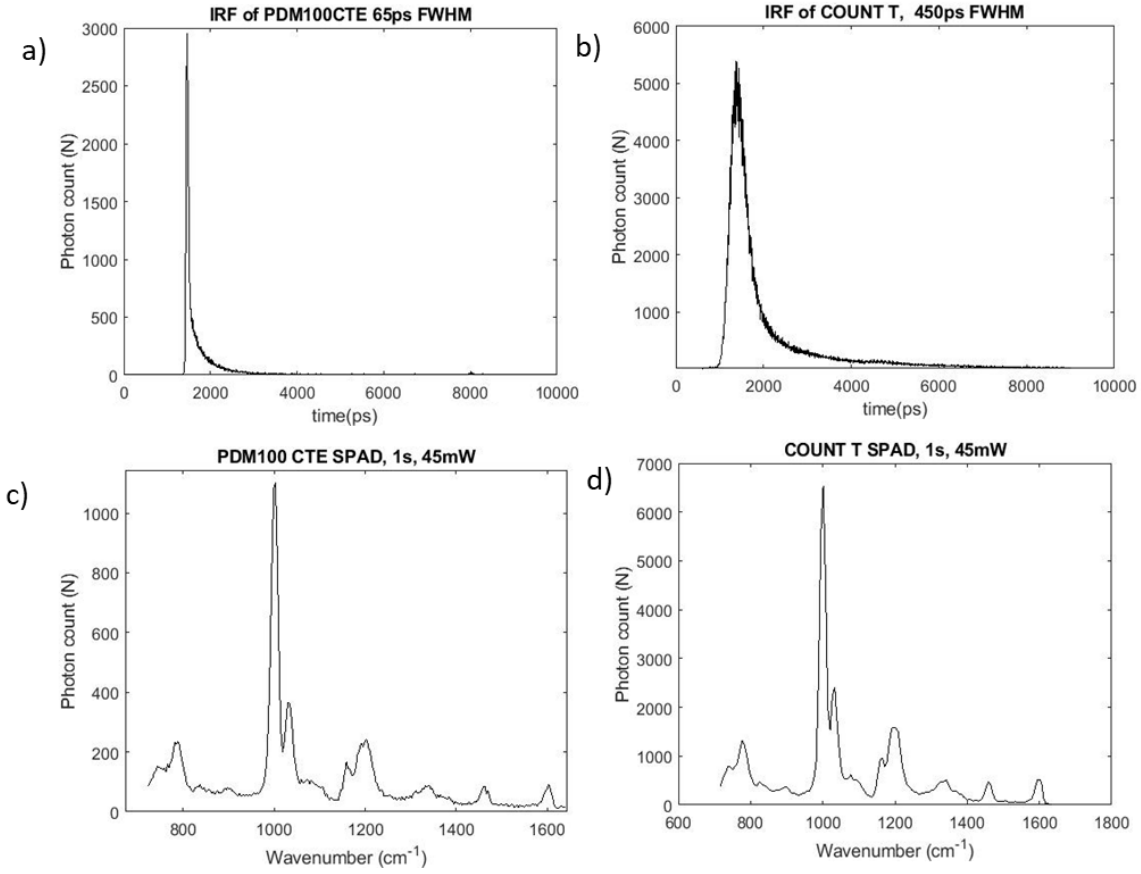

Figure 3.27 Comparison of the temporal response and detection efficiency of the PDM100CTE and the COUNT T SPADs from a standard clear polystyrene reference sample. a) IRF of the PDM100CTE. b) IRF of COUNT-T. c&d) Raman spectrum of polystyrene reference sample under identical conditions to compare the difference in detection efficiency.

Optical throughput

A throughput of approximately 5% is measured for the DMD, second spectrometer and associated optics. The throughput is evaluated by measuring the Raman spectrum of a reference sample using the same detector mounted at the exit of the 2nd spectrometer vs the exit of the 1st spectrometer.

Considering the transmission and reflectivity of all of the components used we have a theoretical maximum throughput of 41%. The DMD used is optimized for the visible spectrum so improvements to the throughput can be expected by using the NIR optimized version.

With reference to figure 3.24 the lenses L1 – L6 are B coated achromatic doublets from Thorlabs with transmission of 98.2% for the 800-900 nm range. There are 6 total mirrors between the exit of spectrometer 1 and the SPAD with an assumed reflectivity equal to a protected silver mirror at over 98 %. The diffraction grating used in both spectrometers is a Newport 220R 300 grooves per mm with 800 nm blaze at an average efficiency of 85 %. Finally, the DMD used was a DLP3000 optimized for visible excitation. The total reflectivity was not measured accurately but it is estimated to be approximately 60 % for 800 - 900 nm.

Spectral resolution

The spectral resolution is estimated as approximately 18 cm^{-1} by measuring the FWHM of the 1001 cm^{-1} peak of polystyrene using a 100 µm fiber input to spectrometer 1. Under the same conditions the CCD measures ~15 cm^{-1}

4 Publication

“Fast Raman spectral mapping of highly fluorescing samples by time-gated spectral multiplexed detection”

In our first publication, we demonstrate the use of time gated Raman spectroscopy for effective fluorescence rejection before going on to utilize DMD based multiplexing of spectral features to allow time gated Raman maps to be generated on the order of seconds per pixel. In this initial version, a prism-based design is used in conjunction with a 50 x 50um SPAD (PDM50C).

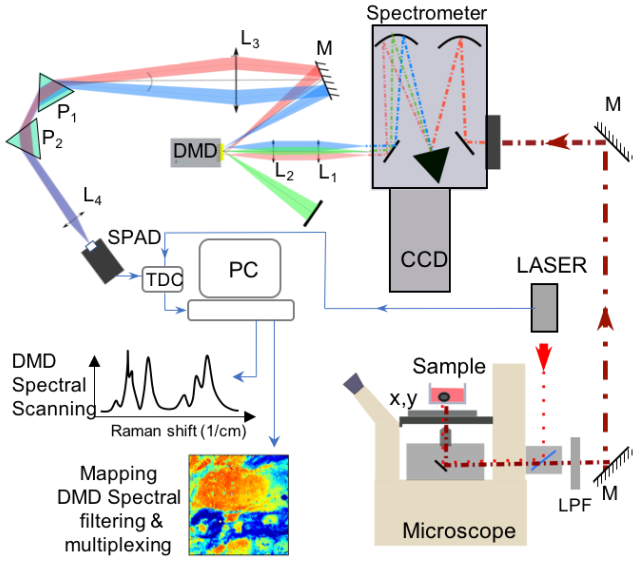

Fig. 4.11. Schematic description of the instrument (not to scale). DMD – digital micromirror device; SPAD – single photon avalanche photodiode, TDC – time-to-digital converter; L1, L2, L3, L4 – lenses; P1, P2 – prisms, M – mirror, LPF – 780 nm long pass filter; x, y – microscope translation stage.

While DMDs have been used in continuous-wave Raman spectroscopy, both for spectral [71,72] and spatial filtering [73,74] (but not in time-gated mode), here we used two prisms to recombine the time-gated spectrally filtered Raman photons onto the single SPAD element in order to provide spectral multiplexing. While this configuration does not provide any advantage when acquiring full Raman spectra (scanning of DMD elements is still required), the high-resolution spectral filtering enabled by the DMD, combined with the spectral multiplexing, single SPAD element and high repetition laser enabled molecular mapping of highly fluorescing samples at high speed and chemical specificity.

Although it should be noted that with this method the spectral filter is optimized for only one compound at a time – requiring a separate acquisition for each target compound.

A schematic description of the instrument is presented in Fig. 1. A 35 ps pulsed, gain switched DFB laser diode with fiber amplification chain at 1550 nm, frequency doubled to 775 nm (OneFive Katana 08, 65 mW average power, 6.55 nJ pulse energy, 10MHz pulse rate) was focused on the samples via an optical microscope (Nikon) equipped with a 50X and 0.50 NA objective (Leica) and a translation stage (PI 542). The Raman scattered photons, together with the elastically scattered and fluorescence photons were collected by the same objective and collimated towards a spectrometer (Andor Shamrock 303i) equipped with a 300 lines/mm grating. The long pass filter blocked the elastically scattered light. The spectrometer was equipped with a deep-depletion back-illuminated CCD (DU401 Andor). By switching a mirror, it was possible to direct the dispersed Raman and fluorescence light via a side port onto a digital micromirror device (Texas Instruments DLP3000 digital micromirror device). Lenses L1 and L2 relay the image plane from the spectrometer output port onto the DMD. As each spatial element of the DMD corresponds to a specific wavelength, the DMD can be used for high-resolution spectral filtering. The light corresponding to the selected wavelengths is recombined via two equilateral prisms then focused by lens L4 onto a $50\ \mu m \times 50\ \mu m$ area SPAD (MPD 50CT SPAD). The prisms were selected to obtain the desired amount of dispersion and lens L3 was selected to match the dispersion angles from the spectrometer to the dispersion of the prisms, such that the entire selected wavelength range was successfully recombined to form a collimated polychromatic beam. The arrival of each pulse from the SPAD was compared with the Katana laser sync pulse via a time to digital convertor (TDC) with 10 ps temporal resolution (TDC GPX2 by AMS). A microcontroller handled the configuration of the TDC and the data acquisition via SPI communication, which then sent the photon detection data in binary serial format to a personal computer (PC). The instrument time-response was approximately 190 ps, which is currently limited by the SPAD used.

The performance of the instrument was first tested by comparing the spectra of standard non-fluorescing materials used in Raman spectroscopy (e.g. polystyrene) acquired using the conventional Raman set up based on the CCD with the spectra of

the same samples acquired by scanning the DMD elements sequentially (referred to as "DMD scanning"). The spectra were acquired in the 650-1650 cm^{-1} range with a resolution of 10 cm^{-1}, equivalent to the spectrum obtained using the Andor DU401 CCD. Only minor differences were observed related to the relative intensity of the bands that were attributed to differences in the wavelength-dependence of the optical components and detection efficiency of the SPAD and CCD. Figure 4.22 shows that all main bands in the continuous-wave Raman spectrum of polystyrene (PS) acquired with the CCD are identified in the time-gated spectrum measured in the DMD scanning mode.

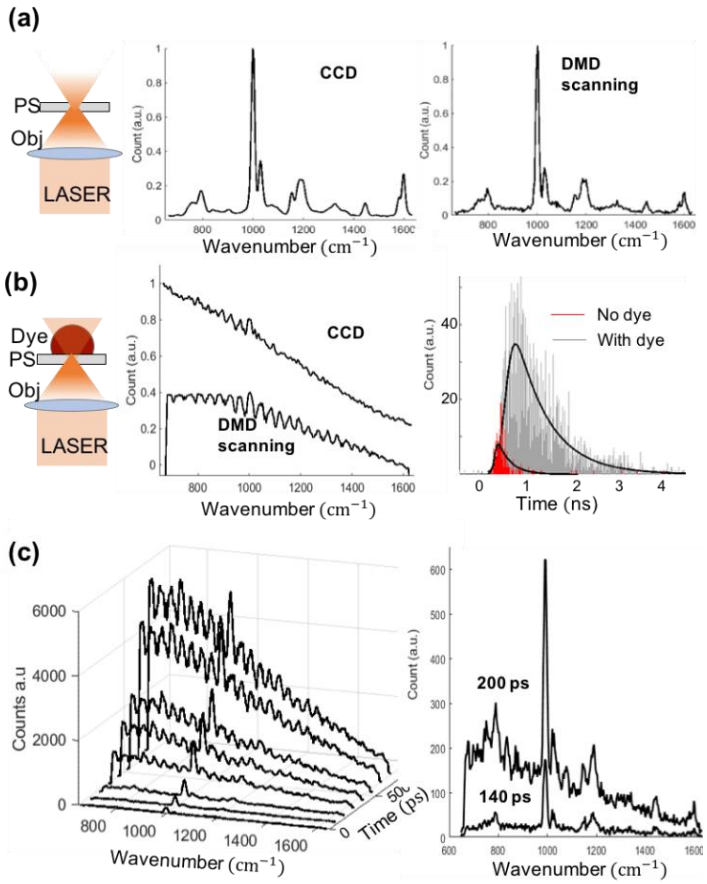

Fig. 4.2. (a) Comparison between the Raman spectra of a polystyrene (PS) sample acquired with the CCD and with the new set up in the DMD scanning mode without time-gating (all time-components integrated 200s total integration time). (b) as (a), but after a drop of a fluorescent dye (Fluorescent Red 730 (Sigma)) with lifetime ~1 ns was added on the PS. The time distribution of the detected photons before (red) and after adding the fluorescent dye (grey) is presented on the right. (c) Time-gated Raman spectra of the PS/Dye sample acquired in the DMD scanning mode.

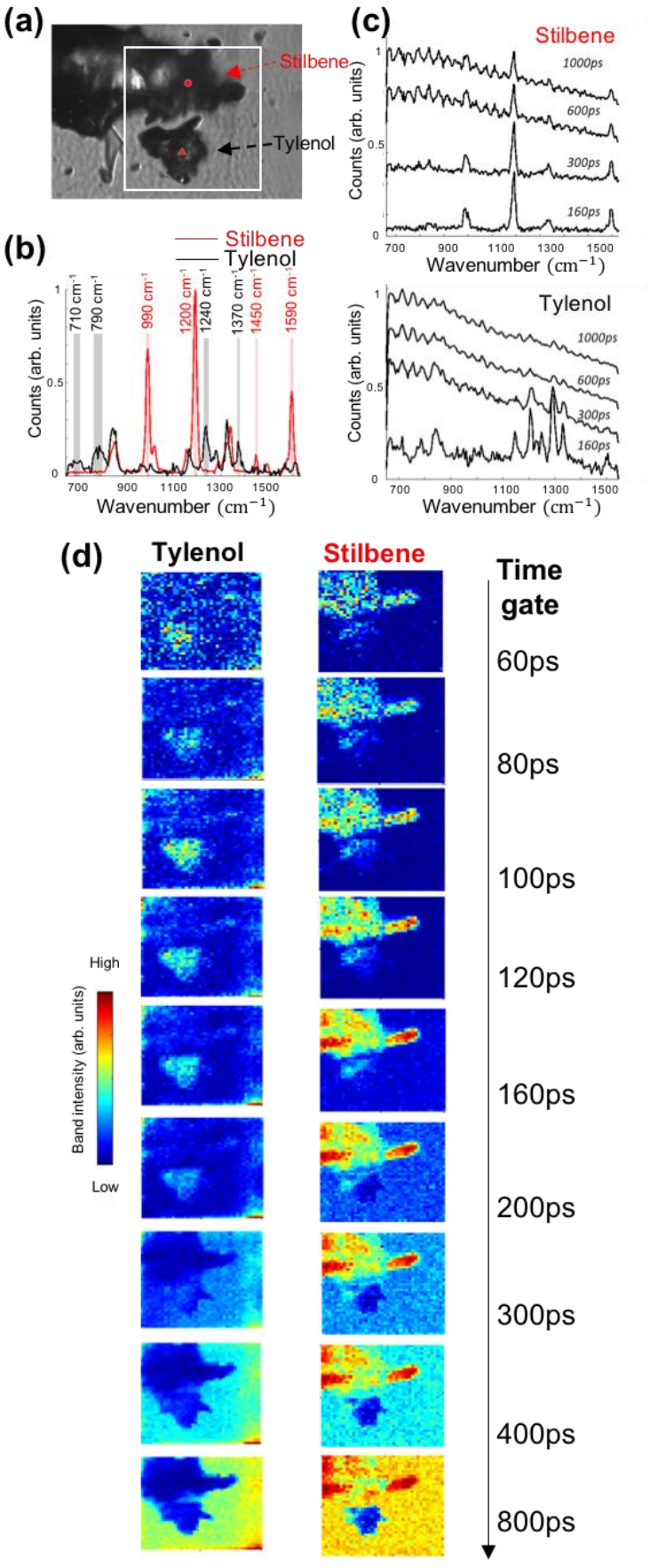
(a)
Stilbene
Tylenol
(b)
Stilbene
Tylenol
Counts (arb. units)
710 cm-1
790 cm-1
990 cm-1
1200 cm-1
1240 cm-1
1370 cm-1
1450 cm-1
1590 cm-1
Wavenumber (cm−1)
(c)
Stilbene
1000ps
600ps
300ps
160ps
Counts (arb. units)
Wavenumber (cm−1)
Tylenol
1000ps
600ps
300ps
160ps
Counts (arb. units)
Wavenumber (cm−1)
(d)
Tylenol
Stilbene
Time gate
60ps
80ps
100ps
120ps
160ps
200ps
300ps
400ps
800ps
High
Band intensity (arb. units)
Low

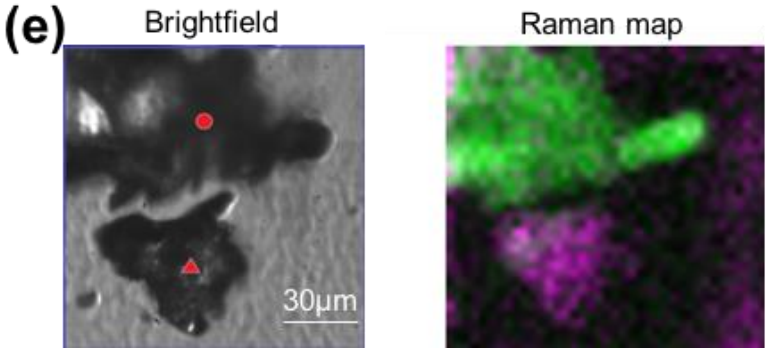

Fig. 4.3. (a) Brightfield image of the Tylenol and stilbene powder on a glass coverslip (mapping area 120 µm × 120 µm). (b). Time-gated spectra of stilbene (circle) and tylenol (triangle). The bands used for multiplexing are highlighted. (c). Time-gated Raman spectra at the same locations after the addition of the fluorescing dye on top of the sample. (d) Time-gated Raman maps acquired in the DMD multiplexing mode corresponding to the Tylenol (left) and stilbene (right) bands. Acquisition times: 3 minutes for stilbene maps, 27 minutes for the Tylenol maps. (e) combined pseudo-colour Raman map: Tylenol (purple) and stilbene (green); time-gate was 120 ps for Tylenol, and 160 ps for stilbene, total time: 30 minutes.

To evaluate the ability of the instrument to discriminate between Raman and fluorescence photons (i.e. fluorescence rejection), the experiments were repeated after adding a highly fluorescing dye (Sigma Aldrich Fluorescent Red 730 (lifetime ~1ns)) solution on top of the polystyrene sample. Figure 4.2b shows that the Raman bands of polystyrene are swamped by the broad fluorescence background, both for the spectrum acquired with the CCD and the spectrum acquired in the DMD scanning mode without time-gating. The main band of the PS at 1004 cm^{-1} corresponding to the ring breathing mode can hardly be distinguished. With this large background, baseline subtraction techniques cannot recover the Raman bands, which remain buried in the shot-noise and etaloning fringes from the detection system accentuated by the strong fluorescence background. Nevertheless, the histograms of the timing of photon detection events (Figure 4.2b) show that the Raman bands could be recovered effectively by time-gating the detection. The time-gated Raman spectra of the PS/dye sample are presented in Figure 4.2c and show that for time gates shorter than 200 ps, the Raman bands of the PS can be observed clearly (the bands in the spectra acquired at 140 ps are similar to those in Figure 4.2a).

While the results in Figure 4.2 demonstrate efficient rejection of the fluorescence photons, the new detection scheme in DMD scanning mode, however, presents no specific advantages compared to previously reported time-gated Raman spectroscopy

using single SPAD elements and scanning monochromators. The advantage of the DMD scheme becomes evident when operating the instrument in "DMD spectral multiplexing" mode, which allows simultaneous detection of the Raman photons corresponding to selected Raman bands of interest, with high-spectral resolution filtering (10 cm^{-1} for this instrument) and high efficiency rejection of the fluorescence photons. The acquisition of a higher number of Raman photons, at a high repetition rate offered by the laser (10 MHz), leads to significantly shorter integration times, and makes time-gated Raman spectral mapping practical.

To demonstrate these advantages, we selected a sample consisting of trans-stilbene and Tylenol powder on a glass coverslip, covered by a small amount of fluorescent dye solution (Figure 4.3a). Stilbene and Tylenol are common samples used in Raman spectroscopy because they elicit sharp Raman bands and no fluorescence background using NIR (775 nm) excitation. The time-gated Raman spectra of Tylenol and stilbene measured in the DMD scanning mode (before adding the fluorescent dye) were used to identify the Raman bands that provided the highest spectral discrimination between the two materials (Figure 4.3b). The spectral features were then carefully chosen to maximize the Raman signal whilst minimizing the spectral overlap. In the example presented here, the bands unique to Tylenol were selected at 710, 790, 1240 and 1370 cm^{-1} (highlighted in grey in Figure 4.3b), while the bands unique to stilbene were the 990, 1200, 1450 and 1590 cm^{-1} (highlighted in pink in Figure 4.3b). After adding the fluorescent dye, time-gated Raman spectra were collected at the same locations (Figure 4.3c). The results show that the Tylenol bands can be efficiently recovered for time-gates as long as 160 ps, but they become covered by the increasing fluorescence background at time-gates longer than 300 ps. Similar increase in the fluorescence background at longer time-gates is observed for stilbene; however, stilbene molecules have higher Raman cross-section, and some bands can be identified even at time-gates as long as 1000 ps.

After identification of the specific bands for Tylenol and stilbene, time-gated Raman maps were acquired by raster scanning the sample through the laser focus over an area of 120 μm x120 μm (3 μm step size, corresponding to 40 x 40 pixels) (Figure 4.3d). To obtain the time-gated Raman maps of Tylenol, the DMD elements corresponding to the 710, 790, 1240 and 1370 cm^{-1} were selected to reflect the Raman photons towards the SPAD, while all other DMD elements were switched to reflect the light

corresponding to all other wavelengths towards the beam block. For the Raman maps highlighting the areas of stilbene, only the DMD elements corresponding to the 990, 1200, 1450 and 1590 cm^{-1} were turned towards the SPAD. This spectral multiplexing allowed the acquisition of the time-gated Raman signals with integration times of 1s per pixel for Tylenol and 0.1s per pixel for stilbene. The total measurement times for the 40×40 pixel resolution images were 27 minutes for the Tylenol and 3 minutes for the stilbene (total scan time for both materials of approximately 30 minutes). To obtain the time-gated Raman maps, the raw data from the scans was separated into 20 ps bins and the resulting images are shown in Figures 4.3d (no further processing applied). (e) combined pseudo-color Raman map of the Tylenol and stilbene samples (time-gate was 120 ps for Tylenol, and 160 ps for stilbene, total time: 30 minutes).

The gate width that provides the greatest signal-to-noise ratio depends on the optical properties of the sample, the Raman intensity and the lifetime and intensity of the fluorescence. As such, the optimum gate width varies from sample to sample. As we are operating in time-correlated single photon counting mode, all photons are recorded with their respective time of detection tagged and the ideal time gate can be determined after measurement by inspection.

The time-gated Raman spectral maps show that the two materials, Tylenol, and stilbene, can be distinctly identified up to time-gates of 200 ps. Beyond this time, the stilbene signal increases but the Raman photons generated by Tylenol become buried in the fluorescence background. The Tylenol images show the greatest signal to noise ratio at a gate width of 120 ps, stilbene sample displays optimum contrast at 160 ps. For long time-gate values (e.g. 800 ps), the Raman photons are swamped by the fluorescence photons; the Tylenol and stilbene particles cannot be discriminated (they appear as regions of low signal as they block part of the fluorescence photons emitted by the dye molecules).

Conclusions

Here we present a simple and practical technique for time-gated Raman spectral mapping. To overcome the main limitations of current time-gated Raman spectroscopy techniques, we utilized a high-repetition pulsed near-infrared laser with a single element detector to enable high temporal resolution. Using a spectral filtering/multiplexing approach based upon a spectrometer as the wavelength

dispersive element, a DMD as the wavelength selective component and prisms to recombine the spectrum allowed the acquisition of the Raman photons with integration times as short as 0.1-1 s per pixel. Such short integration times enabled spectral mapping within practical time scales (e.g. 3-30 minutes) for samples for which the CW Raman bands were fully buried by the fluorescence background. While here we utilized a simple multiplexing technique for proof-of-principle, the DMD can be programmed for more complex multivariate spectral measurements to maximize chemical discrimination, as previously demonstrated for conventional continuous-wave Raman spectroscopy and imaging [54,59]. In addition, the ability to acquire photons with flexible selection of the time-gate allows to optimize the time-gate for each chemical component of the sample or enable simultaneous multimodal Raman and fluorescence lifetime imaging. While our proof-of-principle experiments were limited to standard materials commonly used in Raman spectroscopy, this is a platform technique that could be applied to a range of applications dealing with samples eliciting high fluorescence levels.

5 Publication

"Sub-surface molecular analysis and imaging in turbid media by time-gated Raman spectral multiplexing"

Abstract

Obtaining molecular information deeper within optically-turbid samples is valuable in many applications. However, in many cases this is challenging, in particular when the sample elicits strong laser-induced fluorescence emission. Here, we investigated the use of time-gated and micro-spatially-offset Raman spectroscopy (micro-SORS) based on spectral multiplexing detection to obtain subsurface molecular analysis and imaging for both fluorescing and non-fluorescing samples. The multiplexed spectral detection achieved with a digital micromirror device (DMD) allowed fast acquisition of the time-gated signals to enable 3D Raman mapping (raster scanning in the lateral *x*-*y* plane and using time-of-flight calibration for the axial *z*-direction). Sub-millimetre resolution molecular depth mapping was achieved with dwell times on the order of seconds per pixel. To suppress fluorescence backgrounds and enhance Raman bands, time-gated Raman spectroscopy was combined with micro-SORS to recover Raman signals of red pigments placed behind a layer of optically turbid material. Using a defocusing micro-SORS approach, both fluorescence and Raman signals from the surface layers were further suppressed, which enhanced the Raman signals from the deeper sublayers containing the pigment. These results demonstrate that time-gated Raman spectroscopy based on spectral multiplexed detection, and in combination with micro-SORS, is a powerful technique for subsurface molecular analysis and imaging, which may find practical applications in medical imaging, Cultural Heritage, forensics, and industry.

Through an optically transparent sample, light travels at a speed c/n, where c is the speed of light in vacuum and n is the refractive index of the samples (e.g. ~ 4.5 ps for 1 mm of water), which is shorter than the temporal resolution of current time-gated Raman spectroscopy instruments. However, light propagating through an optically turbid sample is diffusely scattered and has been shown to take 10-20 times longer to propagate [75], allowing for sub- millimetre resolution depth analysis using current technologies.

Due to various technical limitations, the detection efficiency of current time-gated Raman spectroscopy instruments is significantly less than for an optimized steady-state CCD based spectrometer. Furthermore, many time-gated Raman instruments operate with a fixed gate position. Therefore, to analyse the Raman intensity as a function of time, multiple measurements must be made while shifting the gate window with respect to the excitation laser pulse. As a consequence, subsurface 3-D Raman imaging by time-gated Raman spectroscopy has been impractical. By operating in time correlated single photon counting mode (TCSPC), all photons are collected, time tagged and stored to memory in a single measurement window, significantly improving acquisition time.

For an optically turbid material, subsurface photons undergo multiple scattering events. The diffused photons follow a random path and exit the material at a range of positions with respect to the excitation point. In a backscattering geometry, SORS exploits this effect in order to collect diffused Raman photons from subsurface regions. This is achieved by spatially introducing an offset between the laser illumination and Raman collection points. [76] Such offsets can be implemented by using optical fibres [77], DMDs [24], or using a CCD. [78] Micro-SORS (combining microscopy with SORS) has recently been shown to be effective in enhancing the Raman spectrum of the deeper, non-fluorescing target sublayer to be acquired. [79] However, micro-SORS cannot measure the Raman bands of a sample that elicits strong laser induced florescence because SORS cannot discriminate between fluorescence and Raman photons.

In this paper we use raster scanning time-gated Raman spectroscopy based on spectral multiplexed detection to obtain 3-D Raman information from optically turbid samples. In this approach, the spectral multiplexing works as a compressive sensing technique,

that has been used in continuous wave Raman spectroscopy to speed up imaging. [53,59,80,81] This technique has also been applied recently to time-gated Raman spectroscopy in order to decrease the acquisition times and enable time-gated Raman mapping of samples eliciting strong fluorescence backgrounds. [82] Using a single pixel detector, such as a single photon avalanche diode (SPAD), operating in TCSPC mode combined with multiplexing the Raman bands of interest, provides a speed advantage and higher signal to noise ratio. For optically turbid samples eliciting strong laser-induced fluorescence emission, time-gated Raman spectroscopy was combined with micro-SORS to achieve sub-surface Raman analysis with sufficient suppression of the fluorescence background. Micro-SORS allows suppression of the signal from the surface layer, while the time-gated detection provides the suppression of the fluorescence background of the deeper target layer. While time gating alone can suppress signal from the surface layer, we show there is a degree of temporal overlap between the different layers, resulting in the detection of unwanted surface generated photons at longer time gates. For fluorescing surfaces or samples in which the Raman bands of the different regions overlap this is undesirable and further attenuation is required. We present experimental results using layered, non-fluorescing polymer samples and use a range of fluorescing pigments/dyes and substrate materials to emphasise the potential use of the time gated micro-SORS technique for Cultural Heritage applications. In fact, fluorescence is one of the main obstacles often encountered in Cultural Heritage materials, as they exhibit a complex mixture of organic and inorganic compounds, frequently damaged and transformed due to the aging and decay mechanisms.

Materials and Methods

A 775 nm wavelength, 30 ps, 5 nJ pulsed laser with 10 MHz repetition rate (Katana, NKT photonics, Denmark) is used to excite the sample using a Nikon Eclipse inverted microscope via a 0.75 NA, 20x Nikon objective. The backscattered Raman photons are collected, and fibre coupled into an Andor Shamrock 303i spectrometer, where the spectrum can be either be focused onto an Andor DU401 CCD for general continuous wave (CW) Raman spectroscopy or focused upon a Texas Instruments digital micromirror device (DMD, Texas instruments DLPLCR4500EVM)) for wavelength

selection. The reflected spectrum from the DMD is then focused through the entry port of a second spectrometer (Shamrock 303i) to recombine the spectral features into a collimated polychromatic beam. This collimated beam can then be efficiently focused onto a 100 µm SPAD detector (MPD 100CTE (dark count rate < 30 counts per second)). The DMD is programmed to direct the light corresponding to the spectral features of interest to the SPAD, whose output is coupled to a high-performance time to digital convertor where it is then compared with the synchronization pulse from the laser. All photons detected are assigned a time tag before being streamed to a PC via a microcontroller. An instrument response function of 60 ps full width half max (FWHM) was determined by measuring the Raman signal from an optically clear, non-fluorescing sample. Custom software using MATLAB was used for serial communication, data acquisition and analysis. A slave microcontroller (Atmel SAM3X8E ARM Cortex-M3) is programmed to handle the SPI communication to the time to digital convertor and to send and receive data to MATLAB.

The instrument can be used in two main modes of operation, as described previously: [82] In the "DMD scanning mode", the Raman spectrum is reconstructed by sequentially scanning the micro-mirrors of the DMD. This mode is slow but allows the measurement of Raman spectra of unknown samples. Here the DMD was programmed to scan a rectangular array of mirrors analogous to a slit width of 100 µm in 150 steps to build up the full spectrum for 20s integration time. The total time to generate a full spectrum was therefore 3000s.

The "Spectral multiplexing mode" is used when the spectral features of the sample are known. In this case, the DMD can be programmed to use only selected micro-mirrors to direct multiple spectral bands to the SPAD (multiplexed detection). This mode increases the signal to noise ratio of the signal as more light reaches the SPAD and allows for shorter mapping times to be achieved than with a conventional single Raman band setup. For the multiplexed depth analysis shown here, Raman maps were generated with a total dwell time of 16s per pixel (7.1hrs for a 40x40 pixel map).

Micro-SORS measurements were carried out using the defocusing variant, consisting in the acquisition of a series of Raman spectra at imaged (focused) position and displacing away the

sample surface from the microscope objective as described previously. [83] The enlargement of the laser illumination and Raman collection areas allows achieving a higher relative content of the sublayer. Here, two defocused positions were applied, -200μm and -400μm, using a Nikon 20x 0.75 NA microscope objective. The laser spot diameter is 8 μm in focus, expanding to 210 μm at a defocusing of -400 μm.

Non-fluorescing samples: A set of calibration samples were prepared consisting of a 3 mm^3 polystyrene (PS) cube sublayer behind Teflon surface layers of varying thicknesses. This was achieved by stacking multiple layers of 75 μm thick polytetrafluoroethylene (PTFE/ Teflon) tape. Thicker layers of 1.5 mm and 3 mm layers of solid Teflon block (schematic in Figure 5.1a) were used as it was not practical to create such thick layers from multiple layers of thin sheets. Moreover, a sample consisting of two 3 mm^3 polystyrene blocks placed behind Teflon layers of 0.6 mm and 1.5 mm thickness was prepared (see schematic in Figure 5.4a) for 3-dimensional Raman mapping. For depth measurements, the microscope objective was replaced by a lens with 40 mm focal length (equivalent to a 5X magnification) leading to an increase in the laser spot diameter to 30 μm. This configuration increases the depth of field for laser excitation and leads to an enhanced signal from the sublayer compared to the signal obtained with microscope objective.

Fluorescing samples: A selection of dyes and pigments used in art has been carried out on the basis of their fluorescence emission:

- Red lake dye (0207, Natural Red 25, C.I. 75450), purchased from "Zecchi Colori Belle Arti Restauro", and compressed into a KBr pellet (1 mm thickness, 14 mm diameter). A lac dye stated to be extracted from the insect

coccus lacca as per suppliers's label, which infects fig trees indigenous to Asia and India. [84] Used throughout history as far back as 250 AD for dying of textiles, oil and water painting; Laccaic acid is the main chromophore.

- Carmine Naccarat pigment (42100, Natural Red 4, C.I. 75470), obtained from Kremer Pigmente, compressed into a KBr pellet (1 mm thickness, 14 mm diameter). An aluminium red lake of carminic acid, which is the principal chromophore. [85] It is extracted from cochineal, a scale insect. Cochineal dye was used by the Aztecs and Mayas of Central and North America. It became one of Mexico's most valuable export goods during colonial times. [86]

- Quinacridone Red Magenta (23720, PV19, C.I. 73900), supplied by Kremer Pigmente, is the typical quinacridone dye (compressed into a KBr pellet (1 mm thickness, 14 mm diameter)). It is a relatively modern synthetic organic pigment first synthesized and used commercially in the 1950s and used extensively in the paint industry, particularly in automotive paints. Quinacridone pigments were used by artists soon after their commercial introduction and are sold to artists under a variety of names such as Rose Red, Violet, Cobalt Violet, Quinacridone Crimson, Quinacridone Gold, Quinacridone Red, Rose Violet and more. [87]

- Fluorescein dye (F2456, C.I. 45350:1), purchased from Sigma Aldrich is a highly fluorescent molecule widely used in chemistry, laser and solar energy fields and for wood, acrylic and canvas prints. It is also used for the preparation of colorants as eosin. Layered samples using fluorescein as a sub-surface layer were prepared: 1 mm^3 of fluorescein powder, layered upon a 600 µm thick layer of Teflon (eight layers of PTFE tape); 1 mm^3 of fluorescein powder layered behind of a 100 µm thick layer of highly fluorescent brown paper. This sample was studied as a dry powder for convenience and proof of concept.

Results

Time-gated Raman raster scanning for 3-D molecular imaging of non-fluorescing samples

We investigated the ability of using time-gated Raman spectroscopy in spectral multiplexed detection mode to obtain 3-D Raman images of non-fluorescing optically turbid samples. This was achieved by raster scanning the sample in the lateral (*x*-*y*) directions using the microscope translation stage and using the photon diffusion time to obtain the depth information in the axial direction (*z* axis).

First, samples consisting of two layers were used to understand the level of temporal overlap between the Raman photons originating from different depths of the sample (i.e. surface layer and deeper layer). For this, samples consisting of a 3 mm^3 polystyrene (PS) cube covered by 1.5 mm and 3 mm thick sheets of Teflon were selected (schematic in Figure 5.1a). Time-gated Raman spectra of the sample consisting of the 1.5 mm thick Teflon surface layer were recorded in the DMD scanning mode and are presented in Figure 5.1b. The time-gated spectra were obtained by binning the data using 80 ps bin widths in 10 ps steps. Reference spectra of Teflon and polystyrene are also presented for reference, along with a range of different gate delays selected to illustrate the time evolution of the signal. For short time delays (40 ps) the sole contribution of the signal arises from the Teflon surface layer, as identified by the bands at 1216 cm^{-1}, 1299 cm^{-1} and 1379 cm^{-1}. As the signal from the Teflon surface layer peaks (at around 60 ps) Raman bands assigned to polystyrene can be detected at low intensity, such as the 1001 cm^{-1} ring breathing vibration. As time progresses, a decrease in the signal from the Teflon surface layer and an increase in the polystyrene signal from the sublayer is observed.

The experiments were repeated with a sample consisting of a 3 mm thick Teflon surface layer. To better understand the time evolution of the signals, the Raman bands for the Teflon and PS were integrated and the intensity plotted as a function of time (Figure 5.1c). The intensity versus time plots $I(t)$, in Figure 5.1c show a 100 ps time delay between the Teflon and polystyrene signal maxima when the 1.5 mm Teflon is used, which increases to 350 ps when the thickness of Teflon layer is increased to 3 mm.

A degree of temporal overlap is observed between the signals originating from different depths of the sample. For the 1.5 mm thick surface sample, the pure Raman spectrum from PS layer is obtained by subtraction of the Raman spectrum obtained at the shortest time-delay (e.g. 40 ps) from the Raman spectrum at a longer delay time (e.g. 1500 ps) (Figure 5.1d). The spectra were normalised and scaled accordingly to compensate for wavelength dependent scattering effects.

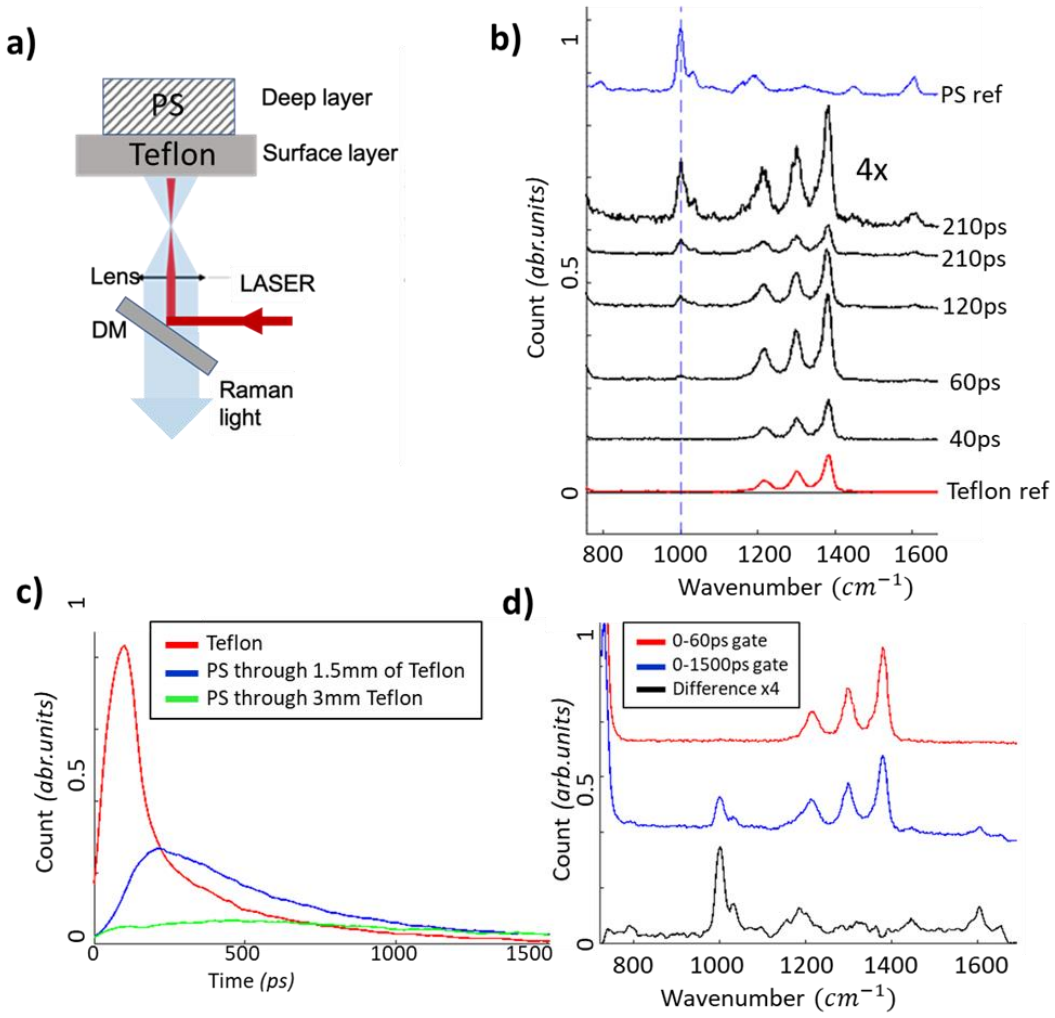

Figure 5.1. a) Schematic of a two-layered sample. b) Time gated Raman spectra polystyrene behind 1.5 mm of Teflon (red and blue reference spectra of Teflon and polystyrene). Spectra were offset vertically for clarity, but their intensity is not altered unless specified. c) Time histograms of signal from integration of the spectral features associated with polystyrene through 1.5 and 3 mm of Teflon sheet. d) 0-60 ps gate time, 0-1500 ps gate time and the difference (X4 for clarity).

After confirming the efficient detection of the Raman bands characteristic to Teflon and polystyrene (red and blue highlighted features in Figure 5.2a), the instrument was operated in spectral multiplexing mode in order to speed up the data acquisition. To provide a relationship between depth and diffusion time of the Raman photons, a set of calibration samples were prepared consisting of a polystyrene sublayer covered with Teflon surface layers of varying thicknesses. The Raman intensity of the polystyrene (through n layers of Teflon) as a function of time is presented in Figure 2b. Analysis of the measured data provides a relationship between the thickness of the surface Teflon layer (T(μm)) and photon diffusion time (t(ps)), where the total diffusion time is the sum of both the excitation and radiated photons; the net photon migration distance is therefore twice the thickness. The time which corresponds to the maximum intensity of the polystyrene signal is taken as the net diffusion time (Figure 5.2b) and was determined by the maximum value of a 2-term exponential fit to the data (with 95% confidence bounds) (example of fit (Figure 5.3)). The calculated values and associated errors are presented in Figure 5.2c.

A linear fit to the data presented in Figure 5.2c provides the relationship between the diffusion time and the thickness of the Teflon: $T(\mu\text{m}) = 8.53(\pm 1.5) * t(\text{ps}) \pm 180\ \mu\text{m}$. Previous works suggest a constant photon migration rate specific to each material hence the decision to use a linear fit. [75,88,89] However, the photon probability distribution will be weighted towards shorter distances as more scattering steps equates to a greater degree of attenuation; a more accurate model would therefore contain a decaying term to account for scattering losses. Furthermore, ideally, the calibration samples should be precisely machined from a single uniform block of material as there may be differences between the optical properties of bulk Teflon and stacked layers of PTFE tape. Although a more accurate calibration could be achieved, this level of accuracy was considered adequate here for the purpose of demonstrating proof-of-principle.

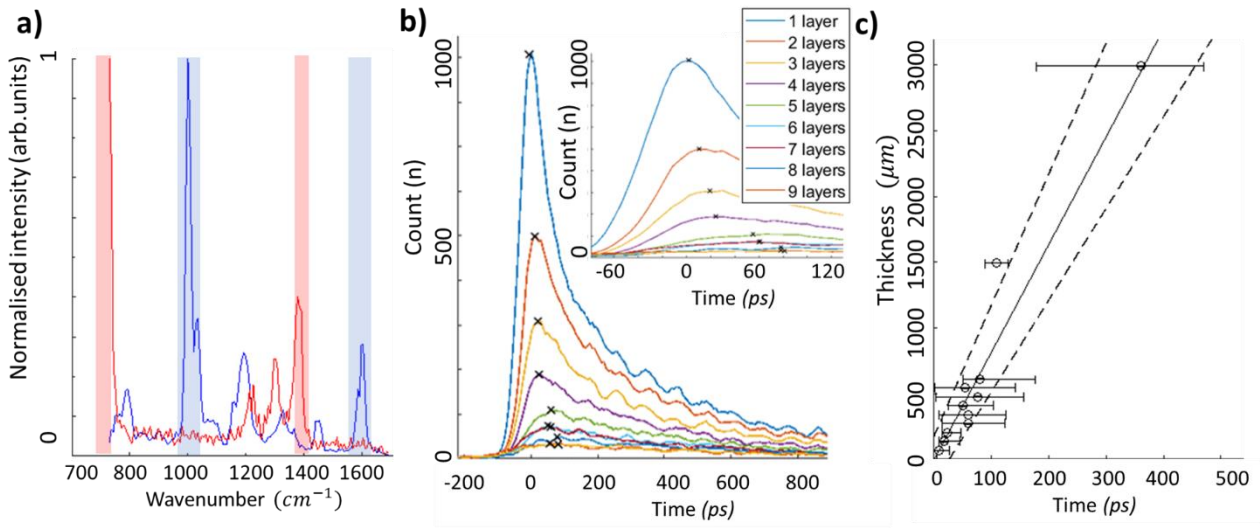

Figure 5.2. a) Reference spectra of Teflon and polystyrene with spectral features chosen for multiplexing highlighted in red and blue. b) Diffused Raman signals of polystyrene through n layers of PTFE tape plotted as a function of time $I(t)$, collected by multiplexing the polystyrene bands highlighted in Figure 5.2a (blue). c) Calibration of Teflon thickness vs diffusion time; each data point and error bar is determined by the peak of a two term exponential fit to the data in 5.2b (Figure 5.3)

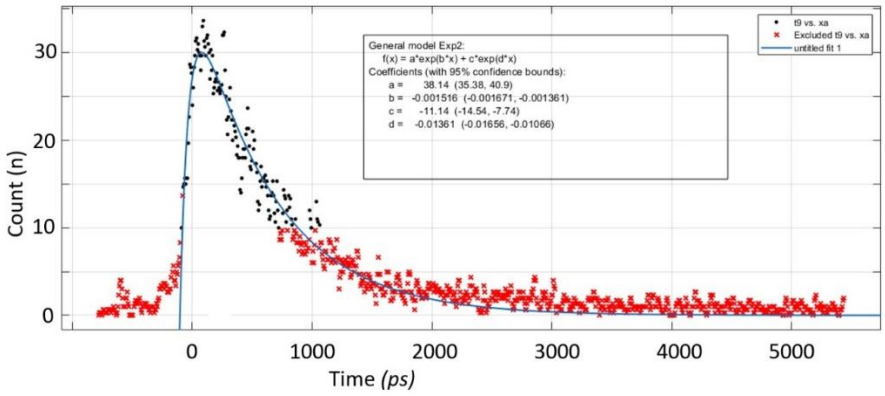

Figure 5.3. Example of method used to determine net diffusion time errors.

I(t) for polystyrene through 9 layers of Teflon tape with 2 term exponential fit to cropped data. The time which corresponds to the maximum intensity of the exponential fit data and confidence bounds is used to determine the net diffusion time and uncertainty.

The feasibility of time-gated Raman spectral multiplexing to measure 3-D Raman images of turbid samples was then investigated using a new sample consisting of two polystyrene blocks placed on Teflon layers of 0.6 mm and 1.5 mm thickness (see schematic in Figure 5.4a).

Previous works on depth profiling using time-gated Raman reported a *x-y* spatial resolution of ~1 mm for Teflon surface layers of 1 mm using defocused 400 nm excitation, [48] suggesting an adequate level of spatial resolution was possible. Here, raster scanning in the *x-y* plane using 250 μm steps size (40 x 40 pixels) two data sets were acquired for each pixel by alternatively switching the DMD mirrors to select the spectral bands of the two materials, Teflon and PS. The integration times for each material were 1s for Teflon and 15 s for PS respectively. Time-gated Raman maps of both the polystyrene (PS) and the Teflon are presented in Figure 5.4b for a selection of gate times selected to highlight the time evolution of the signal (data arranged into 80 ps bin widths). The results show that the Raman signal from the Teflon surface layer peaks around 140 ps. At this time point, the signal from polystyrene is detectable in the region corresponding to the thinner Teflon layer. The signal from the polystyrene on this region peaks at ~200 ps and finally, the signal from the polystyrene through the thicker layer peaks at ~250 ps. Applying the calibration formula determined above, the value of the Teflon thickness is estimated to depths of 511 ± 270 μm and 938 ± 360 μm for the two layers of Teflon (actual measured depths were 600 μm and 1500 μm). Using the photon time-of-flight at each pixel, we proceed in reconstructing a 3D map of the sample. For each pixel, the time at which the maximum intensity of both the polystyrene and Teflon signals $I(t)$ occurs is determined and maps produced based upon the mean photon time of arrival (Figure 5.4c for polystyrene map). The Teflon map determines the zero point (surface) and the two data sets are combined to create a 3D map of the binary sample (Figure 5.4d).

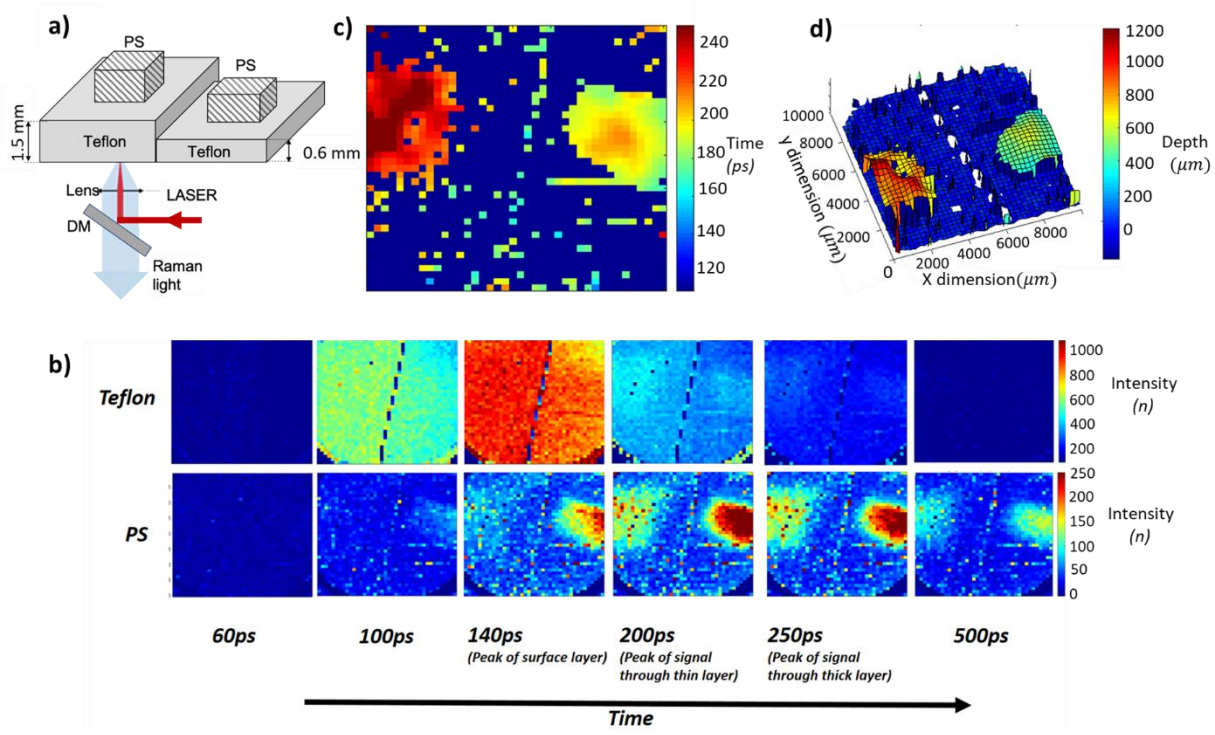

Figure 5.4. a) Schematic description of the Teflon/Polystyrene sample. b) 2D time gated Raman maps of both Teflon and polystyrene (PS) generated by multiplexing the bands shown in Figure 2a (red and blue). Gate times selected to show the time evolution of the signal. c) For each pixel, the time of maximum Raman intensity of polystyrene was used to create a Raman photon time of flight map. d) Depth surface plots of both Teflon and polystyrene generated by calculating the depth from the mean time of flight at each pixel. The data is overlaid to represent the spatial positions of the sample with the Teflon surface shown at zero depth (blue).

Time-gated Raman for fluorescence suppression of pigmented samples relevant to cultural heritage.

Here we investigated the feasibility of combining time-gated Raman spectral multiplexing with micro-SORS to obtain sub-surface molecular analysis from samples eliciting strong fluorescence backgrounds.

As the focus here has been on samples relevant to Cultural Heritage applications, we first investigated the ability of the time-gated Raman instrument to measure Raman spectra of several common red pigments. Red lake, Carmine Naccarat, Quinacridone Red Magenta and fluorescein were selected as they are particularly difficult to analyze using CW Raman techniques. For each sample, the DMD was programmed to select the full spectral range (750 cm^{-1} – 1650 cm^{-1}), the time profile $I(t)$ was then measured for all samples to determine the lifetimes of the fluorescence emission. Normalized $I(t)$ for all pigments are shown in Figure 5.5. All pigments had fluorescence lifetimes in the range 100-180 ps with the exception of fluorescein, for which the lifetime was calculated as 520 ps.

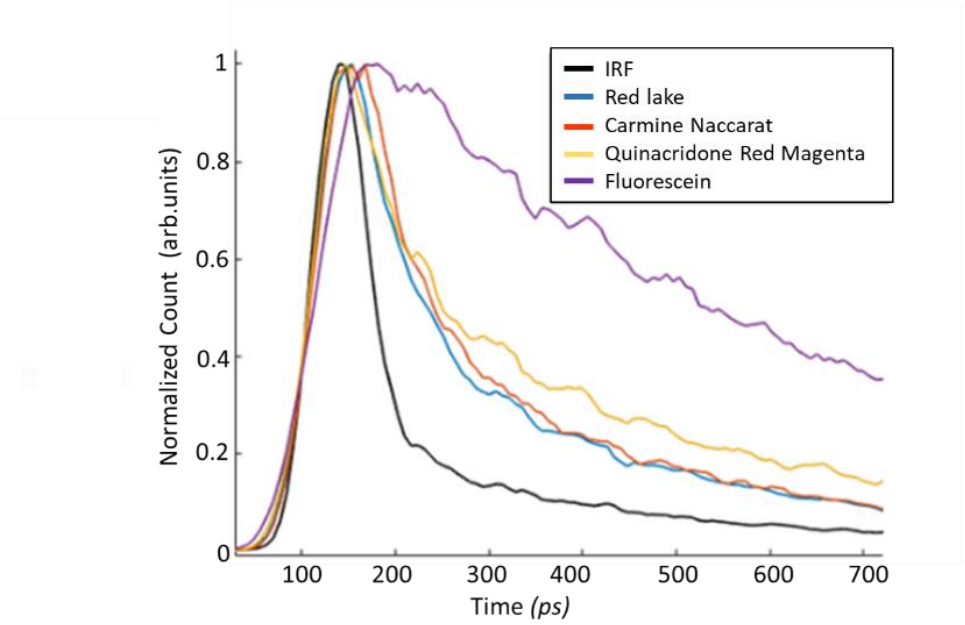

Figure 5.5 Normalized histograms of the laser-induced light emission for the four red pigments. The instrument response function (IRF) is included for comparison.

Time-gated Raman spectra using the DMD in scanning mode were recorded from all pigment samples to establish their main Raman bands and to estimate the level of fluorescence suppression that could be achieved with the current instrument. The data in Figure 5.6 is presented as progressively increasing gate widths to allow a comparison between time gating and a steady state CCD based system. Figure 5.6a presents the time-gated Raman spectra of Red lake showing that for long gate times (>550 ps, equivalent to continuous wave Raman spectroscopy) a Raman band at 1460 cm^{-1} is weakly observed through the intense fluorescence background. For short gate times (e.g. 80-150 ps), Raman bands at 1000 cm^{-1} ,1100 cm^{-1} ,1460 cm^{-1} and 1230 cm^{-1} can be observed, in agreement with Raman spectra reported previously, recorded with a FT Raman spectrometer based on 1064 nm laser excitation. [85]

The time-gated Raman spectra of Carmine Naccarat presented in Figure 5.6b. For continuous wave (long time gates of 550 ps) Raman bands at 1314 cm^{-1} and 1255 cm^{-1} are weakly observed. For short gate times (e.g. 80 ps), the reduced fluorescence background enhances the relative intensities of these features, allowing also detection of weaker Raman bands at 1110 cm^{-1} and 1430 cm-1. These features are in agreement with FT Raman by Burgio and Clark [90].

Figure 5.6c presents the Raman spectra of quinacridone Red Magenta. Figure 5.6c (550 ps) shows that for long gate times (CW), the Raman band at 1316 cm^{-1} is the only spectral feature observable. For short gate times (Figure 5.6c 80 ps), the 1316 cm^{-1} band is greatly enhanced and spectral features at 1508 cm^{-1},1570 cm^{-1},1592 cm^{-1} and 1645 cm^{-1} are observed, in agreement with FT Raman spectra recorded by Burgio and Clark. [90]

Time-gated Raman spectra of fluorescein are presented in Figure 5.6d. With a fluorescence lifetime of 520 ps, the time-gated detection provides the most efficient fluorescence rejection among all pigment samples. For long gate times (Figure 5.6d (550 ps)), the Raman bands at 1180 cm^{-1} and 1316 cm^{-1} are just observable though the intense fluorescent background. At shorter gate times (Figure 5.6d, 80 ps) the level of fluorescence suppression is very efficient and enables detection of Raman bands at 1170 cm^{-1} , 1318 cm^{-1} , 1396 cm^{-1} , 1484 cm^{-1} and 1571 cm^{-1} which are in good agreement with previous works by Wang et al. [91]

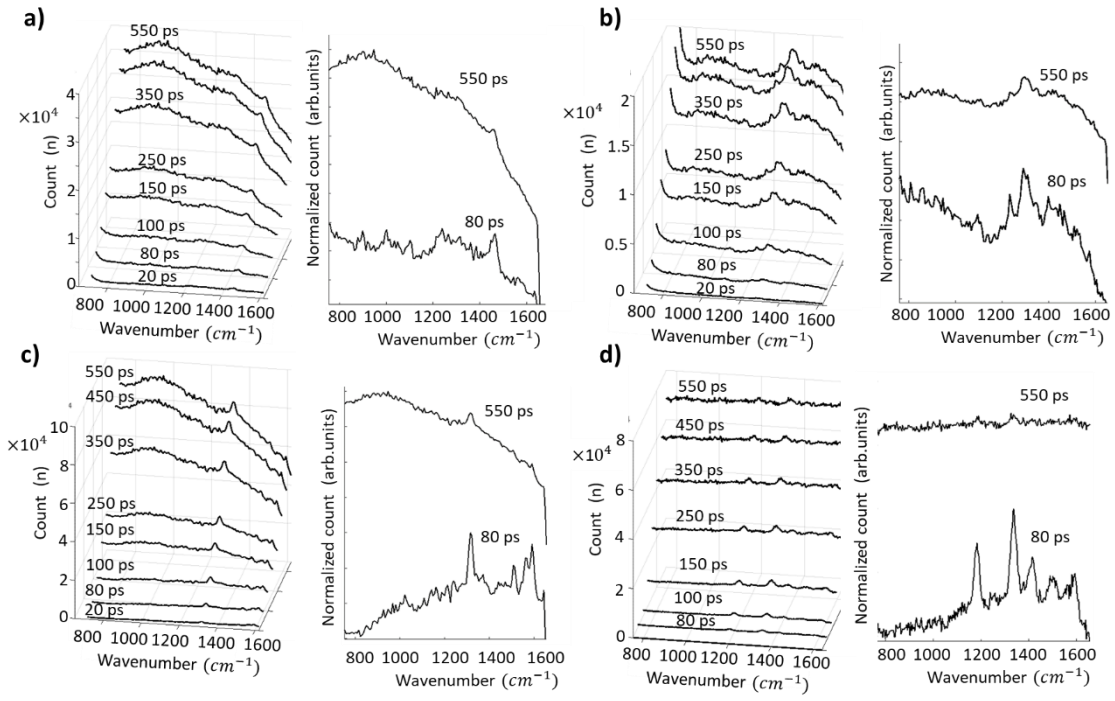

Figure 5.6. Time-gated Raman spectra of red pigments: a) Red lake pigment. b) Carmine Naccarat. c) Quinacridone Red Magenta. d) fluorescein. Times indicate width of gate window for comparison between steady state CCD based systems (0 ps begins at the time which the first Raman photons are detected.

To estimate the performance of fluorescence suppression, a simple single exponential model proposed by Everall et al [60] was used based on the ratios of the fluorophores lifetime and the width of the time gate (equation 1). This simple model has been shown to provide results consistent with experiment for Kerr gated and iCCD based time gated Raman systems. [49,60]

$$fl_{bg}/_{Raman} = \frac{\int_0^{\infty} e^{-t/t_f} dt}{\int_0^{t_g} e^{-t/t_f} dt} = \frac{1}{1-e^{-t_g/t_f}} \approx \frac{t_f}{t_g} \qquad \text{[Eq1],}$$

where t = time, t_f = fluorescence lifetime and t_g is gate width.

If we assume our minimum gate width is equal to the FWHM of the instrument response function, 60 ps, and take the lifetimes as measured from the emission curves shown in Figure 5.5, we can calculate the expected amount of fluorescence suppression using Equation 1.

We then evaluate the performance of the time gated Raman instrument by measuring the improvement factor in the Raman/fluorescence background by comparing the intensity ratios between long (CW) and optimized time gates. The measured Raman/fluorescence background ratio is calculated by integrating the Raman signal above and below the background level of the most prominent Raman peak. The measured Raman/fluorescence background ratio vs time gate data is shown in Figure 5.7. The expected and measured improvements along with the lifetimes are shown below in Table 1.

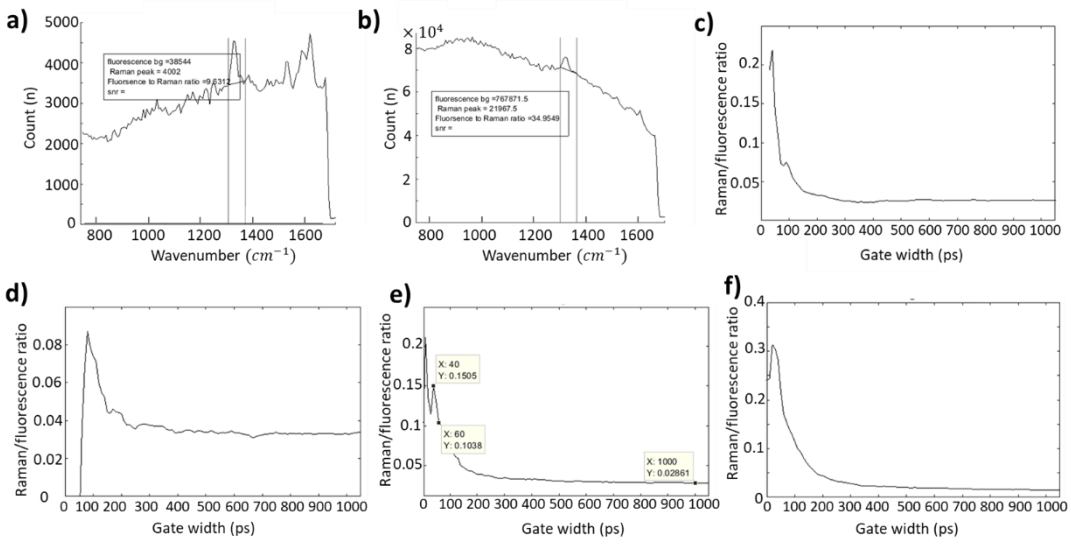

Figure 5.7. Time gated Raman spectra of Quinacridone for 60 ps (a), and 550 ps gate width (b). The vertical lines at $1310cm^{-1}$ show the spectral feature used to calculate the Raman fluorescence background ratio. c,d & e) Raman /fluorescence background ratio vs time gate for each of the samples (Red lake (c), Carmine (d), Quinacridone (e), Fluorescein (f)).

Table 1. Lifetimes predicted and measured improvement of FL/Raman.

Sample	Lifetime (ps)	Calculated Improvement Raman/fl background	Measured improvement Raman/fl background
Red lake	106	2.3	2.8
Carmine Naccarat	137	2.8	2.6
Quinacridone Red Magenta	183	3.6	3.6
Fluorescein	520	9.1	11.7

Time-gated micro-SORS for sub-surface analysis of materials with strong fluorescence backgrounds with a non-fluorescing surface layer

After establishing the main bands in the Raman spectra of the four red pigments, layered samples using fluorescein as a sub-surface layer were prepared to investigate the feasibility of using micro-SORS combined with time-gating to recover the Raman signal from fluorescing sublayer. Although micro-SORS (as well as SORS) can be used to suppress fluorescence from overlayers it cannot deal with fluorescence originating from the target sublayer. [79] As such, being able to address this analytical situation in cultural heritage is of high importance. Without loss of generality, fluorescein was selected here for demonstration of proof-of-principle, as it has the longest fluorescence lifetime out of all pigments, thus enabling the most efficient fluorescence suppression by time-gated detection.

First, a test sample was prepared with approximately 1 mm^3 of fluorescein powder, layered upon a 600 μm thick layer of Teflon (eight layers of PTFE tape). The intensity as a function of time $I(t)$ was measured separately for the Teflon, fluorescein alone and fluorescein through 600 μm of Teflon, where the measured signal consists of all excited photons, both Raman and fluorescence by multiplexing the Raman bands specific to each material. The data is combined and presented in Figure 5.8a. By comparing the data in Figure 5.8a it is observed although the fluorescein signal is

delayed due to photon diffusion, the first 100 ps of fluorescein signal overlaps temporally with the Teflon signal from the surface layer; consequently, time-gating alone cannot separate the sublayer Raman signal from the signal generated at the surface. Using a Nikon 20x 0.75 NA microscope objective, Raman spectra were acquired with the sample in focus and defocused by -200 µm and -400 µm (Figures 5.8b, c & d).

Figure 5.8b shows that when the sample is in focus, the Raman signal from the Teflon surface layer dominates the Raman signals at short gate times (Figure 5.8b e.g. 80 ps). With the gate time optimized for maximum signal from fluorescein (140 ps), the Teflon signal is still observed and the Raman band of fluorescein at 1170 cm^{-1} is just visible. For long gate widths (>500 ps) the intense fluorescence background dominates and detection of any Raman signal of fluorescein is not possible. Figure 5.8c shows that defocusing the objective by -200 µm leads to an attenuation of the signal from the Teflon surface layer. The highest intensity of fluorescein signal was observed at 140 ps (Figure 5.8c), but still the 1318 cm^{-1} peak is barely detectable. No Raman bands are observed for long time-gates (> 500 ps). When the sample was defocused further to -400 µm, the signal of Teflon surface was again attenuated at short gate times (Figure 5.8d, e.g. 80 ps), but provided the best detection of Raman bands of fluorescein at 1180 cm^{-1} and 1318 cm^{-1} at time-gates of 140 ps (Figure 5.8d). Once again, for long gate widths, the intense fluorescence background dominates, and no Raman can be retrieved.

These results demonstrate that time-gated micro-SORS provides the ability to attenuate the signal from the surface layer while allowing discrimination between Raman and fluorescence photons from the sublayer.

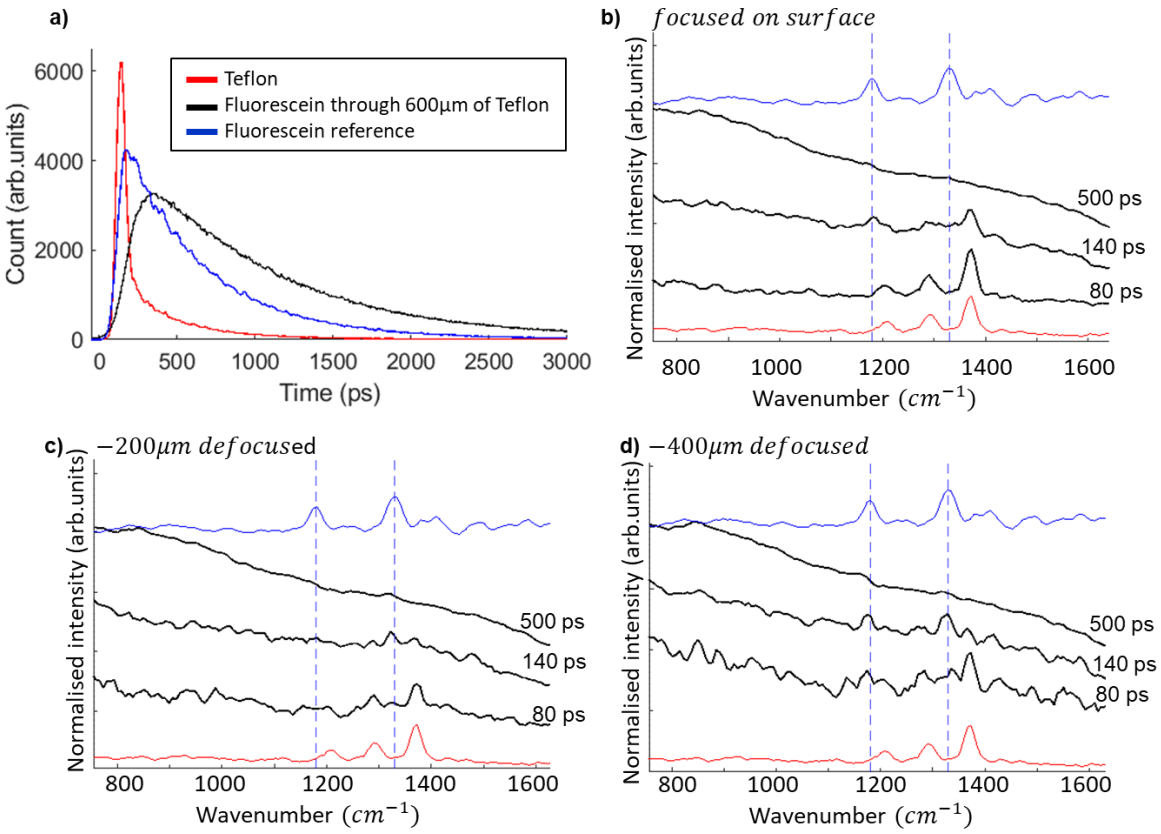

Figure 5.8 a) Composite plot combining the emission intensity as a function of time for Teflon and fluorescein reference samples and a fluorescein though 600 µm of Teflon. Data acquired by multiplexing the 1216 cm^{-1}, 1299 cm^{-1} and 1379 cm^{-1} bands for Teflon and the 1180 cm^{-1} and 1318 cm^{-1} bands for fluorescein. By comparison of the blue and black curves it is observed that although the fluorescein signal is delayed due to the photon diffusion process there is still overlap between the signal generated at the surface and the leading edge of the fluorescein signal. b) In focus time-gated Raman spectra. c). micro-SORS time-gated Raman spectra with -200 µm defocus. d) micro-SORS time-gated Raman spectra with -400 µm defocus. Blue dashed vertical lines at 1180 cm^{-1} and 1318 cm^{-1} reference fluorescein peaks.

Time-gated micro-SORS for sub-surface analysis of materials with strong fluorescence backgrounds with a highly fluorescing surface layer

The temporal overlap between the surface and the sublayer signals can be even more accentuated when both surface layer and sub-surface elicit strong fluorescence background. This most difficult case was investigated here by preparing a sample of 1 mm^3 of fluorescein powder layered behind a 100 μm thick layer of highly fluorescent brown paper. The time-gated gated Raman spectra were acquired with the sample in focus and then 400 μm defocused in order to take advantage of the micro-SORS effect. With the microscope focused on the surface of the sample, for short gate times (Figure 5.9a, e.g. 130 ps), the fluorescence background from the brown paper surface layer dominates the signal and the fluorescein spectrum is barely observed. At longer gate times (Figure 5.9a, e.g. 500 ps) the intense fluorescence background, from both the surface and sublayers, dominates and no Raman spectral bands were observed.

However, a significant enhancement in the detection of Raman bands of fluorescein was observed when the microscope was defocused by 400 μm and short gate times were selected for detection (Figure 5.9b, e.g. 130 ps). In this case, the signal from the surface layer of brown paper was sufficiently suppressed coupled with an enhancement of the sublayer to allow successful recovery of the fluorescein Raman signal. For longer gate widths (> 500 ps), the intense fluorescence background dominated, and again, no Raman spectral features were observed.

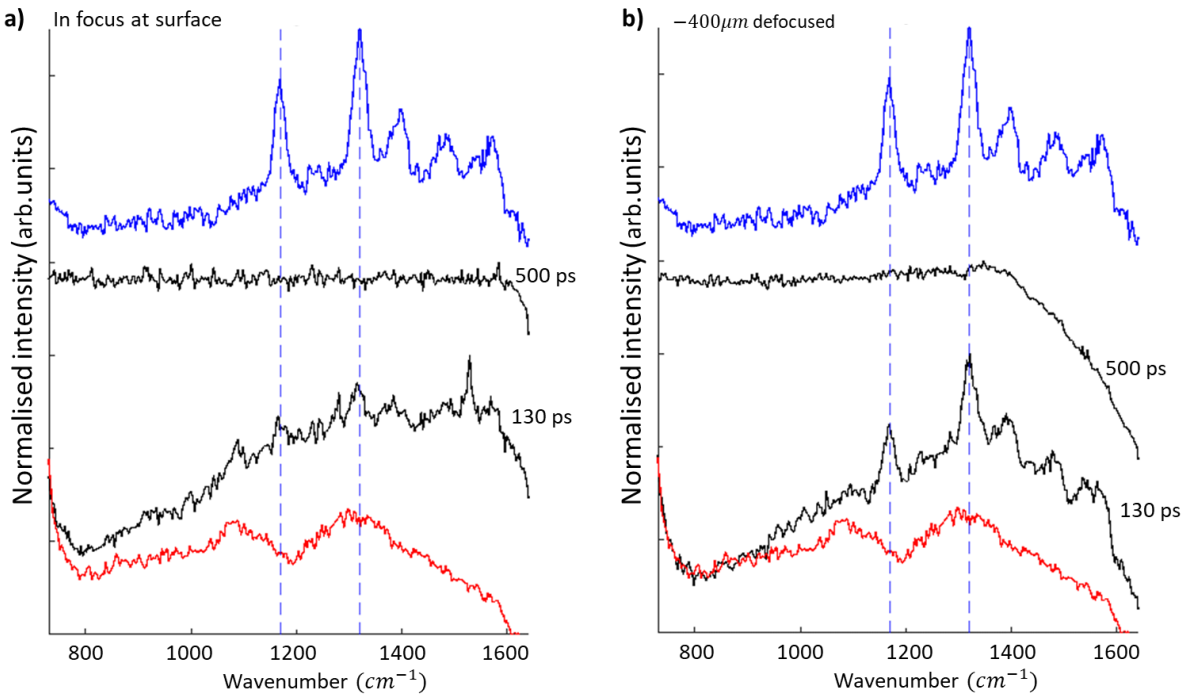

Figure 5.9. Micro-SORS time-gated Raman spectra of a layered sample consisting of 100 µm thick brown paper surface layer and fluorescein sublayer. a) Laser focused on the paper surface. b) -400 µm defocused. Time gated reference spectra of fluorescein and brown paper are shown in blue and red. Raman spectra at 130 ps time-gate (highest intensity of fluorescein Raman signals) are compared to Raman spectra at 500 ps time-gate.

These results demonstrate that the combination of time-gated and micro-SORS is a powerful approach for Raman analysis of subsurface fluorescing materials. Although the defocusing micro-SORS used here led to a decrease in the signal to noise ratio, it is possible to employ more signal-efficient micro-SORS techniques, such as DMD-based micro-SORS to generate ring collection geometries. These techniques could significantly increase the optical throughput and decrease the acquisition times, as required for real-world applications.

Conclusion

By considering scattered photons through diffusive media, we have applied time-gated and spatially-offset Raman spectroscopy to obtain sub surface molecular analysis and imaging for both fluorescing and non-fluorescing samples. The multiplexed spectral detection enabled by a digital micromirror device (DMD) allowed fast acquisition of the time-gated signals to enable 3D Raman maps (raster scanning in the lateral *x*-*y* plane and use time-of-flight calibration for the axial *z*-direction). Utilizing the signal-to-noise advantage obtained by spectral multiplexing and operating in a time correlated single photon counting (TCSPC) mode, sub millimetre resolution molecular depth mapping can be achieved with dwell times on the order of seconds per pixel. Further improvements in the depth accuracy could be made by improving the calibration (machining more precise uniform calibration blocks) and the data analysis methods (fitting a more complex model to the data to account for scattering attenuation).

Defocusing and scattering of the excitation beam and Raman scattered light limits the lateral resolution for depth measurements. However, because of this, further speed improvements could be made by using a higher laser power without risk of laser damage to the sample (50 mW laser power was used for the depth measurements).

Time-gated Raman spectroscopy was successfully applied to record Raman spectra common red pigments encountered in cultural heritage. In spite of the very short fluorescence lifetimes in the 100-550 ps range, the instrument provided efficient rejection of the fluorescence background enabling detection of the main Raman bands.

Finally, we combined time-gating and micro-SORS to recover the Raman signals of red pigments placed behind layers of optically turbid materials. Using defocusing micro-SORS, both fluorescence and Raman signals from the surface layers were further suppressed to enable enhanced detection of the Raman signals from the deeper sublayer. Although the spectral multiplexing enabled by the DMD allowed sufficient detection of the Raman signals, further improvements in the data acquisition speed could be made using DMD-based micro-SORS techniques that have typically higher optical throughput. [83] Such techniques can reduce the acquisition times to levels required for real-life applications.

The combination of a single pixel, cooled detector operating in TCSPC mode with a DMD as the wavelength selective component provides a solution to many of the technical limitations current time gating techniques face. The DMD has a high fill factor of 92% and multiplexing provides a significant signal to noise advantage. The gated dark count rate of the detector is significantly less than the continuous dark count (<0.5 cps gated). The single pixel SPAD coupled with optimized optics and 30 ps laser pulse results in an IRF FWHM of 60 ps for the whole instrument – essential for effective suppression of short-lived fluorophores and high-resolution depth measurements. In conclusion, we showed that time-gated Raman spectroscopy based on multiplexed detection, and combination with micro-SORS, is a powerful technique for subsurface molecular analysis and imaging, which can find practical applications in medical imaging, art and cultural heritage, forensics, and industry.

Chapter 6. Additional experimental results

6.1 Time Gating for Raman spectroscopy in ambient lighting conditions.

Raman spectroscopy, although an extremely powerful tool for measuring the presence of molecular vibrations is usually restricted to a specialised, light tight instrument in a laboratory.

If we are to develop a real time scanner for the molecular classification of materials in the world outside of a laboratory, we must negate the effects of the ambient lighting. Using optical filters, we can be sure to collect only the spectral regions of interest and effectively block a large portion of background. Ambient background lighting, however, is usually a broadband spectrum spanning from the UV into the IR.

Using a pulsed excitation and time gated detection method, the background noise can be reduced by orders of magnitude. For every period T (1/rep rate), the detection method is configured to only acquire photons from the gate window of width $t_{g.}$ Photons incident on the detector that lie outside of the gate window will not be detected and thus do not contribute to the background. Our system can operate with a temporal resolution of 65 ps at 10MHz meaning than for a 100 ps gate window we can have a reduction in background noise by a factor of 1000X.

If suppression of ambient lighting is the only goal, then such high levels of temporal resolution are not necessary. A 1 ns pulsed laser and detection system could be produced for much less than the 30 ps system we currently use thanks to the recent advances in lidar and laser range finding technology. Operating at 10MHz repetition

rate the 1ns temporal resolution would still provide 2 orders of magnitude suppression of ambient background light.

The instrument was configured as in figure 3.24. That is, the 2nd spectrograph was used to recombine the spectrum and focus the light onto the PDM 100CTE SPAD.

As an example, the Raman spectrum of polystyrene is measured using a laboratory grade Raman spectrometer consisting of a Andor spectrograph and CCD detector with a broadband background light source (microscope halogen lamp). The lamp is adjusted

so that Raman spectrum of polystyrene is completely buried within the background noise (Figure 6.1a&b). The 1001 cm^{-1} wavenumber peak can just be seen but the spectrum is essentially useless.

The same level of background and laser power were kept while the instrument is switched to DMD scanning mode. The time gated Raman spectrum is acquired with the halogen lamp on then switched off for a reference spectrum. The time gated spectra are shown in Figure 6.2 for 100, 300, 1000 & 3400 ps gate widths.

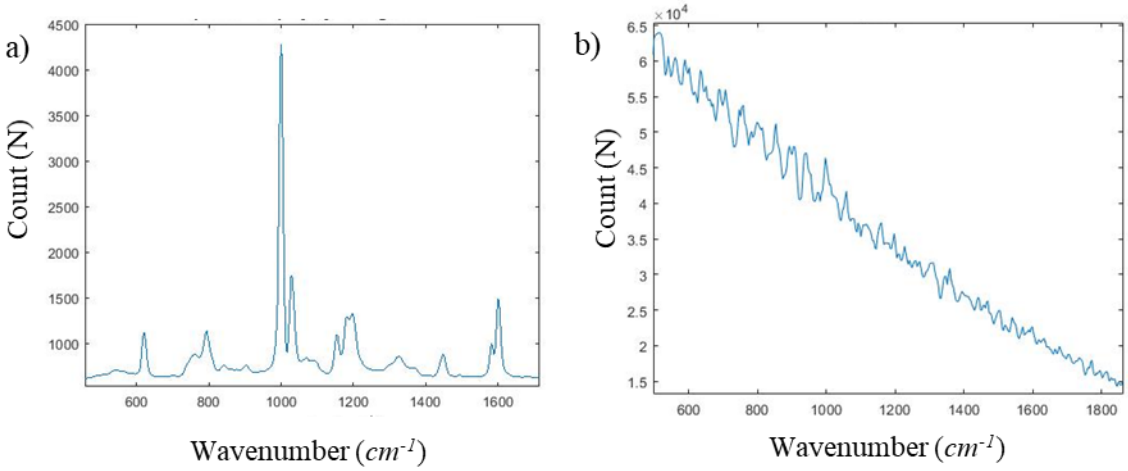

Figure 6.1 Raman spectrum of polystyrene with 45mW excitation with 1s integration using Andor 401 CCD. a) No background light. b) broadband background light source contaminating signal (microscope halogen lamp).

The best signal to noise is achieved between ~100 and 400 ps gate width. Although, a 1ns gate width provides adequate reduction in background for recovery of the signal.

This shows that even a relatively low-resolution pulsed laser detection system is a powerful technique that can be implemented if a portable Raman instrument is to be developed for optically noisy environments.

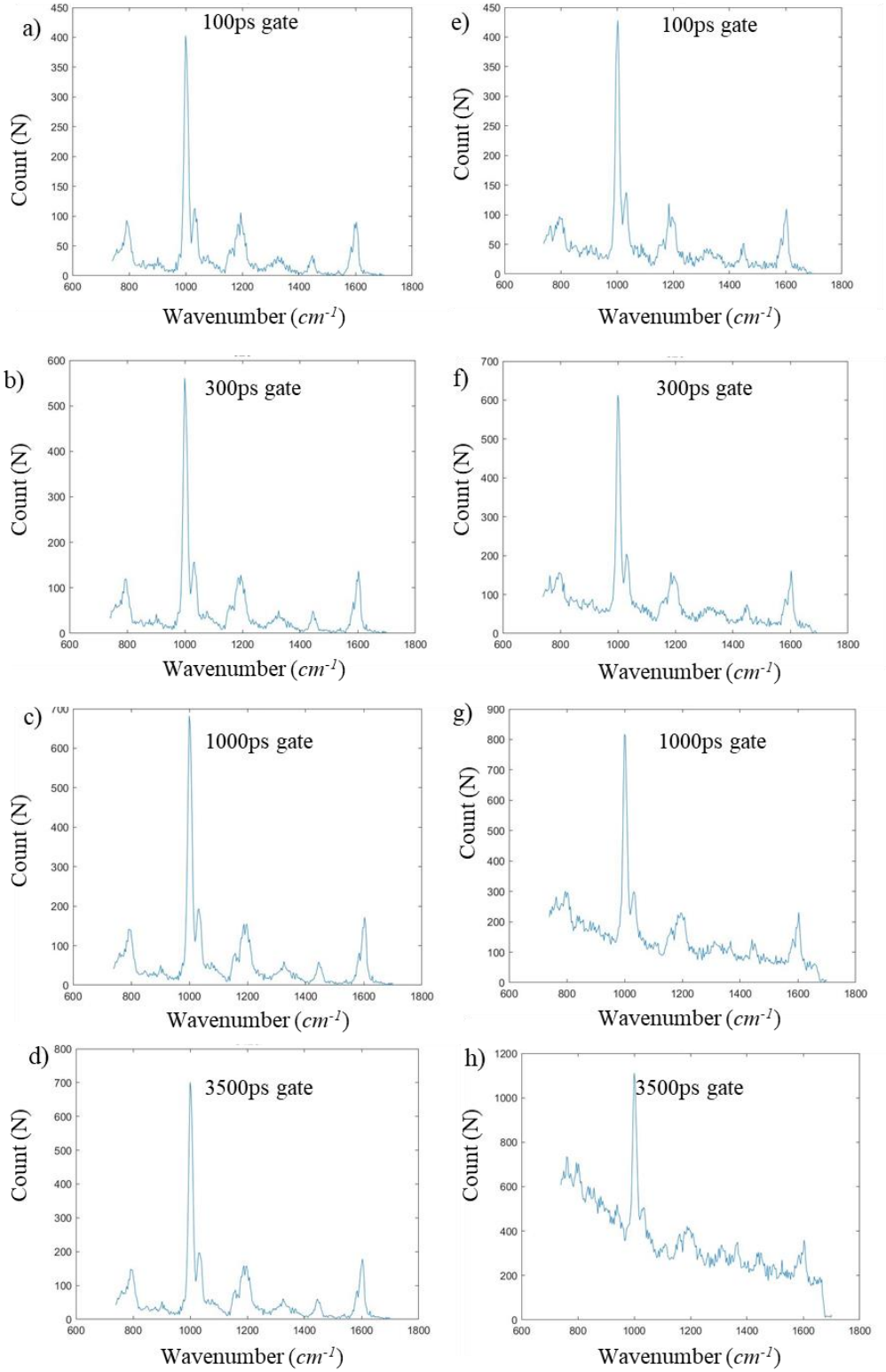

Figure 6.2 a-d) Time gated Raman spectra of polystyrene with no background light. 6.2e-h) Time gated Raman spectra for the same broadband background intensity that is shown in figure 6.1b.

6.2 Two photon excitation

As 775 nm photons are of insufficient energy to excite many electronic states it has been suggested the two photon excitation may be responsible for the intense background in the NIR region. With a pulsed laser, the photon density of each pulse is enough that the probability of two photon excitation needs to be considered.

The probability of a multiphoton process is low and requires a high flux of excitation photons (100 MW/cm^2 to 100 GW/cm^2) [92]. Each pulse of the laser at 65mW average power is 6.5 nJ with a pulse width of 31 ps. Pulse power of the Katana is therefore 775 = 6.5 nJ/31 ps = 210 W

Using a 50X Leica objective we measure the laser spot to be.

3 µm diameter = $7 \times 10^{-12} m^2 \; = \; 7 \times 10^{-8} cm^2$

$210(W)/7 \times 10^{-8} cm^2 \; = \; 2.97 \times 10^{9} W cm^{-2} \; \sim 3 GW cm^{-2}$

The photon density is in the regime required for two photon excitations. As two photon excitation is a non-linear effect this hypothesis can easily be tested by measruring the background intensity as a function of excitation energy. A linear response would indicate single photon fluorescence, whereas two photon fluorescence will show a quadratic response.

To measure any potential effects such as two photon excitation (TPE) fluorescence or second harmonic generation, the instrument is modified as in Figure 6.3. Photons with a wavelength shorter than the 780 nm cut off of the dichroic mirror (DM1) are reflected back down the same optical path of the laser. A 2nd dichroic beam splitter (DM2) is used to reflect wavelegths below 600 nn to be focused onto an optical fiber via a short pass filter (SPF) and a lens (L).

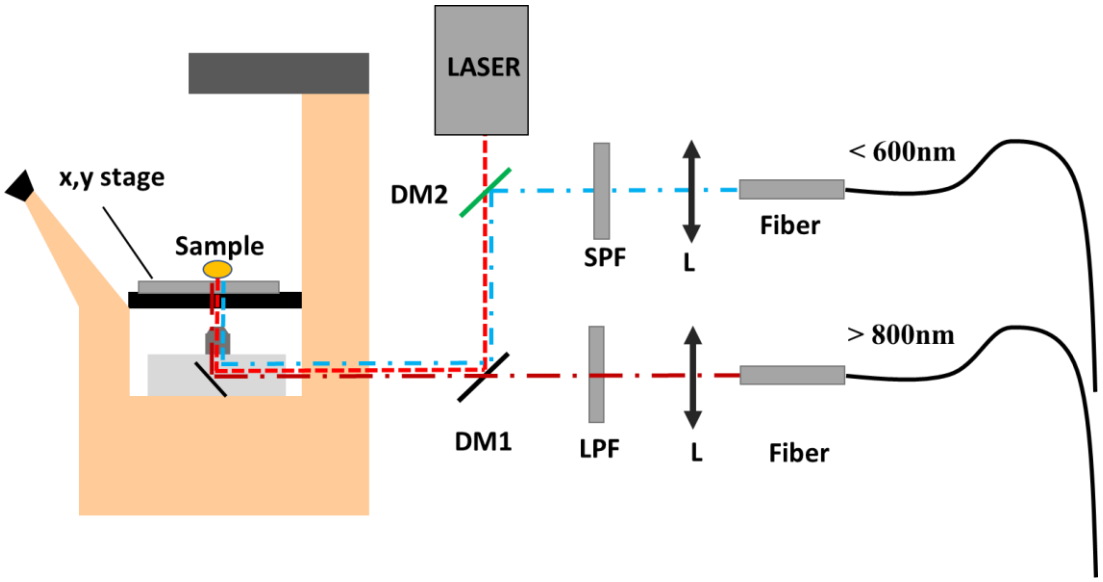

Figure 6.3 Additional optical path added to detect the 300 – 600 nm range. Light from the sample plane with wavelengths less than 760 nm is reflected back down the laser path by DM1 and again by DM2. The filtered 300-600 nm range is focused onto the fiber via an AC127 030A lens.

The short wavelength optics are connected to a separate spectrometer and CCD so that the relationships between single photon and two photon excitaion can be observed.

The measured intensity vs excitation is measured for a range of samples for both the 300-600 nm range and the 800-900 nm range. Figures 6.4 – 6.7 shows preliminary results of various samples. Samples were selected that are known to exhibit intense backgrounds with NIR excitation. Chlorophyl rich fresh green grass (Figure 6.4), quinacridone red (figure 6.4) (a pigment used in the paint industry) and fluorescein (Figure 6.6). In this case, a water soluble variant of fluorescein was used and the powder was dissolved in water at an unknown concentration. It should be noted that it was found that the dissolved aqueous solution responds differently than pure dry powder by producing almost no background in the NIR. It is presented here only because the result provided an interesting comparison due to a strong two photon fluorescence response.

For each of the samples, the background level was measured at 820 nm (~710 cm^{-1}) using the SPAD, and the 300-600 nm range was captured using the CCD. Data was acquired for 1 s integration while increasing the laser power at the sample from 1-50 mW.

The results are arranged as follows; figure (a) shows the temporal response of the SPAD for 50 mW excitation with 820 nm detection. Figure (b) shows the spectrum recorded by the CCD at 50 mw excitation for 300 – 600 nm. Figure (c) shows the total photon count of the SPAD as a function of laser power. Figure (d) shows the total count of the CCD for (300-600 nm) as a function of laser power.

If the fluorescence background at 820 nm as detected by the SPAD is due to two photon fluoresence we would expect to see a quadratic response in the intensity as a function of wavelength (c). Also, we would expect that any two photon excitation would present as a strong response in the 387.5 nm – 600 nm region and the corresponding intensity as a function of power (figure d) would be quadratic.

For samples that generate intense fluorescence backgrounds in the NIR regime it is observed that there was very little corresponding signal in the 300- 600 nm region. The response was measured to be approximately linear in most cases however, without photobleaching, the intensity as a function of laser power presents as decaying curve (figure 6.5c).

The fluorescein in water solution on the other hand exhibited the opposite effect. Very little background in the NIR region (figure 6.6a) and the corresponding response of the measured intensity as a function of excitation power presents as a linear response (figure 6.6c). Whereas, the intensity measured at 300 - 600 nm shows a typical fluorescein fluorescence emsision curve (6.6b). The response of the 300 - 600 nm region shows a quadratic response as would be expected from two photon excitation Figure (6.6d)

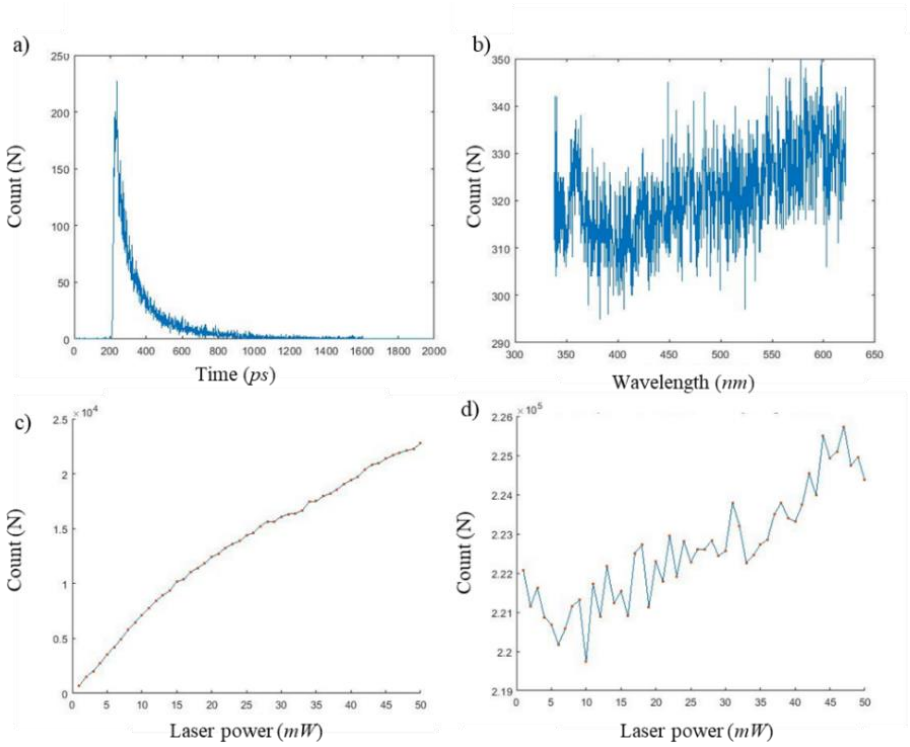

Figure 6.4 a) Signal generated by fresh green grass. a) I(t) at 820 nm detection (50mW). b) Spectrum of 300-600 nm measured by Andor iDUS CCD (50mW). Total measured intensity as a function of incident laser power for c)820 nm and d)300-600 nm.

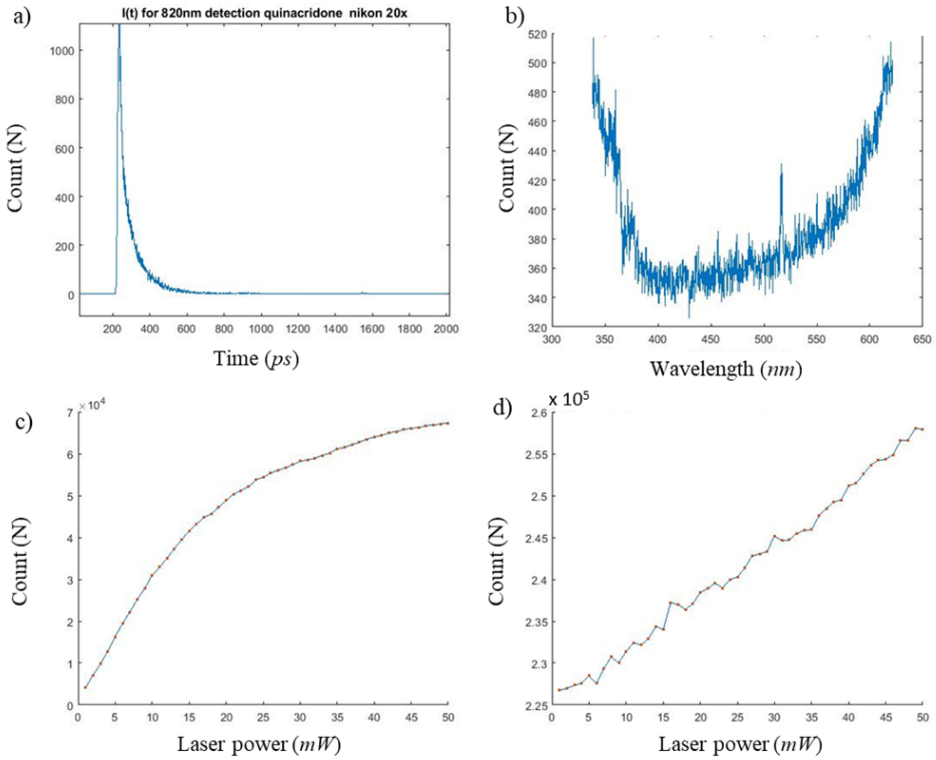

Figure 6.5 a) Signal generated by Quinacridone red pigment. a) I(t) at 820 nm detection (50 mW). b) Spectrum of 300-600 nm measured by Andor iDUS CCD (50 mW). Total measured intensity as a function of incident laser power for c)820 nm and d)300-600 nm.

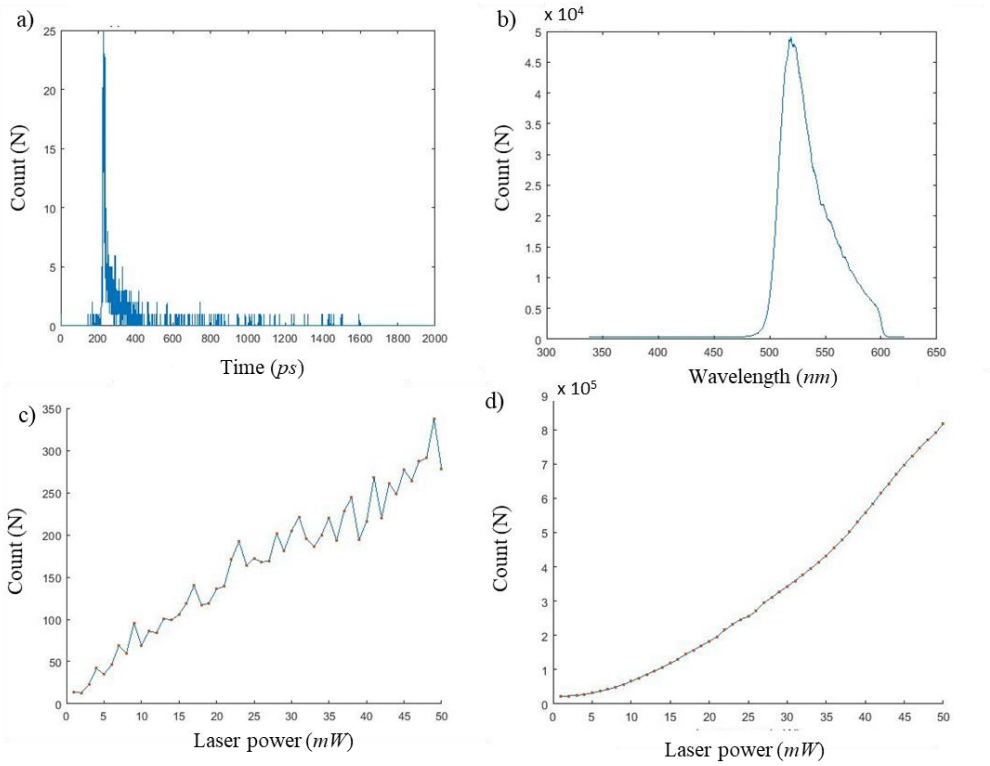

Figure 6.6. Measured intensity of fluorescein dye in water. a) I(*i*) at 820 nm detection (50 mW). b) Spectrum of 300-600 nm measured by Andor iDUS CCD (50 mW). Total measured intensity as a function of incident laser power for c)820 nm and d)300 - 600 nm.

For the samples that exhibit high levels of NIR autofluorescence (chlorophyl and quinacridone) only linear responses of the signal as a function of laser power were observed in the 800-900 nm regime even after extensive photo bleaching. The linear response of the NIR signal as a function of excitation power confirms that the fluorescence background in these samples is not due to nonlinear effects such as two photon excitation or second harmonic generation.

In the case of fluorescein dye in water, a strong two photon excitation is observed in the 300-600 nm range. A power fit to the intensity vs excitation power yields a power coefficient of 1.7 (Figure 6.7).

The lack of corresponding background in the 800-900 nm range while generating TPE adds further evidence that the fluorescence background at NIR is not related to TPE.

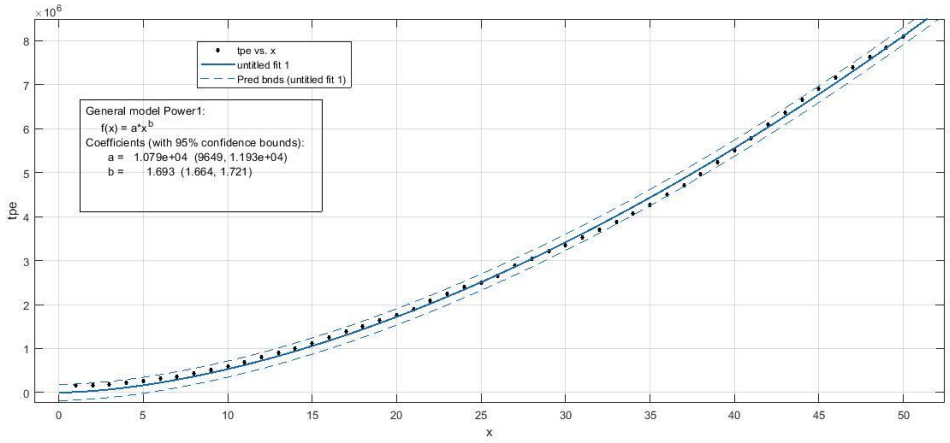

Figure 6.7. Fit to two photon intensity as a function of excitation power for fluorescein dye in water. Excitation - 775 nm. Detection - integrated signal from 300-600 nm.

6.3 Temporal response of biological materials (preliminary results)

The temporal profile of biological samples was measured to determine the potential reduction in fluorescence background through time gating. A fresh green privet leaf was used as chlorophyl source and horse blood was used as a source of protoporphyrin IX. Elastin and collagen samples were 99 % pure dry powder from Sigma Aldrich.

The preliminary results are shown in Figure 6.8. The instrument response function is shown as the blue curve and the black curve is the sample being measured. A mono exponential fit to the data is used to estimate the lifetimes and the result of the samples are compared in table 6.1.

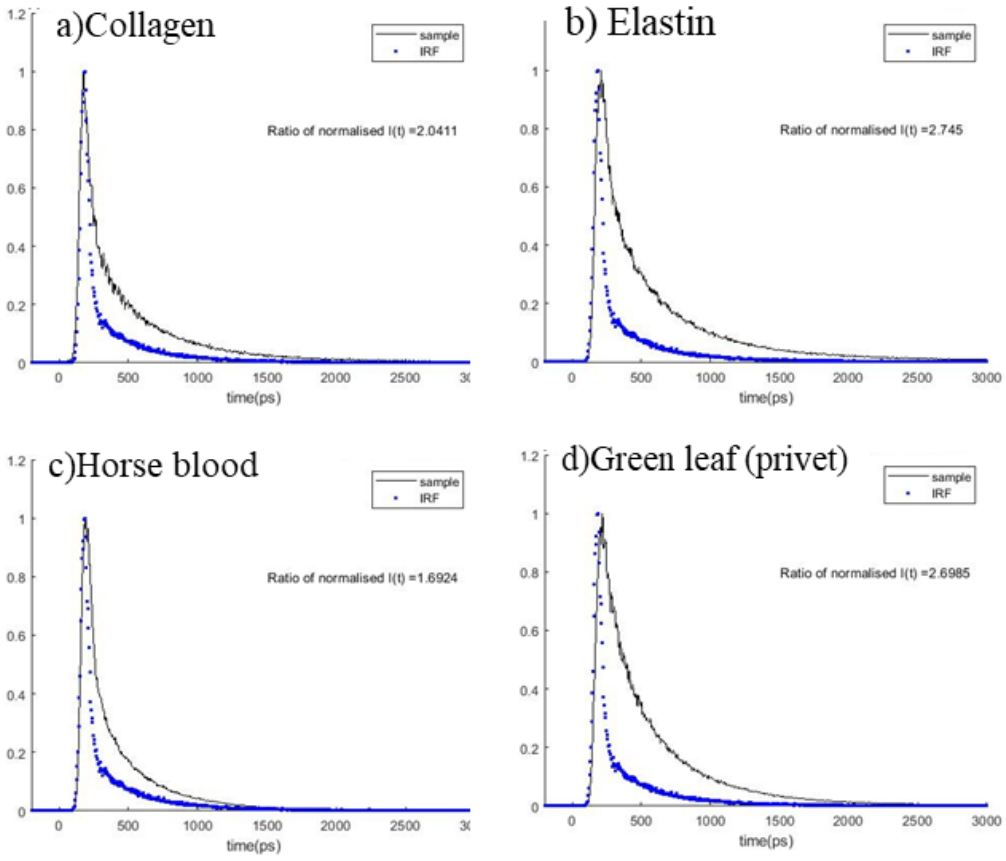

Figure 6.8.Temporal response of biological samples for 775 nm excitation and 820 nm detection. Blue curve represents IRF. a) collagen. b) Elastin c) Horse blood d)Fresh green privet leaf.

Table 6.1 lifetimes of biological samples taken from the literature (blue)(references in table 2.1). Measured lifetimes using 775 nm excitation (red)

Fluorophore	Excitation (nm)	Emission (nm)	Lifetime, (ns)	Predicted suppression factor (60 ps gate)
Protoporphyrin IX	400-450	710	15.9	265
Protoporphyrin IX	400-500	633	8.4-13	140-217
Elastin	337	>345	2.3	23
Collagen	337	>345	5.3ns	89
Chlorophyl a	430,662	650-700,710-740	0.17-3ns	3.4-50
Collagen	775	820	0.25	4.7
Elastin (powder)	775	820	0.33	6
Horse blood	775	820	0.17	3.4
Leaf (Chlorophyl)	775	820	0.32	5.8

7 Conclusions and future prospects

The work in this thesis shows that the added temporal dimension can provide background reduction from fluorescence while offering depth information of optically turbid samples on time scales comparable to conventional, steady state Raman instruments thanks to compressive detection techniques. Furthermore, time gating techniques offers the advantage of significant reduction in detector thermal noise and ambient light.

Confirmation that the NIR fluorescence was due to single photon interactions was made by observing the linear response of the background to changing excitation power. Further confirmation was provided by simultaneously measuring two photon fluorescence and second harmonic generation through the addition of another optical path connected to a separate spectrometer. The results show no correlation between NIR fluorescence and two photon interactions.

All values stated for the lifetimes of the fluorophores in the literature are for excitation in the visible regime. Not one instance was found with lifetimes of fluorophores with NIR excitation. Of the samples measured, porphyrin structures are suggested to be the source of the background and the lifetimes measured with 775 nm excitation are between 170-300 ps; much less than any values stated in the literature.

Consequently, the performance of fluorescence suppression using 775 nm excitation was found to be less than expected (based upon the calculations based upon the values found in the literature).

Nevertheless, the design and application of the instrument was successful and demonstrates a potential route to a fast, multimodal instrument capable of simultaneously measuring Raman intensity, fluorescence intensity and fluorescence lifetimes, while providing adequate photon densities to excite two photon fluorescence and second harmonic generation.

The reduction in ambient background offered by time gating means that such a system, once optimized, has the potential to provide molecular classification in real world conditions under ambient lighting. For example, a surgeon could acquire a spectrum from a patient in real time while operating in normal conditions.

The DMD optical filters in this work were manually determined, however, compressive detection mathematical models can be applied to the optical filters to provide greater contrast between samples. The work in this area is developing rapidly and compressive detection techniques have been shown to be superior to hyperspectral techniques in the low signal domain where read noise becomes the dominant source of noise.

Future work will involve utilizing the full capability of the multimodal instrument for the analysis of highly fluorescent samples in science, art and industry. Improved fitting and deconvolution techniques will be applied to the temporal response of the fluorescence signal. With more precise measurements of the lifetimes coupled with time gated Raman spectroscopy we aim to identify the fluorochromes responsible for the high background at NIR excitation.

The technique could be applied to stand off Raman detection of materials such as have been demonstrated in [93–95] to detect explosives from afar. This could potentially result in a further improved SNR and potentially offer a solution for detecting roadside explosives in war zones in real time.

Time gated multiplexing with 1064 nm excitation offers potential. Multiplexing the signal would compensate for the low Raman scattering cross section to a degree while the time gating would allow a significant reduction in the high thermal noise typically attributed to InGaAs detectors. Furthermore 1064 would offer even better depth detection due to the reduced levels of absorption in tissue and other optically turbid samples. On the other hand, this technique applied in the UV regime could yield superior results for situations where photodamage is not an issue.

When SPAD arrays can be produced with comparable specifications to a research grade CCD, then undoubtably, they will become the detector of choice for future researchers and industry. That is, with high fill factors and quantum efficiencies, low dark counts, and consistent temporal resolution across the whole arrays with on pixel TDCs.

References

1. C. V. Raman and K. S. Krishnan, "A new type of secondary radiation," Nature **121**, 501–502 (1928).

2. J. R. Lakowicz, *Principles of Fluorescence Spectroscopy Principles of Fluorescence Spectroscopy*, 3rd ed. (Springer science & business media, 2006).

3. J. Kostamovaara, J. Tenhunen, M. Kögler, I. Nissinen, J. Nissinen, and P. Keränen, "Fluorescence suppression in Raman spectroscopy using a time-gated CMOS SPAD.," Opt. Express **21**, 31632–31645 (2013).

4. P. Matousek, M. Towrie, A. W. Parker, C. L. Facility, C. Rutherford, C. Ma, W. M. Kwok, and D. Phillips, "Fluorescence Suppression in Raman Spectroscopy using a High Performance Picosecond Kerr Gate," J. Raman Spectrosc. **32**, 983–988 (2001).

5. D. V. Martyshkin, R. C. Ahuja, A. Kudriavtsev, and S. B. Mirov, "Effective suppression of fluorescence light in Raman measurements using ultrafast time gated charge coupled device camera," Rev. Sci. Instrum. **75**, 630–635 (2004).

6. K. H. Howard, J, N J Everall, R W Jackson, "Fluorescence rejection in Raman spectroscopy using a synchronously pumped, cavity- dumped dye laser and gated photon counting," J. Phys. E. **934**, (1986).

7. A. C. Menzies, "The Raman Effect," Nature **125**, 205–207 (1930).

8. C. V. Raman and K. S. Krishnan, "A new type of secondary radiation [11]," Nature **121**, 501–502 (1928).

9. D. A. Long, *The Raman Effect* (Wiley, 2002), Vol. 8.

10. R. F. Chen, "Fluorescence quantum yields of tryptophan and tyrosine," Anal. Lett. **1**, 35–42 (1967).

11. C. D. McGuinness, A. M. Macmillan, K. Sagoo, D. McLoskey, and D. J. S. Birch, "Excitation of fluorescence decay using a 265 nm pulsed light-emitting diode: Evidence for aqueous phenylalanine rotamers," Appl. Phys. Lett. **89**, 1–4 (2006).

12. K. König, "Clinical multiphoton tomography," J. Biophotonics **1**, 13–23 (2008).

13. G. S. Singhal and E. Rabinowitch, "MEASUREMENT OF THE FLUORESCENCE LIFETIME OF CHLOROPHYLL a IN VIVO," Biophys. J. **9**, 586–591 (1968).

14. J. H. Brannon and D. Magde, "Absolute quantum yield determination by thermal blooming. Fluorescein," J. Phys. Chem. **82**, 705–709 (1978).

15. J.-M. I. Maarek, L. Marcu, W. J. Snyder, and W. S. Grundfest, "Time-resolved Fluorescence Spectra of Arterial Fluorescent Compounds: Reconstruction with the Laguerre Expansion Technique," Photochem. Photobiol. **71**, 178 (2000).

16. T. Glanzmann, J. P. Ballini, H. Van Den Bergh, and G. Wagnières, "Time-resolved spectrofluorometer for clinical tissue characterization during endoscopy," Rev. Sci. Instrum. **70**, 4067–4077 (1999).

17. M. Y. Berezin and S. Achilefu, "Fluorescence lifetime measurements and biological imaging," Chem. Rev. **110**, 2641–2684 (2010).

18. L. Sauer, A. S. Vitale, C. M. Milliken, N. K. Modersitzki, J. D. Blount, and P. S. Bernstein, "Autofluorescence Lifetimes Measured with Fluorescence Lifetime Imaging Ophthalmoscopy (FLIO) Are Affected by Age , but Not by Pigmentation or Gender," 1–13 (2020).

19. A. Chorvatova and D. Chorvat, "Tissue fluorophores and their spectroscopic characteristics," Fluoresc. Lifetime Spectrosc. Imaging Princ. Appl. Biomed. Diagnostics 47–76 (2014).

20. Z. Huang, A. McWilliams, H. Lui, D. I. McLean, S. Lam, and H. Zeng, "Near-infrared Raman spectroscopy for optical diagnosis of lung cancer," Int. J. Cancer **107**, 1047–1052 (2003).

21. I. J. Pence, C. A. Patil, C. A. Lieber, and A. Mahadevan-Jansen, "Discrimination of liver malignancies with 1064 nm dispersive Raman spectroscopy," Biomed. Opt. Express **6**, 2724 (2015).

22. C. G. Atkins, K. Buckley, M. W. Blades, and R. F. B. Turner, "Raman Spectroscopy of Blood and Blood Components," Appl. Spectrosc. **71**, 767–793

(2017).

23. N. M. Htun, Y. C. Chen, B. Lim, T. Schiller, G. J. Maghzal, A. L. Huang, K. D. Elgass, J. Rivera, H. G. Schneider, B. R. Wood, R. Stocker, and K. Peter, "Near-infrared autofluorescence induced by intraplaque hemorrhage and heme degradation as marker for high-risk atherosclerotic plaques," Nat. Commun. **8**, 1–16 (2017).

24. S. Franzen, S. E. Wallace-Williams, and A. P. Shreve, "Heme charge-transfer band III is vibronically coupled to the Soret band," J. Am. Chem. Soc. **124**, 7146–7155 (2002).

25. W. A. Eaton, L. K. Hanson, P. J. Stephens, J. C. Sutherl, and J. B. R. Dunn, "Optical Spectra of Oxy- and Deoxyhemoglobin," J. Am. Chem. Soc. **100**, 4991–5003 (1978).

26. B. R. Wood, P. Caspers, G. J. Puppels, S. Pandiancherri, and D. McNaughton, "Resonance Raman spectroscopy of red blood cells using near-infrared laser excitation," Anal. Bioanal. Chem. **387**, 1691–1703 (2007).

27. M. Uttamlal and A. Sheila Holmes-Smith, "The excitation wavelength dependent fluorescence of porphyrins," Chem. Phys. Lett. **454**, 223–228 (2008).

28. T. Azumi and K. Matsuzaki, "What does the term “vibronic coupling’ mean?," Photochem. Photobiol. **25**, 315–326 (1977).

29. B. K. Yoo, S. G. Kruglik, I. Lamarre, J. L. Martin, and M. Negrerie, "Absorption band III kinetics probe the picosecond heme iron motion triggered by nitric oxide binding to hemoglobin and myoglobin," J. Phys. Chem. B **116**, 4106–4114 (2012).

30. C. M. Schmidt and K. a Trentelman, "1064 nm dispersive Raman micro-spectroscopy for the in-situ identification of organic red colorants," e-Preservation Sci. **6**, 10–21 (2009).

31. C. A. Patil, I. J. Pence, C. A. Lieber, and A. Mahadevan-Jansen, "1064 nm dispersive Raman spectroscopy of tissues with strong near-infrared autofluorescence," Opt. Lett. **39**, 303 (2014).

32. K. Golcuk, G. S. Mandair, A. F. Callender, N. Sahar, D. H. Kohn, and M. D. Morris, "Is photobleaching necessary for Raman imaging of bone tissue using a green laser?," Biochim. Biophys. Acta - Biomembr. **1758**, 868–873 (2006).

33. V. Viswanathan, T. K. Gundu Rao, and P. Bhama Iyer, "Raman spectrum of cellulose from cotton," Indian J. Fibre Text. Res. **24**, 78–80 (1999).

34. A. P. Shreve, N. J. Cherepy, and R. A. Mathies, "Effective Rejection of Fluorescence Interference in Raman Spectroscopy Using a Shifted Excitation Difference Technique," Appl. Spectrosc. **46**, 707–711 (1992).

35. P. J. Cadusch, M. M. Hlaing, S. A. Wade, S. L. McArthur, and P. R. Stoddart, "Improved methods for fluorescence background subtraction from Raman spectra," J. Raman Spectrosc. **44**, 1587–1595 (2013).

36. Y. Hu, T. Jiang, A. Shen, W. Li, X. Wang, and J. Hu, "A background elimination method based on wavelet transform for Raman spectra," Chemom. Intell. Lab. Syst. **85**, 94–101 (2007).

37. A. O'Grady, A. C. Dennis, D. Denvir, J. J. McGarvey, and S. E. J. Bell, "Quantitative Raman spectroscopy of highly fluorescent samples using pseudosecond derivatives and multivariate analysis," Anal. Chem. **73**, 2058–2065 (2001).

38. D. Zhang and D. Ben-Amotz, "Enhanced chemical classification of Raman images in the presence of strong fluorescence interference," Appl. Spectrosc. **54**, 1379–1383 (2000).

39. C. A. Lieber and A. Mahadevan-Jansen, "Automated Method for Subtraction of Fluorescence from Biological Raman Spectra," Appl. Spectrosc. **57**, 1363–1367 (2003).

40. S. Burgess and I. W. Shepherd, "Fluorescence suppression in time-resolved Raman spectra," J. Phys. E. **10**, 617 (1977).

41. P. Matousek, M. Towrie, and A. W. Parker, "Efficient Rejection of Fluorescence from Raman Spectra Using Picosecond Kerr Gating," Appl. Spectr. **53**, 1485–1489 (1999).

42. I. Nissinen, J. Nissinen, P. Keränen, D. Stoppa, and S. Member, "A 16 × 256

SPAD Line Detector With a 50-ps, 3-bit, 256-Channel Time-to-Digital Converter for Raman Spectroscopy," **18**, 3789–3798 (2018).

43. C. Bruschini, H. Homulle, I. M. Antolovic, S. Burri, and E. Charbon, "Single-photon avalanche diode imagers in biophotonics: review and outlook," Light Sci. Appl. **8**, (2019).

44. Timegate instruments, "TimeGate Instruments," http://www.timegate.fi/.

45. Hamamatsu Photonics "High Sensitivity Cameras: Principle and Technology," 1–8. https://www.hamamatsu.com/resources/pdf/sys/e_dctn1.pdf (2006).

46. J. Selb, D. K. Joseph, and D. A. Boas, "Time-gated optical system for depth-resolved functional brain imaging," J. Biomed. Opt. **11**, 044008 (2006).

47. J. H. Hooijschuur, I. E. Iping Petterson, G. R. Davies, C. Gooijer, and F. Ariese, "Time resolved Raman spectroscopy for depth analysis of multi-layered mineral samples," J. Raman Spectrosc. **44**, 1540–1547 (2013).

48. F. Ariese, H. Meuzelaar, M. M. Kerssens, J. B. Buijs, and C. Gooijer, "Picosecond Raman spectroscopy with a fast intensified CCD camera for depth analysis of diffusely scattering media †," 1192–1197 (2009).

49. E. V Efremov, J. B. Buijs, C. Gooijer, and F. Ariese, "Fluorescence Rejection in Resonance Raman Spectroscopy Using a Picosecond-Gated Intensified Charge-Coupled Device Camera," **61**, 571–578 (2007).

50. B. Lee, "Texas Instruments_Introduction to Digital Micromirror Devices (DMDs)," 1–13 (2008).

51. P. Nelson, "Texas Instruments DLP ® Technology for Spectroscopy," 1–8 (2014).

52. F. Sinjab, Z. Liao, and I. Notingher, "Applications of Spatial Light Modulators in Raman Spectroscopy," **73**, 727–746 (2019).

53. D. Cebeci, B. Mankani, and D. Ben-Amotz, "Recent Trends in Compressive Raman Spectroscopy Using DMD-Based Binary Detection," J. Imaging **5**, 1 (2018).

54. C. Scotté, H. B. De Aguiar, D. Marguet, E. M. Green, P. Bouzy, S. Vergnole,

C. P. Winlove, N. Stone, and H. Rigneault, "Assessment of Compressive Raman versus Hyperspectral Raman for Microcalcification Chemical Imaging," Anal. Chem. **90**, 7197–7203 (2018).

55. D. S. Wilcox, G. T. Buzzard, B. J. Lucier, O. G. Rehrauer, P. Wang, and D. Ben-Amotz, "Digital compressive chemical quantitation and hyperspectral imaging," Analyst **138**, 4982 (2013).

56. O. G. Rehrauer and S. Claridge, "Multivariate Statistical Methods that Enable Fast Raman Spectroscopy," (2016).

57. D. S. Wilcox, G. T. Buzzard, B. J. Lucier, P. Wang, and D. Ben-Amotz, "Photon level chemical classification using digital compressive detection," Anal. Chim. Acta **755**, 17–27 (2012).

58. F. Soldevila, J. Dong, E. Tajahuerce, S. Gigan, and H. B. de Aguiar, "Fast compressive Raman bio-imaging via matrix completion," **6**, (2018).

59. O. G. Rehrauer, V. C. Dinh, B. R. Mankani, G. T. Buzzard, B. J. Lucier, and D. Ben-Amotz, "Binary Complementary Filters for Compressive Raman Spectroscopy," Appl. Spectrosc. **72**, 69–78 (2018).

60. N. Everall, T. Hahn, P. Matousek, A. W. Parker, and M. Towrie, "Picosecond time-resolved Raman spectroscopy of solids: Capabilities and limitations for fluorescence rejection and the influence of diffuse reflectance," Appl. Spectrosc. **55**, 1701–1708 (2001).

61. W. Zheng, Z. Huang, S. Xie, T.-C. Chia, Z. Lu, and J. K. Chen, "Lifetimes of normal and tumorous human lung tissues by time-resolved fluorescence spectra," 73–77 (1996).

62. H. M. Chen, C. P. Chiang, C. You, T. C. Hsiao, and C. Y. Wang, "Time-resolved autofluorescence spectroscopy for classifying normal and premalignant oral tissues," Lasers Surg. Med. **37**, 37–45 (2005).

63. D. Schweitzer, S. Schenke, M. Hammer, F. Schweitzer, S. Jentsch, E. Birckner, W. Becker, and A. Bergmann, "Towards Metabolic Mapping of the Human Retina," **419**, 410–419 (2007).

64. M. Wakita, G. Nishimura, and M. Tamura, "Some Characteristics of the

Fluorescence Lifetime of Reduced Pyridine Nucleotides in Isolated Mitochondria , Isolated Hepatocytes , and Perfused Rat Liver In Situ," **118**, 1151–1160 (1995).

65. I. Nissinen, A. K. Lansman, J. Nissinen, J. Holma, and J. Kostamovaara, "2x(4)128 time-gated CMOS single photon avalanche diode line detector with 100 ps resolution for Raman spectroscopy," Eur. Solid-State Circuits Conf. 291–294 (2013).

66. R. Krahl, A. Bülter, F. Koberling, and P. Gmbh, "Performance of the Micro Photon Devices PDM 50CT SPAD detector with PicoQuant TCSPC systems," SymPhoTime 1–5 (2005).

67. Micro Photon Device, "PDM Series," 4–5. http://www.micro-photon-devices.com/MPD/media/Datasheet/PDM.pdf (2007).

68. Texas. Instruments, "DLP3000 DLP ® 0 . 3 WVGA Series 220 DMD," https://media.digikey.com/pdf/Data%20Sheets/Texas%20Instruments%20PDFs/DLP3000.pdf (2015).

69. F. L. Pedrotti, L. M. Pedrotti, and L. S. Pedrotti, *Introduction to Optics*, 3rd ed. (Cambridge University Press, 2017).

70. J. A. Decker, "Experimental realization of the multiplex advantage with a hadamard-transform spectrometer.," Appl. Opt. **10**, 510–514 (1971).

71. D. S. Wilcox, G. T. Buzzard, B. J. Lucier, P. Wang, and D. Ben-Amotz, "Photon level chemical classification using digital compressive detection," Anal. Chim. Acta **755**, 17–27 (2012).

72. N. T. Quyen, E. Da Silva, N. Q. Dao, and M. D. Jouan, "New Raman spectrometer using a digital micromirror device and a photomultiplier tube detector for rapid on-line industrial analysis. Part I: Description of the prototype and preliminary results," Appl. Spectrosc. **62**, 273–278 (2008).

73. Z. Liao, F. Sinjab, G. Gibson, M. Padgett, and I. Notingher, "DMD-based software-configurable spatially-offset Raman spectroscopy for spectral depth-profiling of optically turbid samples," Opt. Express **24**, 12701 (2016).

74. F. Sinjab, D. Awuah, G. Gibson, M. Padgett, A. M. Ghaemmaghami, and I.

Notingher, "Holographic optical trapping Raman micro-spectroscopy for non-invasive measurement and manipulation of live cells," Opt. Express **26**, 25211 (2018).

75. P. Matousek, N. Everall, M. Towrie, and A. W. Parker, "Depth profiling in diffusely scattering media using Raman spectroscopy and picosecond Kerr gating," Appl. Spectrosc. **59**, 200–205 (2005).

76. E. Draper, M. Towrie, M. D. Morris, A. W. Parker, P. Matousek, I. P. Clark, N. Everall, and A. Goodship, "Numerical Simulations of Subsurface Probing in Diffusely Scattering Media Using Spatially Offset Raman Spectroscopy," Appl. Spectrosc. **59**, 1485–1492 (2005).

77. Z. Wang, H. Ding, G. Lu, and X. Bi, "Use of a mechanical iris-based fiber optic probe for spatially offset Raman spectroscopy," Opt. Lett. **39**, 3790 (2014).

78. J. Qin, M. S. Kim, W. F. Schmidt, B. K. Cho, Y. Peng, and K. Chao, "A line-scan hyperspectral Raman system for spatially offset Raman spectroscopy," J. Raman Spectrosc. **47**, 437–443 (2016).

79. C. Conti, A. Botteon, C. Colombo, M. Realini, and P. Matousek, "Fluorescence suppression using micro-scale spatially offset Raman spectroscopy," Analyst **141**, 5374–5381 (2016).

80. O. G. Rehrauer, B. R. Mankani, G. T. Buzzard, B. J. Lucier, and D. Ben-Amotz, "Fluorescence modeling for optimized-binary compressive detection Raman spectroscopy," Opt. Express **23**, 23935 (2015).

81. B. M. Davis, A. J. Hemphill, D. Cebeci Maltaş, M. A. Zipper, P. Wang, and D. Ben-Amotz, "Multivariate hyperspectral raman imaging using compressive detection," Anal. Chem. **83**, 5086–5092 (2011).

82. C. J. Corden, D. W. Shipp, P. Matousek, and I. Notingher, "Fast Raman spectral mapping of highly fluorescing samples by time-gated spectral multiplexed detection," Opt. Lett. **43**, 5733 (2018).

83. C. Conti, A. Botteon, C. Colombo, M. Realini, and P. Matousek, "Fluorescence suppression using micro-scale spatially offset Raman spectroscopy," Analyst **141**, 5374–5381 (2016).

84. R. D. Harley, "Artists' pigments c.1600-1835: a study in English documentary sources," viii, 246 p., [7] p. of plates (2001).

85. C. M. Schmidt and K. A. Trentelman, "1064 nm DISPERSIVE RAMAN MICRO-SPECTROSCOPY FOR THE IN-SITU IDENTIFICATION OF ORGANIC RED COLORANTS," e-Preservation Sci. **6**, 10–21 (2009).

86. D. R. Kammerer, *Handbook on Natural Pigments in Food and Beverages Chapter: 3 Anthocyanins* (Elsevier, 2016).

87. S. Q. Lomax, "Phthalocyanine and quinacridone pigments: their history, properties and use," Stud. Conserv. **50**, 19–29 (2005).

88. I. E. Iping Petterson, P. Dvorák, J. B. Buijs, C. Gooijer, and F. Ariese, "Time-resolved spatially offset Raman spectroscopy for depth analysis of diffusely scattering layers," Analyst **135**, 3255–3259 (2010).

89. N. Everall, T. Hahn, P. Matousek, A. W. Parker, and M. Towrie, "Photon migration in Raman spectroscopy," Appl. Spectrosc. **58**, 591–597 (2004).

90. L. Burgio and R. J. H. Clark, *Library of FT-Raman Spectra of Pigments, Minerals, Pigment Media and Varnishes, and Supplement to Existing Library of Raman Spectra of Pigments with Visible Excitation* (2001), Vol. 57.

91. L. Wang, A. Roitberg, C. Meuse, and A. K. Gaigalas, "Raman and FTIR spectroscopies of fluorescein in solutions," Spectrochim. Acta - Part A Mol. Biomol. Spectrosc. **57**, 1781–1791 (2001).

92. A. Periasamy and R. M. Clegg, *FLIM Microscopy in Biology and Medicine* (2009).

93. H. Östmark, M. Nordberg, and T. E. Carlsson, "Stand-off detection of explosives particles by multispectral imaging Raman spectroscopy," Appl. Opt. **50**, 5592–5599 (2011).

94. J. C. Carter, S. M. Angel, M. Lawrence-Snyder, J. Scaffidi, R. E. Whipple, and J. G. Reynolds, "Standoff detection of high explosive materials at 50 meters in ambient light conditions using a small Raman instrument," Appl. Spectrosc. **59**, 769–775 (2005).

95. M. Gaft and L. Nagli, "UV gated Raman spectroscopy for standoff detection of explosives," Opt. Mater. (Amst). **30**, 1739–1746 (2008).

Appendix

As before, the signal to noise ratios are compared for the time gated SPADs and CCD at 785 nm excitation and the 1064 nm InGaAs detector for varying levels of Raman and fluorescence with 300 ps and 3000 ps lifetime fluorophores.

The signal to noise is calculated based upon one pixel. The signal (Raman and fluorescence) incident on that one pixel in one second is indicated in the caption. The amount of fluorescence suppression offered by time gating is calculated by;

$$\frac{1}{1 - e^{-t_g/t_f}}$$

Where the time gate t_g is the IRF of 60 ps and 400 ps for the two SPADS.

Figures A1-A4 show the signal to noise for a range of Raman and fluorescence signal levels with a fluorophore of just 300 ps. The calculations show that although the high temporal resolution SPAD (IRF=60ps) can offer a small amount of fluorescein suppression ~300/60=5x, the lower quantum efficiency of the detector results in a lower signal to noise than the CCD and the low temporal resolution SPAD for almost all signal regimes.

Figures A5-A9 shows the signal to noise signal to noise for a range of Raman and fluorescence signal levels with a fluorophore just 3000 ps. With longer lived fluorophores time gating with the SPADS offers increased SNR in all regimes except for the low fluorescence regime and the extreme fluorescence/high signal regime.

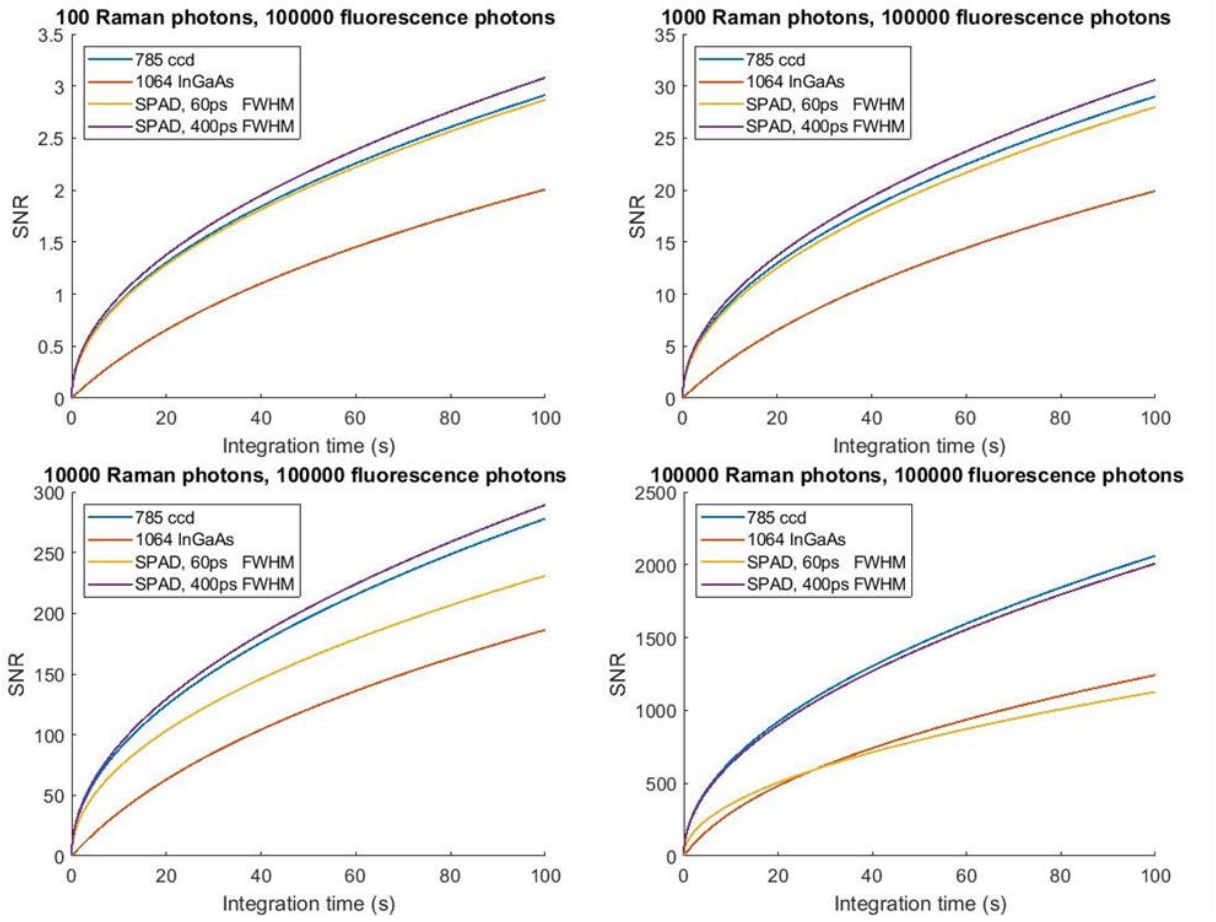

Figure A1. SNR comparison of one pixel of the SPAD, CCD at 785 nm and 1064 nm InGaAs for varying levels of Raman intensity with high levels of fluorescence background from a fluorophore with a 0.3 ns lifetime and time gating equal to the FWHM of the detectors. a) 100 incident Raman photons. b) 1000 incident Raman photons. c) 10000 Raman photons per second, per pixel. d) 100000 Raman photons per second, per pixel.

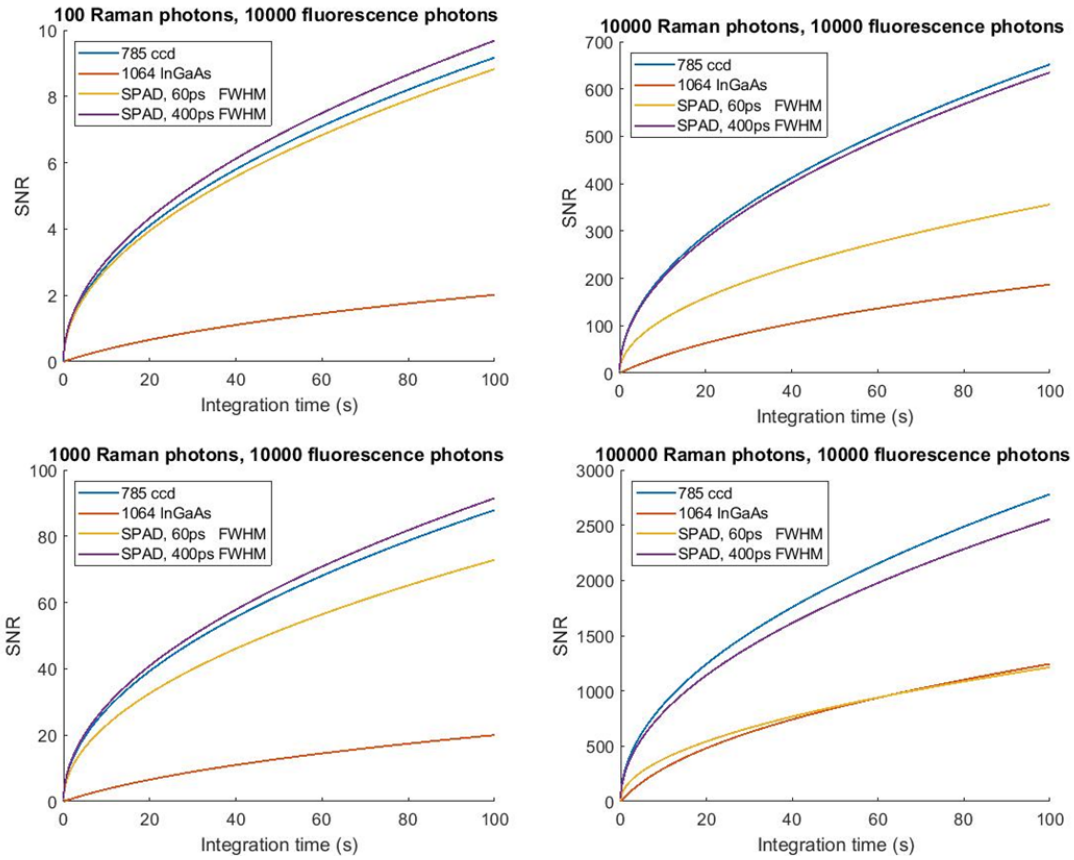

Figure A2. SNR comparison of one pixel of the SPAD, CCD at 785 nm and 1064 nm InGaAs for varying levels of Raman intensity with moderate levels of fluorescence background (10000 photons per pixel per second) from a fluorophore with a 0.3 ns lifetime and time gating equal to the FWHM of the detectors. a) 100 incident Raman photons. b) 1000 incident Raman photons. c) 10000 Raman photons per second, per pixel. d) 100000 Raman photons per second, per pixel.

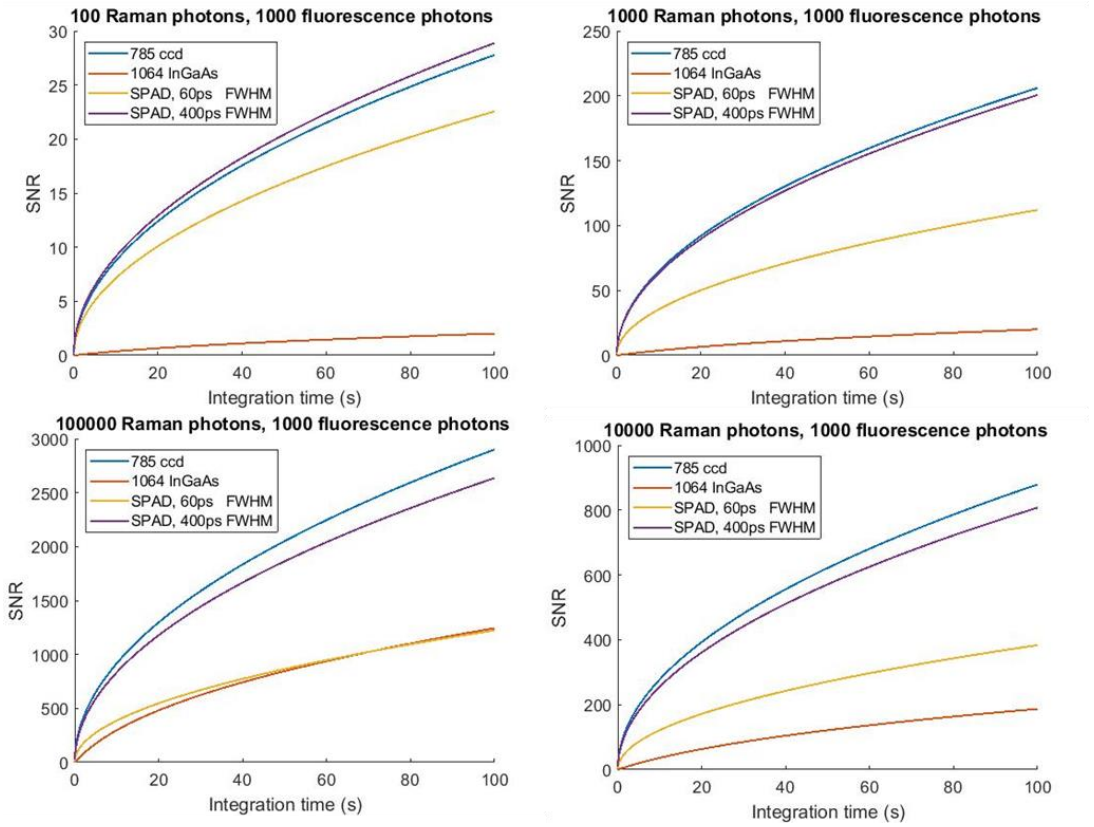

Figure A3. SNR comparison of one pixel of the SPAD, CCD at 785 nm and 1064 nm InGaAs for varying levels of Raman intensity with low levels of fluorescence background (1000 photons per pixel per second) from a fluorophore with a 0.3 ns lifetime and time gating equal to the FWHM of the detectors. a) 100 incident Raman photons. b) 1000 incident Raman photons. c) 10000 Raman photons per second, per pixel. d) 100000 Raman photons per second, per pixel.

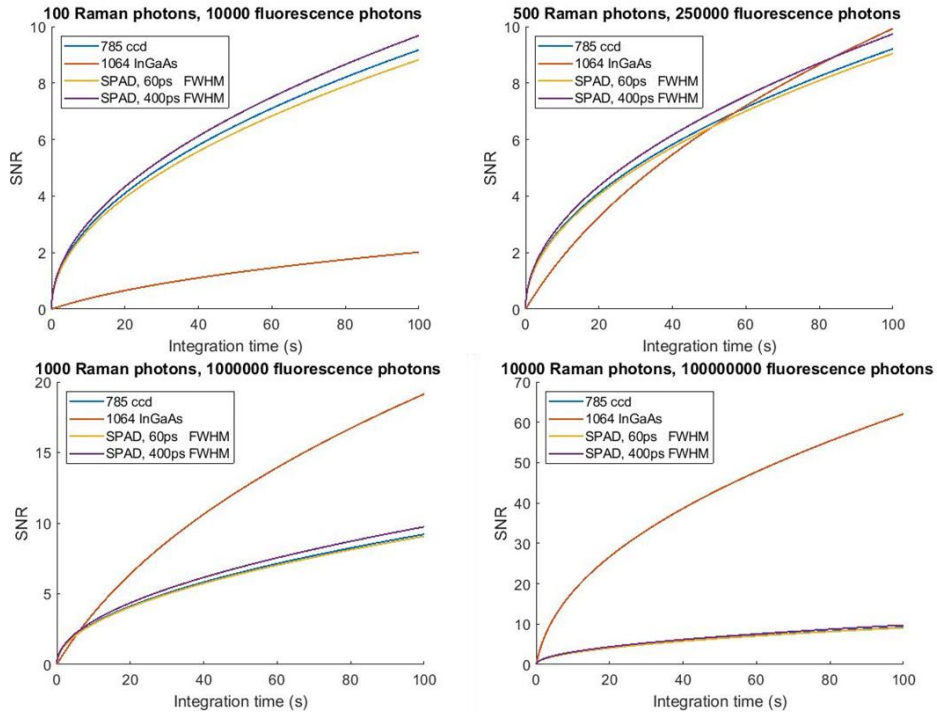

Figure A4. SNR comparison of one pixel of the SPAD, CCD at 785 nm and 1064 nm InGaAs for varying levels of Raman intensity with moderate levels of fluorescence background from a fluorophore with a 0.3 ns lifetime and time gating equal to the FWHM of the detectors. a) 100 incident Raman photons. b) 500 incident Raman photons. c) 1000 Raman photons per second, per pixel. d) 10000 Raman photons per second, per pixel.

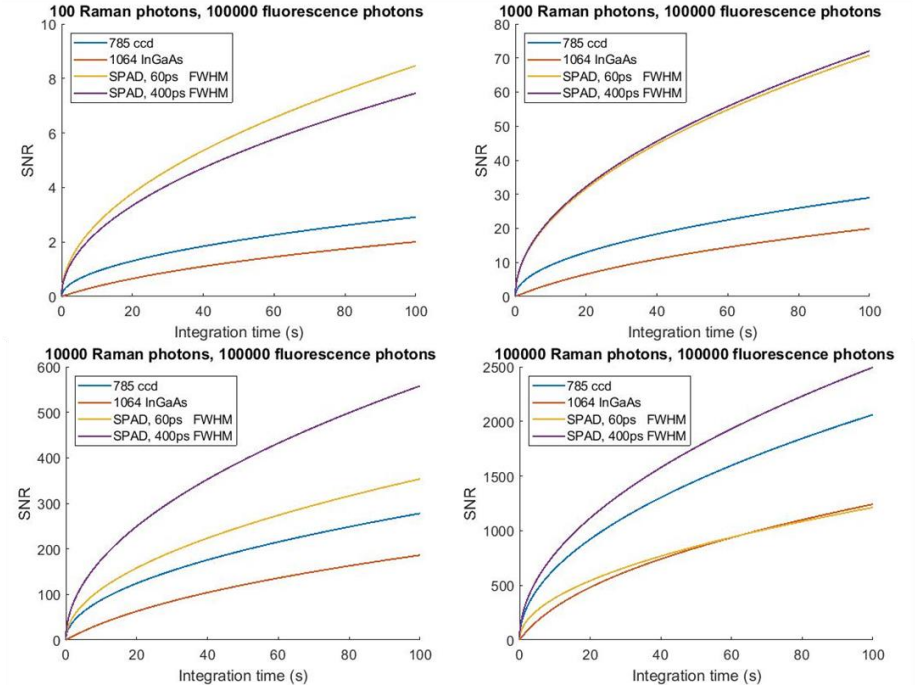

Figure A5. SNR comparison of one pixel of the SPAD, CCD at 785 nm and 1064 nm InGaAs for varying levels of Raman intensity with high levels of fluorescence background (100000 photons per pixel per second) from a fluorophore with a 3 ns lifetime and time gating equal to the FWHM of the detectors. a) 100 incident Raman photons. b) 1000 incident Raman photons. c) 10000 Raman photons per second, per pixel. d) 100000 Raman photons per second, per pixel.

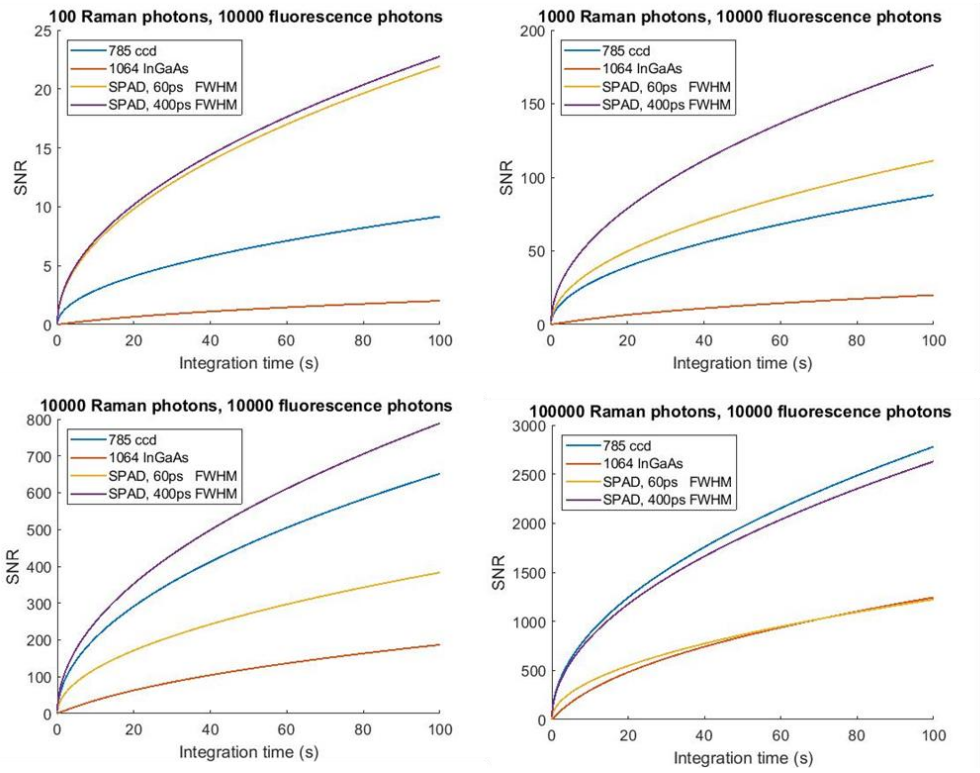

Figure A6. SNR comparison of one pixel of the SPAD, CCD at 785 nm and 1064 nm InGaAs for varying levels of Raman intensity with moderate levels of fluorescence background (10000 photons per pixel per second) from a fluorophore with a 3 ns lifetime and time gating equal to the FWHM of the detectors. a) 100 incident Raman photons. b) 1000 incident Raman photons. c) 10000 Raman photons per second, per pixel. d) 100000 Raman photons per second, per pixel.

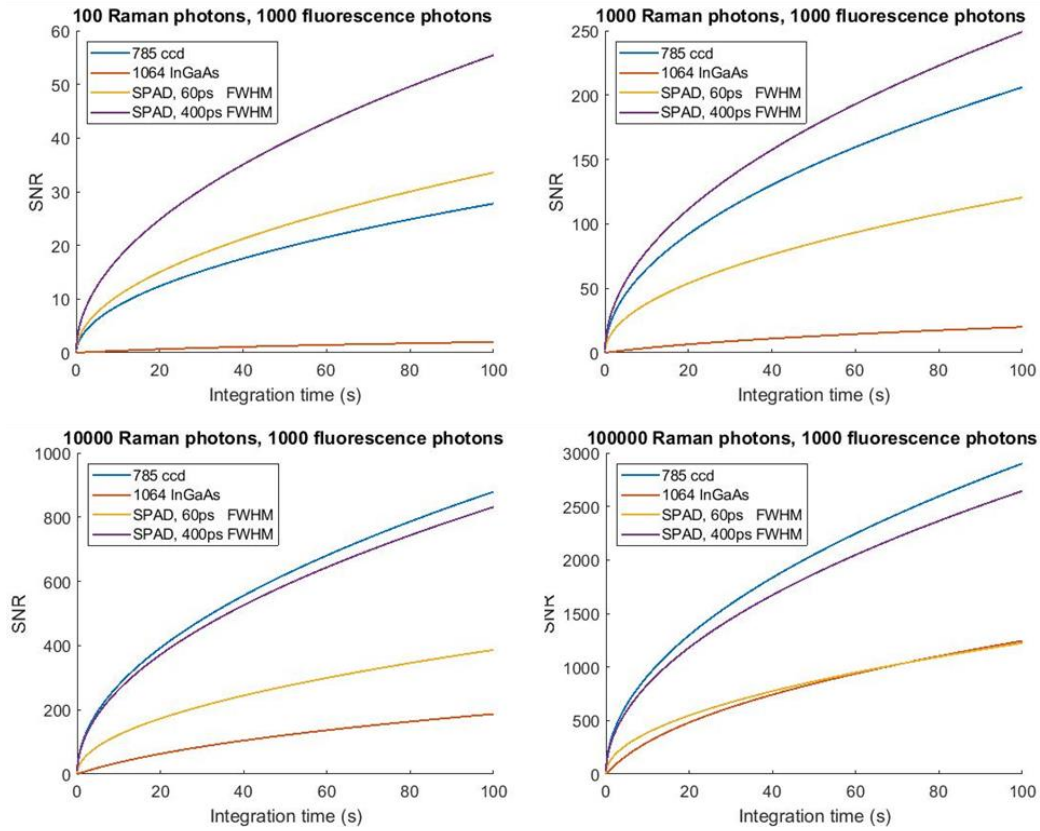

Figure A7. SNR comparison of one pixel of the SPAD, CCD at 785 nm and 1064 nm InGaAs for varying levels of Raman intensity with low levels of fluorescence background (1000 photons per pixel per second) from a fluorophore with a 3 ns lifetime and time gating equal to the FWHM of the detectors. a) 100 incident Raman photons. b) 1000 incident Raman photons. c) 10000 Raman photons per second, per pixel. d) 100000 Raman photons per second, per pixel.

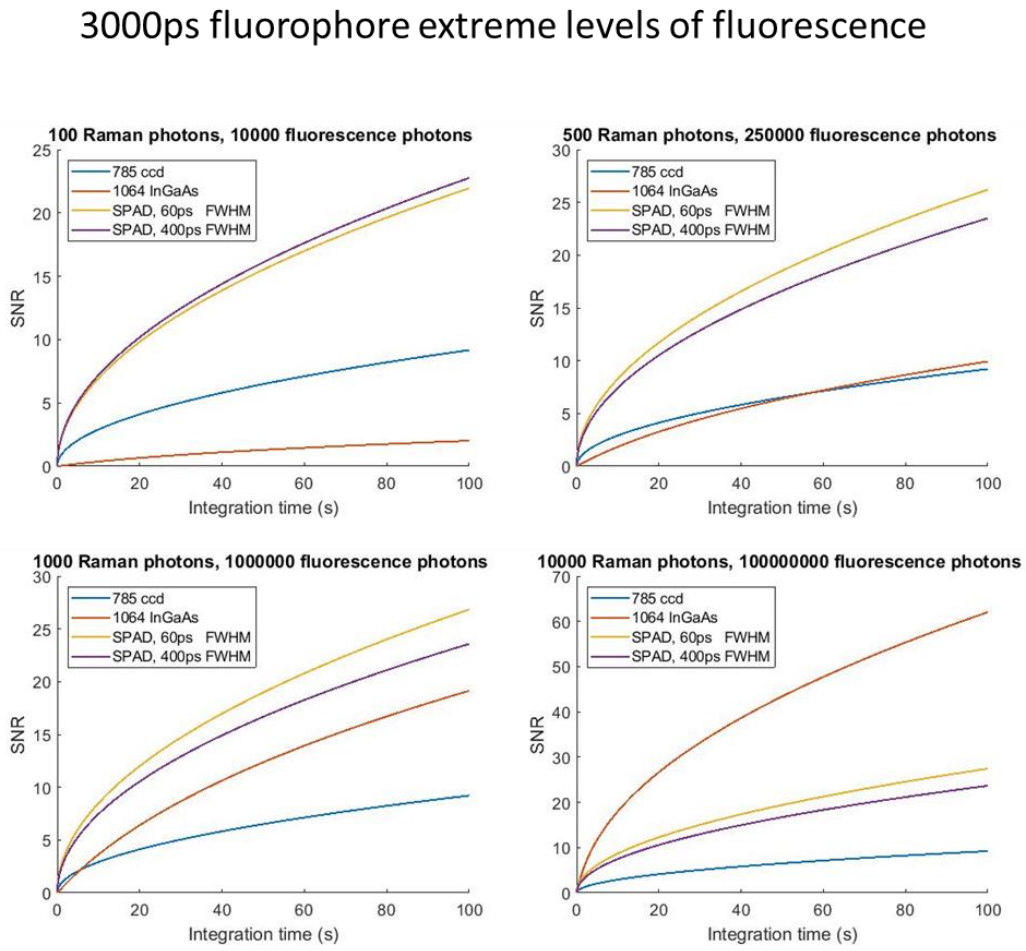

Figure A8. SNR comparison of one pixel of the SPAD, CCD at 785 nm and 1064 nm InGaAs for varying levels of Raman intensity with moderate levels of fluorescence background (10000 photons per pixel per second) from a fluorophore with a 3 ns lifetime and time gating equal to the FWHM of the detectors. a) 100 incident Raman photons. b) 500 incident Raman photons. c) 1000 Raman photons per second, per pixel. d) 10000 Raman photons per second, per pixel.